ISTANBUL TECHNICAL UNIVERSITY ★ INFORMATICS INSTITUTE

THE PROPERTIES OF NANOSTRUCTURED BINARY METAL ALLOYS

Ph.D. THESIS

Berk ONAT

Department of Computational Science and Engineering

Computational Science and Engineering Programme

JULY 2013

ISTANBUL TECHNICAL UNIVERSITY ★ INFORMATICS INSTITUTE

THE PROPERTIES OF NANOSTRUCTURED BINARY METAL ALLOYS

Ph.D. THESIS

Berk ONAT
(702052005)

Department of Computational Science and Engineering

Computational Science and Engineering Programme

Thesis Supervisor: Prof. Dr. Sondan DURUKANOĞLU FEYİZ

JULY 2013

İSTANBUL TEKNİK ÜNİVERSİTESİ ★ BİLİŞİM ENSTİTÜSÜ

NANOYAPILI İKİLİ METAL ALAŞIMLARIN ÖZELLİKLERİ

DOKTORA TEZİ

Berk ONAT
(702052005)

Hesaplamalı Bilim ve Mühendislik Anabilim Dalı

Hesaplamalı Bilim ve Mühendislik Programı

Tez Danışmanı: Prof. Dr. Sondan DURUKANOĞLU FEYİZ

TEMMUZ 2013

Berk ONAT, a Ph.D. student of ITU Informatics Institute 702052005 successfully defended the thesis entitled **“THE PROPERTIES OF NANOSTRUCTURED BINARY METAL ALLOYS”**, which he/she prepared after fulfilling the requirements specified in the associated legislations, before the jury whose signatures are below.

Thesis Advisor : **Prof. Dr. Sondan DURUKANOĞLU FEYİZ** ....
Sabancı University

Jury Members : **Prof. Dr. A. Nihat BERKER** ....
Sabancı University

Assoc. Prof. Dr. Aylin SUNGUR ....
İstanbul Technical University

Assoc. Prof. Dr. Oğuzhan GÜRLÜ ....
İstanbul Technical University

Assist. Prof. Dr. Adem TEKİN ....
İstanbul Technical University

Date of Submission : **24 June 2013**
Date of Defense : **29 July 2013**

"Now, if my calculations are correct, when this baby hits eighty-eight miles per hour, you're gonna see some serious…"
Dr. Emmett L. Brown

to my family

FOREWORD

I would like to thank my supervisor, Prof. Dr. Sondan Durukanoğlu Feyiz for giving me the opportunity to do this work and all the guidance, advices in every single step of my research and studies. I am grateful to her as she is a real mentor and a demanding person that guide me to be a better and real researcher and made this dissertation possible. I thank all my professors and the supporting advisors following the research progress, Assoc. Prof. Fethiye Aylin Sungur and Assoc. Prof. Oğuzhan Gürlü for their advises, help and collaborations. I thank to the jury committee, Assist. Prof. Adem Tekin for insightful advises and Prof. Dr. A. Nihat Berker for the invaluable discussions, experienced critics, and mentoring in many occasions.

I also thank all my colleagues for the warm atmosphere and the staff for the administrative helps in the department of Computational Science and Engineering in Informatics Institute. I would also like to thank the Scientific and Technological Research Council of Turkey-TUBITAK for the financial support under Grant No. 106T567, 109T105 and the National Center for High Performance Computing at ITU for providing us the machines and extra allocations to perform the computations.

I can never thank enough to my family, my mother, my father and my brother for their support and encouragements throughout my life and my mother-in-law and father-in-law for their endless support. Special thanks also go to other family members: Lokum (*Turkish Delight*) and Badem (*Almond*) - the kittens.

Finally, I am also grateful to my wife for her endless support, advises and love. I will always appreciate her great help and care in every state of demand for assistance.

July 2013 Berk ONAT

TABLE OF CONTENTS

Page

FOREWORD .... **ix**
TABLE OF CONTENTS .... **xi**
ABBREVIATIONS .... **xiii**
LIST OF TABLES .... **xv**
LIST OF FIGURES .... **xvii**
LIST OF SYMBOLS .... **xxi**
SUMMARY .... **xxiii**
ÖZET .... **xxv**
1. INTRODUCTION **1**
2. METHODS **3**
  2.1 Time Independent Schrödinger Equation in Born-Oppenheimer Approximation 3
  2.2 Density Functional Theory (DFT) 4
    2.2.1 Hohenberg-Kohn theorems 4
    2.2.2 Kohn-Sham equations 5
    2.2.3 The approximation to exchange-correlation energy 8
      2.2.3.1 Local density approximation 8
      2.2.3.2 Generalized gradient approximation 9
  2.3 Embedded Atom Method (EAM) 9
  2.4 The Calculation of Structural Constants and Energies in EAM 13
  2.5 Phonon Dispersions 16
  2.6 Molecular Dynamic Simulations (MD) 18
  2.7 Nudged Elastic Band Method (NEB) 20
  2.8 Real Space Green's Function Method for Vibrational Local Density of States 22
  2.9 Adaptive Particle Swarm Optimization (APSO) 25
3. CALCULATIONS ON Cu NANOWIRES **31**
  3.1 Atomic Relaxations on Cu Nanowires 31
  3.2 Computational Details 31
  3.3 Results & Discussions 34
4. CHARGE CORRECTED EAM POTENTIAL FOR Cu-Ni ALLOYS **39**
  4.1 The Theoretical and Computational Details of Cu-Ni EAM Potential 40
    4.1.1 Parametrization of alloy potential 40
    4.1.2 *Ab-initio* calculations 42
  4.2 Optimization and Fitting Procedure of Cu-Ni Potentials 45

4.3 The Results and Discussions for Cu-Ni EAM Potential 47
  4.3.1 The structural and total energy calculations 50
  4.3.2 Phonon dispersions for Cu, Ni and Cu-Ni alloys 58
  4.3.3 The energy barriers of various diffusion mechanisms for Cu, Ni adatoms on Cu or Ni surfaces 59
5. VIBRATIONAL THERMODYNAMICS OF Cu-Ni ALLOYS 63
5.1 The Theoretical and Computational Details 63
5.2 The Vibrational Density of States of Cu-Ni Alloys 66
5.3 Heat Capacity of Cu-Ni Alloys 69
5.4 Free Energy and Entropy Calculations for Cu-Ni Alloys 71
6. THE GROWTH OF Ni AND Cu-Ni NANOSTRUCTURES ON Cu(111) SURFACE 77
6.1 The Evolution of Ni and Cu Add/Vacancy Islands on Cu(111) 77
6.2 Sub-Monolayer Ni Deposition on Cu(111) 82
6.3 The Structural Properties of Ni and Cu-Ni Islands on Cu(111) 83
6.4 The Kinetics of Ni, Cu Adatoms on Cu(111) 84
7. CONCLUSION 87
REFERENCES 89
CURRICULUM VITAE 100

ABBREVIATIONS

MPI : Message passing interface
FMM : Force-matching method
TBA : Tight-binding approach
EMT : Effective-medium theory
EAM : Embedded atom method
APSO : Adaptive particle swarm optimization
TISE : Time independent Schrödinger equation
BOA : Born-Oppenheimer approximation
DFT : Density functional theory
HK : Hohenberg-Kohn
LDA : Local density approximation
GGA : Generalised gradient approximation
PW91 : Perdew and Wang
PBE : Perdew-Burke-Enzerhof
EOS : Equation of states
MD : Molecular dynamic
NVE : Microcanonical ensemble
NVT : Constant-volume canonical ensemble
NEB : Nudged elastic band method
MEP : Minimum energy path
RSGF : Real space Green's function
PSO : Particle swarm optimization
ESE : Evolutionary state estimation
ELS : Elitist learning state
MEAM : Modified embedded atom method
MPI : Message passing interface
FSM : Finnis-Sinclair model
SCF : Self-consistent field
fcc : Face-centered cubic
sc : Simple cubic
bcc : Base-centered cubic
dc : Diamond cubic
hcp : Hexagonal closed packed
SF : Stable stacking fault
US : Unstable stacking fault
NPT : Constant-pressure canonical ensemble
$\mathbf{D}_{fcc}$: Dumbell
$\mathbf{T}_h$: Tetrahedra
$\mathbf{O}_h$: Octahedra
DOS : Density of states

VDOS : Vibrational density of states
ML : Monolayer
STM : Scanning tunnelling microscopy
nn : Nearest-neighbor
St : Step
DL : Double layer
M : Monomer
H : Hopping
E : Exchange
+X : Number of chain
ps : Picosecond
ns : Nanosecond
ν**s** : Microsecond
eV : electron-volt
K : Kelvin
J : Joule
Å : Angstrom
Ry : Rydberg
THz : Terahertz

LIST OF TABLES

Page

Table 4.1 : Experimental lattice constants for Cu-Ni alloys and unit cell dimensions for the representative crystal structures for *ab-initio* calculations. The experimental values for each desired concentration were the interpolated values of the experimental concentrations taken from Ref. [68], [69]. 44

Table 4.2 : Optimized and fitted parameters for pure Cu, Ni elements and Cu-Ni alloy.. 48

Table 4.3 : Lattice constants, cohesive energies, bulk modulus, elastic constants, diatomic bond lengths and bond energies, vacancy formation energies and phonons at X, L, and K for Cu and Ni predicted by the current EAM potential, together with the available experimental data and other EAM potentials. † Fitted with low weight. * Fitted with high weight. 51

Table 4.4 : Lattice constants, cohesive energies, bulk modulus, elastic constants, vacancy formation energies and diatomic bond lengths and bond energies for Cu-Ni alloys predicted by the current EAM potential compared with the available experimental and *ab-initio* data. † Fitted with low weight. $*$ Fitted with high weight................. 52

Table 4.5 : Energies (mJ/m^2) for surface formation, planar defects and energies (eV) of interstitials for Cu, Ni elements calculated by the current EAM potentials compared with available experimental data. 56

Table 4.6 : Energies per atom (mJ/m^2) for several selected crystal structures of Cu, Ni calculated by the current EAM potentials and compared with *ab-initio* data.. 57

Table 4.7 : Diffusion energy barriers (eV) for Cu and Ni adatoms on various Cu and Ni surfaces calculated with the Cu-Ni alloy EAM potential and compared with available experimental, *ab-initio*, or model potential data in Ref. [100]. 62

Table 5.1 : The VDOS shifting factor f for Cu-Ni alloy with respect to the pure Cu phonon spectrum. 69

Table 6.1 : The energy barriers for various diffusion mechanisms of Ni and Cu on Cu(111). Abbreviations: St: step, ML: monolayer, DL: doublelayer, M: monomer, H: hopping, E: exchange. +X represents X chains of Cu or Ni atoms at the step, A/ represents adatom on the surface or island layer where A can be one of Cu or Ni. The values in brackets ( ) are up barriers for hopping and exchange diffusion mechanisms and detachment barriers from dimer and trimer. 86

LIST OF FIGURES

Page

Figure 2.1 : Schematic representation of Khon-Sham Ansatz [15]. 7

Figure 2.2 : Illustration of the NEB method: (a) The images are generated along the blue line interpolation between initial state, R_0, and final state, R_N. The NEB method apply F_i^{NEB} force during the optimization to relax the images on to the true MEP. (b) The force components along the reaction path: F_i^{NEB} is the nudged elastic band force, $F_i^{\perp}$ is the perpendicular force of F_i due to the $V(R)$ potential, $F_i^{S||}$ shows the spring force parallel to tangent $\hat{\tau}_i$ [38,39]... 21

Figure 2.3 : The compared distances for g and P_1 particles to the others in (a) exploration, (b) exploitation, convergence, and (c) jump-out states, where g is the globally the best particle in the swarm with $P_1, P_2, \ldots, P_5$ [45].. 27

Figure 2.4 : S_1 exploration, S_2 exploitation, S_3 convergence and S_4 jump-out state membership for evolutionary factor [45].................................. 27

Figure 2.5 : The swarm distribution in various evolutionary states of an optimization for two dimensional problem. (a)Exploration, (b)Exploitation, (c)Convergence, (d)Jump-out................................. 28

Figure 2.6 : The flow chart of (a) main APSO algorithm, (b) Evolutionary state estimation, (c) Elitist learning [45].. 29

Figure 3.1 : Cross-sectional (on the left) and perspective view (on the right) of the <100> axially oriented nanowire with 7×7 number of atoms along the diagonals. The darker and lighter yellow spheres show the atoms in A and B type stacking of Cu(100) crystal. For the N(100)×(100) type nanowires, the distance between the atoms along the diagonal is nn (nearest neighbor distance)......................... 32

Figure 3.2 : Cross-sectional (on the left) and perspective view (on the right) of the <110> axially oriented nanowire with 7×7 number of atoms along the diagonals. The darker and lighter yellow spheres show the atoms in A and B type stacking of Cu(110) crystal. For the N(110)×(111) type nanowires, the distances between the atoms along the short and long diagonals are *nn* (nearest neighbor distance) and a_0 lattice constant, respectively................................... 32

Figure 3.3 : The atomic relaxations, with respect to bulk terminated positions, at the cross-sectional plane of (a) 5(100)×(100) and (b) 15(100)×(100) type nanowires. (b) shows atomic displacements only on the left corner of the 15×15 nanowire. The displacements are magnified by a factor 4.5 in both (a) and (b). Here C represents the atom at the center of cross-sectional plane. The labeled atoms of A and B represent the atoms of A and B type stacking of Cu(100) crystal. Note that the magnitudes of the relaxations of atoms around the edges of nanowire diminish as the cross-sectional area increases. 35

Figure 3.4 : The relative energy profiles of various elongation steps for (a) <100> and (b) <110> oriented nanowires with respect to bulk cohesive energy. The bulk energy profile is shown for comparison... 37

Figure 3.5 : The cross-sectional area of <100> nanowire under (a) %36 and (b) %37 contraction. 37

Figure 4.1 : The electron charge distributions for Cu and Ni. (a) The probability distributions for 3*d* and 4*s* Slater-type orbitals for effective nuclear charges, (b) The total charge distribution for 3*d* and 4*s* from SCF calculations of Clementi et al. [62,63] 41

Figure 4.2 : Cu-Ni EAM potential functions: (a) pair interaction function, (b) electron charge density function, and (c) embedding energy function. 49

Figure 4.3 : The atomic configurations for (a) the non-defect structure of *fcc* bulk crystal from top view of (111) orientation, (b) side view of the defect free structure, (c) (111) stacking fault structure in between the layers of blue and red atoms, (d) the two (111) twining fault structure in between the layers of blue and red atoms. 54

Figure 4.4 : The atomic configurations for (a) the defect free structure of *fcc* bulk crystal from top view of (001) orientation, (b) dumbbell (red atoms) structure, (c) (111) stacking fault structure in between the layers of blue and red atoms, (d) the two (111) twining fault structure in between the layers of blue and red atoms. The colors represent the cohesive energies in between the minimum -3.54eV (blue) and maximum -2.89eV (red). 55

Figure 4.5 : Mixing enthalpy for Cu-Ni alloy in various concentrations of Ni calculated with the current EAM potential. The experimental values from Ref. [97], [98] and the values of other EAM type potentials from Ref. [8], [9], and [99] are shown for comparison. 58

Figure 4.6 : Phonon dispersion curves (a) for Cu and (b) for Ni: solid line stands for the values obtained from current EAM, dashed line from *ab-initio* method and hollow circles from the experiment at 80K for Cu [86], 296K for Ni [87]. 60

Figure 4.7 : Phonon dispersion curves (a) for $L1_2$ Cu_3Ni, (b) for $L1_1$ CuNi, (c) for $L1_2$ Ni_3Cu: solid line represent the values obtained from the current potential, dashed line from *ab-initio* method, and dotted line from Foiles EAM potential [9]. 61

Figure 5.1 : VDOS for (a) Cu and Ni (inset) (b) Cu-Ni alloys calculated with the current EAM potential. The experimental curves for pure Cu and Ni from Ref. [111] and [112] are shown for comparison. 66

Figure 5.2 : The calculated partial VDOS for (a) Cu and (b) Ni in the alloy. 67

Figure 5.3 : The vibrational DOS for ordered (a) $Cu_{75}Ni_{25}$, (b) $Cu_{50}Ni_{50}$, and (c) $Cu_{25}Ni_{75}$ alloys calculated with the current EAM potential together with the disordered and segregated Cu-Ni alloys VDOS. ... 68

Figure 5.4 : The vibrational heat capacity calculated with the current EAM potential (a) for pure Cu and Ni (inset) (b) for various Cu-Ni alloys in addition to the excess vibrational heat capacity calculated with the current EAM potential (c) for various Cu-Ni alloys (d) when the electronic contributions were accounted. The experimental values for pure elements from Ref. [114] and for Cu-Ni alloys from Ref. [106] are shown for comparison. 70

Figure 5.5 : (a) The vibrational free energy for Cu-Ni alloys, (b) the concentration weighted excess free energy, (c) mixing enthalpy, (d) the partial and (e) total vibrational entropy for various Cu-Ni alloys and ordered phases calculated with the current EAM potential. 73

Figure 5.6 : The vibrational excess entropy compared (a) to the partial and configurational entropies and (b) to the experimental results from Ref. [98] at 298K and Ref. [97] at 1000K. 75

Figure 6.1 : The snapshots of the evolution for monolayer Ni (blue) and Cu (yellow) islands on Cu(111) surface (1st layer: orange, 2nd layer: red). (a) Initial configuration, (b)-(p) the snapshots of the system at the end of every 100ns, except (f), (i) and (p) where the first one shows the formation of the bridge at 450ns, the second one shows dimer formation at 728ns and the last one shows the final configuration at 1690ns. 79

Figure 6.2 : (a) The initial and (b) the final configuration after 840ns simulation of monolayer Ni (blue) and Cu (yellow) islands with 6nn separation on Cu(111) surface (1st layer: orange, 2nd layer: red). ... 79

Figure 6.3 : (a) The initial and (b-h) configurations after each 25ns simulations of double-layer Ni (bottom:blue, top:white) and Cu (yellow) islands on Cu(111) surface (1st layer: orange, 2nd layer: red)........... 80

Figure 6.4 : The (a) initial configuration and (b-f) configurations after each 100ns simulation steps of double-layer Ni (bottom: blue, top: white) and vacancy Cu islands on Cu(111) surface (1st layer: orange, 2nd layer: red)... 81

Figure 6.5 : (a) The initial and (b-f) the configurations after each 200ns simulation steps of monolayer Ni (blue) and Cu vacancy islands on Cu(111) surface (1st layer: orange, 2nd layer: red)...................... 82

Figure 6.6 : The snapshots of the final configurations of Ni atoms (top: green, middle: white, bottom: blue) on Cu(111) surface (1st layer: orange, 2nd layer: red) for (a) 500ps uniform, (b) 5ns uniform, (c) 10ns uniform and (d) 2-5ns nonuniform Ni deposition simulations... 83

Figure 6.7 : The average heights for the predefined profile on (a) double-layer Cu-Ni islands (inset shows top view of the supercell where blue and yellow atoms represent Ni and Cu, respectively) and (b) monolayer Ni island.. 84

LIST OF SYMBOLS

H : Hamiltonian operator,
Ψ : Wave function,
E : Electronic energy,
$\hbar$: Planck constat,
$\vec{R}$: Nuclear coordinates,
M_I : Mass of the nuclei,
Z_I : Atomic mass of the nuclei,
$\vec{r}$: Coordinate of the electrons,
m_e : Mass of the electron,
$v_{ext}(\vec{r})$: External potential,
$n_0(\vec{r})$: Electronic density of ground state,
$F[n(\vec{r})]$: Universal functional of density,
$E_{HK}[n]$: Energy of the system in Hohenberg-Kohn formalism,
$n_(\vec{r})$: Density of electronic states,
$T_R[n]$: Kinetic energy of non-interacting electrons,
$E_{xc}[n]$: Exchange and correlation energy,
$E_{Hartree}[n]$: Hartree energy,
$v_{KS}(\vec{r})$: Kohn-Sham potential,
v : Chemical potential,
ε_i : Eigenvalue,
ε_{xc} : Exchange-correlation potential,
$\varepsilon_x(n)$: Exchange potential,
$\varepsilon_c(n)$: Correlation potential,
$\mathscr{F}$: Nonlinear functional of the charge density,
ρ_i : Charge density,
$F(\rho_i)$: Embedding energy,
Z_j : Type of jth ion,
r_{cut} : Cutoff radius,
ϕ : Pair interaction,
h_{smooth} : Smoothing function,
a_0 : Lattice constant,
Ω_0 : Atomic volume,
B : Bulk modulus,
E_{coh} : Cohesive energy,
S_A : Scaling parameter,
G_A : Shifting parameter,
$\vec{\mathfrak{F}}$: Force,
C_{mnkl} : Elasticity tensor,
E_{relax} : Relaxation energy,

$\vec{u}$: Displacement,
$\vec{q}$: Wave vector,
w : Angular frequency,
$\tilde{U}$: Amplitude of the wave,
Ψ_{ij}^{mn} : Force constant,
$D_{mn,ij}$: Dynamical matrix,
N : Number of atom,
E : Total energy,
m : Mass,
U : Interatomic potential,
$\ddot{\vec{r}}$: Acceleration,
U : Interatomic potential,
$r\vec{(t)}$: Position,
$p\vec{(t)}$: Momentum,
Δt : Time-step,
$\dot{\vec{r}}$: Velocity,
k_B : Boltzman constant,
T : Temperature,
k_S : Spring constant,
$\vec{\nabla}V(\vec{R})$: Gradient of the energy,
G : Green function,
h_i : Sub-matrix,
I : Unit matrix,
w : Vibrational frequency,
d_b : Interlayer separation,
Z^* : Effective Charge,
n^* : Effective quantum number,
γ_{SF} : Stable stacking fault,
γ_{US} : Unstable stacking fault,
γ_T : Twining fault,
γ_S : Surface formation,
E_I : Interstitial energy,
H_{A-B} : A-B Mixing Enthalpy,
S : Entropy,
S_{vib} : Vibrational entropy,
F : Free energy,
F_{vib} : Vibrational free energy,
C_V : Lattice heat capacity,
$N(\omega)$: The normalized total vibrational density of states,
f^{Exp} : Scaling factor,
S_{conf} : Configurational entropy,
S_{elec} : Electronic entropy,
$f(\varepsilon)$: Fermi-Dirac distribution,
ε_F : Fermi energy,
C_V^{elec} : Electronic specific heat capacity,
C_P : Constant pressure heat capacity.

THE PROPERTIES OF NANOSTRUCTURED BINARY METAL ALLOYS

SUMMARY

In this Thesis, a new semi-empirical and many-body type model potential for Cu-Ni alloys was developed using embedded atom method (EAM) formalism based on a modified charge density profile with an improved optimization technique. In the process, the charge density profile for pure Cu and Ni elements was modified by incorporating the 4s charge density contribution within the optimization. The adaptive particle swarm optimization (APSO) method was utilized to search the parameter space of the EAM functions. The technique was further optimized by implementing MPI based parallel algorithms. The potential was furnished by fitting to experimental and first-principle data for Cu, Ni, and Cu-Ni binary compounds, such as lattice constants, cohesive energies, bulk modulus, elastic constants, diatomic bond lengths, and bond energies. The generated potentials were then tested through computing a variety of properties of pure elements and the alloy of Cu, Ni: the melting points, alloy mixing enthalpy, vibrational thermodynamical functions, equilibrium lattice structures, vacancy formation, stacking and interstitial formation energies, and various diffusion barriers on the (100) and (111) surfaces of Cu and Ni.

In general, modifications on the charge density profile of pure Cu and Ni resulted in the phonon dispersion curves for pure Cu, Ni and Cu-Ni alloys of 25%, 50%, and 75% Ni concentrations in a good agreement with experimental and *ab-initio* findings. The calculations on vacancy formation, stacking and interstitial fault energies led to results that are in good agreement with the experimental and *ab-initio* data. These promising results are a good measure for the reliability of the potential when the system is under deformation. The calculations of vibrational thermodynamical properties within the harmonic approximation of lattice dynamics also produced results that are in good agreement with the available experimental data. The thermodynamical functions of specific heat capacity, free energy, and entropy were determined for various concentrations of Cu-Ni alloys. Although for most properties of the alloy systems, the electronic contributions are expected to be the driving element, for the current case the dominant contribution to the thermodynamical properties was found to be governed by the phonons of the system. The result for the vibrational properties further indicated that Cu bonds get stronger with increasing Ni concentration in the Cu-Ni alloys, that is usually attributed to the change in energy introduced by the *sd* hybridization in such systems.

The potentials were further tested for the growth mechanisms of Ni, Cu nanostructures on the Cu(111) surface both using molecular dynamic (MD) simulations and total energy calculations. The main outcome of the simulations was that Cu atoms could easily incorporate into the upper layers of Ni nano-clusters with mono and double layers on the substrate. The migration of Cu atoms to the upper layers of Ni islands were found to be influenced by the number of layers in Ni islands: there was a remarkable increase in Cu migration to above layers of double-layer Ni islands when compared to single-layer Ni islands. As the diffusion mechanisms are important factors in determining the growth characteristics on surfaces and have critical role in the kinetics of the surface structures, the energy barriers were also calculated using nudged elastic band method (NEB) for various diffusion mechanisms on Cu(111) surface. The critical mechanism determining whether the island would be a pure Ni surrounded by Cu atoms or Cu-Ni mixed island was found to be the dimer formation over the Ni monolayer islands. The results also showed that nanostructures can have both mixed and segregated phases for Cu-Ni islands on the surface and the heights of these structures can differ by the type of formation. These findings can help one to understand the experimental observations on the growth of single or double layer Ni islands on Cu(111) surface.

NANOYAPILI İKİLİ METAL ALAŞIMLARIN ÖZELLİKLERİ

ÖZET

Bu Tez çalışmasında, Gömülü Atom Yöntemi (GAY) kullanılarak Cu-Ni alaşımları için yük yoğunluğu tanımlamaları yeniden düzenlenmiş ve bu tanım kullanılarak yarı deneysel çok cisimli model potansiyeller üretilmiştir. Cu ve Ni saf elementleri için yük yoğunluğu tanımı, 3d valans elektron yoğunluğuna 4s elektron yoğunluğunun katkısı eklenerek sağlanmıştır. Potansiyel fonksiyon parametrelerinin ayarlanması için uyumlu parçacık sürüsü optimizasyon (APSO) yönteminden yararlanılmış, yöntemin hesaplama süresinin kısaltılması için ise MPI tabanlı paralel dağıtık algoritmalar kullanılmıştır. Ayrıca, APSO yönteminde yerel minimum durumlarından kaçınılmasını sağlayan 'Elit Öğrenme' süreci paralel programlama algoritmaları yardımıyla hem dağıtık mimaride geliştirilmiş hem de birden fazla sayıda alınarak yakınsama hızının arttırılması sağlanmıştır. Potansiyel fonksiyonlarının hem saf Cu ve Ni, hem de Cu-Ni alaşımları için eğri ayarlanarak belirlenmesinde örgü sabiti, hacim modülü, elastik sabitler, boşluk oluşturma enerjisi, ikili bağ uzunluğu ve enerjisi gibi deneysel ve ilk-ilke değerleri kullanılmıştır. Üretilen potansiyellerin sınanması için ise saf Cu, Ni ve çeşitli Cu-Ni alaşımlarının özellikleri hesaplanmıştır. Bu özellikler; erime sıcaklıkları, alaşım oluşturma entalpisi, titreşim termodinamik fonksiyonları, denge durumu örgü yapıları, alaşım boşluk oluşturma enerjisi, istifleme hatası ve çatlak oluşma enerjileri ile (100) ve (111) yüzeylerinde Cu ve Ni ekatomları için hesaplanan bir çok difüzyon engel değerleridir.

Üretilen potansiyelin yük yoğunluğuna getirdiği düzeltme, hesaplanan saf Cu, Ni ve alaşım Cu-Ni özelliklerinin deney ve ilk-ilke sonuçlarıyla daha tutarlı olmasını sağlamıştır. Hesaplamalardaki en çarpıcı iyileşme saf Cu, Ni ve %25, %50 ve %75 Ni katkılı Cu-Ni alaşımları için hesaplanan fonon dispersiyon eğrilerindedir. Üretilen Cu-Ni GAY potansiyelinin alaşımlar için hem boyuna titreşim frekanslarındaki ayrışmayı doğru betimlediği, hem de tüm titreşim frekans eğrilerinin karakterini ilk-ilke sonuçlarıyla tutarlı ürettiği görülmüştür. Hesaplanan boşluk oluşturma enerjileri, istif hatası ve çatlak oluşturma enerji değerlerinin ise yine deney ve ilk-ilke sonuçlarıyla oldukça tutarlı olduğu görülür. Bu sonuçlar, deformasyona uğratılan bir malzemenin modelenebilmesi için geliştirilen Cu-Ni potansiyelinin güvenilir olduğunun bir göstergesidir. Cu ve Ni için (100) ve (111) yüzeylerinde yine Cu ve Ni ekatom difüzyon engel enerjilerinin deneylerle ve daha önce geliştirilen etkileşim potansiyelleriyle tutarlı olduğu bulunmuştur. Enerji engel değerlerinin tutarlılığı, potansiyelin yüzey uygulamaları için elverişli olduğunu gösterir. Ayrıca, sıcaklığa bağlı hiçbir özelliğin eğri ayarlamada kullanılmadığı düşünülürse, erime sıcaklığı ve yüksek sıcaklıklarda karışım entalpi değerlerinin deney sonuçlarıyla tutarlı olması, üretilen potansiyelin yüksek sıcaklık uygulamalarında da başarılı olacağını belirtir.

Potansiyelin bir uygulaması olarak Cu-Ni alaşımları için titreşimsel termodinamik fonksiyonlarının nasıl değiştiği hesaplanmıştır. Örgü dinamiğinin harmonik yaklaşıklığında yapılan hesaplamaların var olan deney sonuçlarıyla uyumlu olduğu bulunmuştur. Cu-Ni alaşımlarının tüm konsantrasyonları için titreşimsel ısı kapasitesi, serbest enerji ve entropi değerleri belirlenmiştir. Termodinamik fonksiyonlara en büyük katkının fononlar tarafından gerçekleştiği belirlenmesine rağmen Cu-Ni alaşımları için elektronik durumlardan da katkı geldiği ve bu katkının düşük sıcaklıklarda belirleyici olduğu sonucuna varılmıştır. Fonon durum yoğunluğu ve termodinamik fonksiyonların sonuçları, Cu-Ni alaşımlarında Ni oranının arttırılmasıyla Cu bağlarının kuvvetlendiğini gösterir.

Her ne kadar ısı kapasitesi hesaplamaları, titreşim durumlarının katkısının belirleyici olduğunu açık bir şekilde gösterse de elektronik katkıların eklenmesiyle Ni zengin Cu-Ni alaşımlarında deneylerle daha tutarlı sonuçlara ulaşılmıştır. Bu durum, Ni katkısının Cu-Ni alaşımlarında elektronik durumu değiştirdiğini ve termodinamik özelliklere düşük de olsa katkı sağlandığını gösterir. Isı kapasitesi hesaplamaları, düşük sıcaklıklarda anharmonik etkinin daha az olduğuna, yüksek sıcaklıklarda ise Ni için etkinin daha fazla olduğuna işaret eder. Cu-Ni alaşımları tüm Ni konsantrasyonları için Cu ve Ni'in ayırt edilemediği yüzey merkezli kübik bir katı karışımı oluşturur. Karışım yapılanma entropisi her konsantrasyon için pozitiftir ve alaşım oluşturma entropisine daha çok katkı sağladığından Cu-Ni alaşımları karışım oluşturma eğilimindedirler. Bununla birlikte hesaplanan alaşım oluşturma entropi değerleri ise tüm konsantrasyonlar için negatif sonuç üretir. Bu durum faz diyagramında Cu-Ni'in ayrıştığı bir alan oluşumuna katkı sağlar. Bu iki sonuç deneylerle tutarlıdır: Cu-Ni düşük sıcaklıklarda farklı bölgeler oluşturacak şekilde ayrışırlar ve yüksek sıcaklıklarda tek bir fazda karışım oluştururlar. Bir diğer önemli sonuç ise yapılan hesaplamalarda %75 Ni konsantrasyonu civarında fonon durum yoğunluklarının düzenli ve düzensiz alaşımlarda farklı olduğudur. Bu bulgu Warren–Cowley kısa erimli düzen hesaplamalarıyla tutarlıdır. Ayrışmış ve düzenli Cu-Ni yapıları için hesaplanan durum yoğunlukları, düzensiz yapıdakinden az farkla da olsa değişir. Bu sonuç, kısa erimli düzenin %75 konsantrasyon civarında oluşabileceğine işaret edebilir.

Bununla birlikte, geliştirilen potansiyelin sınanmasına yönelik olarak Cu(111) yüzeyi üzerinde Cu ve Ni nanoyapılarının oluşum doğası araştırılmıştır. Yapılan çalışmada toplam enerji hesaplamaları ve moleküler dinamik benzetimlerden yararlanılmıştır. Model benzetimlerinin sonuçları, Cu atomlarının hem tek hem de çift katmanlı Ni nanoyapılarının üst katmanlarına kolaylıkla geçebildiğini göstermiştir. Cu atomlarının Ni adalarının üst katmanlarına gerçekleştirdikleri hareketin Ni adalarındaki tabaka sayısı ile değiştiği gözlenmiştir. Çift katmanlı Ni adalarının üst katmanlarına olan Cu hareketinin, tek katmanlı Ni adalarına olandan 7.5 kat daha hızlı olduğu hesaplanmıştır. Büyümenin doğasının anlaşılabilmesi ve yüzey yapılarının oluşumundaki kritik süreçlerin belirlenebilmesi için çeşitli difüzyon engellerinin enerji değerleri dürtülü elastik bant yöntemiyle hesaplanmıştır. Engel enerji değerleri incelendiğinde, ada oluşumundaki kritik sürecin Ni adası üzerinde ikili öbek oluşumu olduğu saptanmıştır. Bu süreç, adaların Cu atomlarıyla çevrilmiş saf Ni adaları mı yoksa Cu-Ni karışım adaları şeklinde mi oluşacağını belirlemede önemli bir etkendir. Hesaplama sonuçları, Cu(111) üzerinde oluşan nanoyapıların hem Cu ve Ni karışımlı alaşım adaları hem

de Cu ve Ni bölgelerine ayrılmış alaşım adaları olduklarını ve bu adaların yüzeyden farklı yüksekliklerde oluştuğunu göstermiştir. Diğer yandan Ni adalarının başlangıçta nasıl çift katmanlı oluşabildiğini anlayabilmek için, Cu(111) yüzeyine Ni atom ekleme benzetimleri yapılmıştır. 10ns^{-1} ve daha yavaş atom gönderilen yüzeylerde deneylerle örtüşen altıgen yapıların oluştuğu bulunmuştur. Deneylerde ayrıca birden fazla ve çeşitli büyüklüklerde altıgen nanoyapılar oluştuğundan, adaların nasıl büyüyebildikleri yine benzetimler yoluyla araştırılmıştır. Bu benzetimlerde, Ni atomlarının yüzeye eşit veya eşit olmayan zaman adımlarıyla gönderilmesinin ada yapısına olan etkisi incelenmiştir. Benzetim sonuçları, yüzeye eşit olmayan sürelerde Ni atomları göndermenin çeşitli büyüklükteki adaların oluşmasına katkı sağladığı yönündedir. Elde edilen bu sonuçlar ile deneylerde gözlenen Cu(111) yüzeyi üzerindeki tek ve çift katmanlı Ni adalarının oluşum doğası açıklanabilmiştir.

1. INTRODUCTION

There has been a growing interest in developing reliable interaction potentials as they provide an attractive alternative to Quantum Mechanical approaches for atomic-scale simulations of materials that are crucial in understanding material structure evolution under various thermodynamic conditions. Although Quantum Mechanical calculations are based on the first-principle and do not involve parametrization and thus provide the most accurate results, these approaches are confined to the problems which require relatively small computational cells (at most 100 atoms or less) and are limited by the computational power. On the other hand, simulations for realistic problems such as systems with extended defects, phase diagrams and epitaxial growth of materials require relatively large enough computational cells and time up to length- and time-scales comparable to those accessible in experiments. To this end, high quality potentials might be a real choice to tackle down the problems on computational side and thus to study static and dynamic properties of much larger systems.

There are various techniques for developing many-body types potentials: Finnis-Sinclair Model (FSM) [1–3], the tight-binding approach (TBA) [4], the effective-medium theory (EMT) [5], the force-matching method (FMM) [6] and the embedded-atom method (EAM) [7–9]. In all these models the formalism is based on the parametrization of the total energy of the system, and thereby fitting to various properties or energetics of the interested elements or alloys such as lattice constant, melting temperature, elastic constants, etc. Since the accuracy of these potentials is mostly dictated by the fitting procedure for the parameter set and the choice of fitted values, generation of EAM potentials for alloys is sometimes hindered by lack of experimental data such as crystallographic structures, precise energetic values, and elastic constants. In such cases, the conventional way to overcome this drawback is to generate the data using highly accurate first-principle calculations within density-functional theory (DFT) [10] formalism.

In this Thesis, the highly optimized semi-empirical potentials were developed for bulk Cu-Ni alloys based on an approach furnished by the embedded atom method [7,8] with improved optimization techniques. The parametrization involved an extensive set of density functional calculations as well as experimental bulk properties. Although there are several Cu-Ni alloy EAM potentials, they are mostly generated through an optimization procedure based on a fitting to the properties of pure elements of the alloy rather than to the properties of the alloy itself. In the formalism of the very first EAM potentials− developed for 6 *fcc* metals of Ag, Cu, Ni, Au, Pt, Pd and their alloys [8], for example, Cu-Ni alloy potentials were generated through a global fitting process that optimizes the alloy properties not only for Cu-Ni alloy but also for alloys of Cu and Ni with the other four elements. Since the procedure was based on a simultaneous optimization of the potentials for six metals and their alloys instead of optimization of the binary alloy alone, the potentials may have some issues in reproducing the experimental results. In another study Foiles [9] also developed an alloy Cu-Ni potential where the fitting included only Cu, Ni pure element and Cu-Ni alloy properties. Although the potential successfully reproduces some surface alloy properties such as segregation, surface energies and also some bulk properties like mixing enthalpy and short-range ordering, there is still a need for betterment to correctly describe the phonon dispersions for metals with unfilled *d*-bands [11,12]. In addition, Zhou *et al.* [13] have reported an alloy potential database using elemental potentials, including Cu and Ni. In their formalism, an analytical expression [14] was used in developing pair interaction for alloys that include only the element functions with no parametrization and fitting to alloy properties. Such an approach might be quiet reasonable in developing a general purpose alloy potential which may naturally pose some challenges to correct observations of alloy properties. In this Thesis, thus the aim was to develop an accurate and highly optimized Cu-Ni alloy potential which produces reliable predictions for structural properties, energetics, phonons and thermodynamic functions of the alloy.

2. METHODS

In this chapter, the techniques used in this thesis to develop a reliable interaction potential for Cu-Ni alloys were presented in separate sections. In this context, the parallel implementation of Adaptive Particle Swarm Optimization(APSO) and the optimized charge density for the Embedded Atom Method (EAM) were the main focus of this Thesis.

2.1 Time Independent Schrödinger Equation in Born-Oppenheimer Approximation

In the most general form, the Time Independent Schrödinger Equation (TISE), that yields the electronic structure of a system constructed with electrons and nuclei, can be written as following:

$$H\Psi = E\Psi \tag{2.1}$$

where E is the electronic energy, Ψ is the wave function, and H is the Hamiltonian operator defined with

$$\begin{aligned} H = & -\frac{\hbar^2}{2m_e}\sum_i \nabla_i^2 - \sum_{i,I}\frac{Z_I e^2}{\left|\vec{r}_i - \vec{R}_I\right|} + \frac{1}{2}\sum_{i\neq j}\frac{e^2}{\left|\vec{r}_i - \vec{r}_j\right|} \\ & - \sum_I \frac{\hbar^2}{2M_I}\nabla_I^2 + \frac{1}{2}\sum_{I\neq J}\frac{Z_I Z_J e^2}{\left|\vec{R}_I - \vec{R}_J\right|}. \end{aligned} \tag{2.2}$$

Here, $\vec{R}$ denotes the nuclear coordinates, M_I is the mass of the nuclei and Z_I is the atomic mass of the nuclei, and $\vec{r}$ represents the coordinate of the electrons and m_e is the mass of the electron. The analytical solution to the above eigen-value problem exists only for hydrogen-like atoms. Likewise, the exact numerical solutions are limited to atoms or very small molecules. Full quantum mechanical formalism to solve the

Eqn. 2.2 is almost infeasible [15]. The most important issue is the two-body nature of the Coulomb interaction that makes the Schrödinger Equation inseparable. This problem can be tackle down using Born-Oppenheimer Approximation (BOA) [16]. The approximation is based on the relative motions of electrons with respect to the nuclei: since the motions of the electrons in a system are much faster than the heavier ions ($M_I >> m_e$), the nuclei can be considered as static particle within the time scale of the electronic motion. This suggestion is also known as adiabatic approximation and in this formalism, TISE can be split into the ionic and the electronic parts.

The Hamiltonian of the electronic system in this approximation is defined by

$$H_e = -\frac{\hbar^2}{2m_e}\sum_i \nabla_i^2 - \sum_{i,I}\frac{Z_I e^2}{\left|\vec{r}_i - \vec{R}_I\right|} + \frac{1}{2}\sum_{i\neq j}\frac{e^2}{|\vec{r}_i - \vec{r}_j|}. \tag{2.3}$$

Here, first term is the kinetic energy of electrons, second term represent the interactions of electrons with the external potential of ions located at the sites $\vec{R}_I$, and the last term is the interaction of electrons with each other.

2.2 Density Functional Theory (DFT)

The density functional theory (DFT) is a powerful method to solve the Schrödinger Equation for non-interacting electrons of quantum many-body problem. DFT has become the primary tool in condensed matter physics to solve the electronic structure of widespread systems from bulk structures down to the finite structures such as clusters or molecules. Theoretical foundation is based on the two important theorems and an *ansatz* established by Hohenberg and Kohn [17] and Kohn and Sham [10], respectively.

2.2.1 Hohenberg-Kohn theorems

The Hohenberg-Kohn (HK) theorems applies to a system of interacting particles of electrons and nuclei in an external potential $v_{ext}(\vec{r})$, where the Hamiltonian is given by

$$H = -\frac{h^2}{2m_e}\sum_i \nabla_i^2 + \sum_i v_{ext}(\vec{r}_i) + \frac{1}{2}\sum_{i\neq j}\frac{e^2}{|\vec{r}_i - \vec{r}_j|}. \tag{2.4}$$

For such systems with interacting particles of electrons, the two fundamental theorems are [17]:

> **Theorem I:** For any given system of interacting electrons in an external potential $v_{ext}(\vec{r})$, the potential $v_{ext}(\vec{r})$ can be determined by a unique functional of the electronic density of ground state $n_0(\vec{r})$, apart from a trivial additive constant.
>
> **Theorem II:** Independent of $v_{ext}(\vec{r})$, there exist a universal functional of density, $F[n(\vec{r})]$, such that the energy of the interacting particle system can be written as
>
> $$E_{HK}[n] = F_{HK}[n] + \int v_{ext}(\vec{r})n(\vec{r})d\vec{r} \tag{2.5}$$
>
> and the exact ground state energy of the system is the global minimum of the functional $E_{HK}[n]$ where the density $n(\vec{r})$ that minimizes the functional is the exact ground state density $n_0(\vec{r})$.

These two theorems can be simplified into a general corollary as follows: once the ground state density $n_0(\vec{r})$ of the given system is known, the functional $E_{HK}[n]$ is sufficient in determining all the properties of the system completely, except a constant shift in the energy. Although theorems provide mathematical basis for the solution of full many-body Schrödinger Equation, they do not give any method on how to solve the quantum many-body problem generally other than the original definition of many-body wavefunctions in HK proofs [17]. To accomplish that Kohn-Sham propose an *ansatz*.

2.2.2 Kohn-Sham equations

In Kohn-Sham *ansatz*, the quantum many-body problem is replaced by an independent particle problem by taking the ground state density of interacting system equal to the ground state density of a reference auxiliary non-interacting system. Since the exact kinetic energy of an interacting system can not be equal to that of the non-interacting system, a missing energy is added to define the correlation contributions. In the assumption of Kohn-Sham [10], the ground state energy of the electrons in non-interacting system is given by

$$E_{HK}[n] = T_R[n] + E_{xc}[n] + E_{Hartree}[n] + \int v_{ext}(\vec{r})n(\vec{r})d\vec{r}, \tag{2.6}$$

where $T_R[n]$ is the kinetic energy of non-interacting electrons in auxiliary reference system, $E_{xc}[n]$ is the energy of exchange and correlation contributions, and $E_{Hartree}[n]$ is the energy of the classical electrostatic interaction for the electron density $n(\vec{r})$ with itself and given by

$$E_{Hartree}[n] = \frac{1}{2}\int\int \frac{n(\vec{r})n(\vec{r}')}{\mid \vec{r}-\vec{r}' \mid} d\vec{r}d\vec{r}'. \tag{2.7}$$

Since the energy of the full interacting system in an external potential is given in terms of HK functional F_{HK}, the exchange and correlation term, E_{xc}, can be defined by

$$E_{xc} = F_{HK}[n] - T_R[n] - E_{Hartree}[n]. \tag{2.8}$$

As seen in the Eqn. 2.8, the exchange and correlation energy is a functional of density $n(\vec{r})$ for a true interacting many-body system in contrast to the non-interacting system where the electron-electron interactions are replaced by Hartree energy. Therefore, if the exact universal functional form of exchange-correlation energy, E_{xc}, is at hand the many-body interacting particles problem can be solved by using Kohn-Sham formulation. In fact the exact form of E_{xc} is rather complex and unknown. Therefore one can only solve the existing problem with some approximations that will be discussed in the next sections. The solution of the Kohn-Sham auxiliary system for the ground state can be calculated using variational principle [18]

$$\frac{\delta T_R[n]}{\delta n(\vec{r})} + v_{KS}(\vec{r}) = \mu \tag{2.9}$$

where μ is the chemical potential of non-interacting system which should coincide with the chemical potential of interacting system [15]. In Eqn. 2.9, the reference potential, $v_{KS}(\vec{r})$, of the auxiliary system is given by

$$\begin{aligned} v_{KS}(\vec{r}) &= v_{ext}(\vec{r}) + v_{Hartree} + v_{xc} \\ &= v_{ext}(\vec{r}) + \int \frac{n(\vec{r}')}{|\vec{r}-\vec{r}'|} d\vec{r}' + \frac{\delta E_{xc}[n]}{\delta n(\vec{r})}. \end{aligned} \tag{2.10}$$

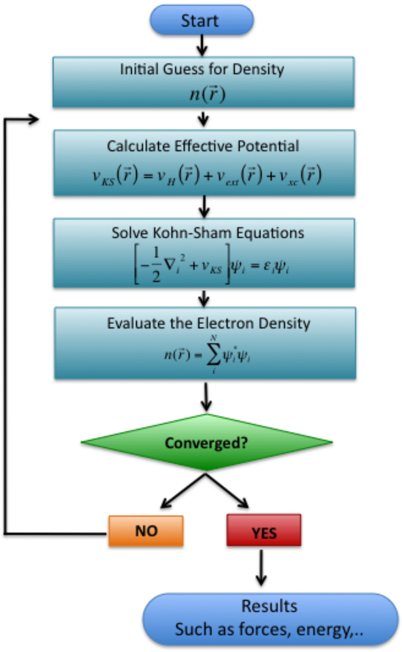
Start
Initial Guess for Density
$n(\vec{r})$
Calculate Effective Potential
$v_{KS}(\vec{r}) = v_H(\vec{r}) + v_{ext}(\vec{r}) + v_{xc}(\vec{r})$
Solve Kohn-Sham Equations
$\left[-\frac{1}{2}\nabla_i^2 + v_{KS}\right]\psi_i = \varepsilon_i\psi_i$
Evaluate the Electron Density
$n(\vec{r}) = \sum_i^N \psi_i^*\psi_i$
Converged?
NO
YES
Results
Such as forces, energy,..

Figure 2.1: Schematic representation of Khon-Sham Ansatz [15].

Using the variational principle to a fictitious auxiliary system of non-interacting electrons in an external potential $v_{KS}(\vec{r})$, the ground state density of the interacting electron system, $n_0(\vec{r})$, can be obtained by solving the following equation:

$$\left[-\frac{1}{2}\nabla^2 + v_{KS}(\vec{r})\right]\psi_i(\vec{r}) = \varepsilon_i\psi_i(\vec{r}). \tag{2.11}$$

Here the ground state has one electron in each of the N orbitals Ψ_i with the lowest eigenvalues ε_i. The density of the auxiliary system then can be calculated over all orbitals:

$$n(\vec{r}) = \sum_i^N \psi_i^*(\vec{r})\psi_i(\vec{r}). \tag{2.12}$$

The Equations 2.9, 2.10, and 2.11 are known as Kohn-Sham equations [10] and have to be solved self-consistently with such a ground state density that will construct v_{KS} functional (See Fig. 2.1). Note that these equations are independent of any exchange-correlation functional approximation to the ground state density.

2.2.3 The approximation to exchange-correlation energy

If the exchange-correlation functional, $E_{xc}[n]$ defined in Eqn. 2.7 were known, then exact ground state energy and density of the many-body electron problem could be obtained by the solving the Kohn-Sham equations for independent-particles. The most commonly used approaches to the exchange-correlation functional in DFT are the local density approximation (LDA) and the generalized gradient approximation (GGA).

2.2.3.1 Local density approximation

The simplest and most widespread approximation is the local density approximation which considers that the electron energy at each point in the system is the same as that of a uniform electron gas of the same density. In this approach, the exchange-correlation functional, $E_{xc}[n]$, can be defined as

$$E_{xc}^{LDA}[n] = \int \varepsilon_{xc}^{hom}(n(\vec{r}))n(\vec{r})d\vec{r}, \tag{2.13}$$

where $\varepsilon_{xc}^{hom}(n)$ is the exchange correlation energy per particle of a uniform electron gas of a density n. The exchange correlation potential is then given by

$$V_{xc}^{LDA}[n(\vec{r})] = \frac{\delta E_{xc}^{LDA}}{\delta n(\vec{r})} = \varepsilon_{xc}^{hom}(n) + n(\vec{r})\frac{\delta \varepsilon_{xc}^{hom}(n)}{\delta n}. \tag{2.14}$$

ε_{xc} can be split into exchange and correlation potentials, $\varepsilon_{xc} = \varepsilon_x(n) + \varepsilon_c(n)$. The exchange contribution can be evaluated analytically [18], while the correlation part has been obtained by parameterizing the results of Monte Carlo simulations [19–21]. LDA is successful for many system, especially those where the electronic density is quite uniform such as bulk metals, molecules, semiconductor and ionic crystal. LDA yields a good accuracy in reproducing experimental structural and vibrational properties of strongly bound systems. However, there is a number of features that the LDA is known to fail to reproduce. For instance, it usually overestimates bonding energies and under-estimates bond lengths [15].

2.2.3.2 Generalized gradient approximation

An improvement to LDA is made through consideration of the gradient of the electron density. This is called the generalized gradient approximation (GGA),

$$E_{xc}^{GGA}[n] = \int \varepsilon_{xc}^{GGA}(n(\vec{r}), |\nabla n(\vec{r})|) n(\vec{r}) d\vec{r} \tag{2.15}$$

which depends also on the norm of the local density gradient, $|\nabla n(\vec{r})|$. For the gradient correction to the exchange and correlation part of the energy $E_{xc}^{GGA}[n]$, there have been several parametrization schemes such as Perdew and Wang (PW91) [22], Perdew, Burke, and Enzerhof (PBE) [23]. In comparison with LDA, GGA tends to improve the total energies, atomization energies, energy barriers, and structural differences [15].

2.3 Embedded Atom Method (EAM)

Based on Density Functional Theory, described in the previous section 2.2, the interactions between the atoms in a system can be defined as a unique functional of the charge density of each atom in the crystal [10]. Hence, in such a crystal view, one can even further assume each atom as a defect in a lattice embedded into the electron charge density of the neighboring atoms [24] described by local density approximation [10]. Thus, one can write the energy of an ion at lattice site i for a given system as

$$E_i = \mathscr{F}_i[\boldsymbol{\rho_i}] \tag{2.16}$$

where $\mathscr{F}_i$ is a nonlinear functional of the charge density $\boldsymbol{\rho_i}$ at lattice site i in a crystal. Furthermore, one can simply extract the charge density for a system by any suitable *ab-initio* approximation, the functional $\mathscr{F}$ will still be far beyond to be defined by a simple analytical expression without further approximations. One such example is a *jellium* like uniform density approximation where the charge density around an atom changes slightly. With uniform density approximation and an analytical form of charge density function for each atom, $\mathscr{F}$ can be reduced to a plain function $F(\rho)$. Another important factor in correctly describing the interactions in a system is the ion-ion interactions as these long-range interactions prevent the local effects to be dominant in the system. Thus, a realistic description of energy of an ion in a system requires both the short- and long-range interactions.

In the embedded-atom method [7,8] the energy of an ion in a system is given by

$$E_i = F_{Z_i}(\bar{\rho}_i) + \frac{1}{2}\sum_{\substack{i,j \\ i\neq j}} \phi_{Z_iZ_j}(r_{ij}) \tag{2.17}$$

and the total energy of the system can be calculated by taking the sum over all atoms:

$$E_{tot} = \sum_i E_i. \tag{2.18}$$

The equation defining the energy of the ion has two parts: first part, $F(\bar{\rho}_i)$, is the many-body function defining the energy needed to embed an ion i into the background electron charge density at its specific site. Here, $\bar{\rho}_i$ is the host charge density which is taken to be superposition of electron densities of all ions of the Z_jth type within the cutoff radius, r_{cut}, of the ion i and given by

$$\bar{\rho}_i = \sum_{\substack{j \\ i\neq j}} \rho_{Z_j}(r_{ij}). \tag{2.19}$$

The second part, $\phi_{Z_iZ_j}(r_{ij})$, is the pair interaction between i and j ions separated by r_{ij} distance. The choice of ρ and ϕ functions highlights the type of EAM formalism. Among the various implementations, the three functional descriptions are the most commonly used: 1) all the EAM functions, ρ, ϕ and F, are defined with analytical expressions [25], 2) ϕ and one of the ρ and F are defined with an analytical expression and the other (ρ and F) is approximated with a spline [26,27], and 3) all of ρ, ϕ and F functions are defined in splines [28]. In all cases, the functions are parametrized and smoothly cutoff at a r_{cut} distance by fitting to the values in a database constructed with experimental or the *ab-initio* results .

The following function is utilized to implement the cutoff for potential functions:

$$h_{smooth}(r) = h(r) - h(r_{cut}) + \left(\frac{r_{cut}}{m}\right)\left[1 - \left(\frac{r}{r_{cut}}\right)^m\right]\left(\frac{dh}{dr}\right)_{r=r_{cut}} \tag{2.20}$$

where $m = 20$ as in Ref. [29]. Here, Eqn. 2.20 keeps the potential function and its first derivatives continuous, and thus provides the potential to generate values without any non-physical basis at cutoff.

The fitting procedure of EAM functions, introduced by Foiles *et al* [8] involves the following universal equation of state (EOS) [30].

$$E(x) = -E_{coh}\,(1 + x(a))\,e^{-x(a)} \tag{2.21}$$

where

$$x(a) = (a/a_0 - 1)\,(E_{coh}/9\Omega_0 B)^{-1/2} \tag{2.22}$$

and the parameters a_0, Ω_0, B and E_{coh} are the lattice constants, atomic volume, bulk modulus, and cohesive energy, respectively, for the equilibrium *fcc* crystal at 0K. The crystal energies for different lattice constants calculated with EOS are in most cases directly used on the left hand side of Eqn. 2.17.

The fitting database in EAM is usually constructed with the experimental values for the energetic and structural constants of the elements and alloys. In absence of experimental results, the database is completed using *ab-initio* calculations. Mostly, the database includes cohesive and minimum energies of several crystal structures, lattice constants, bulk modulus, elastic constants, vacancy formation energies, adatom or vacancy migration energies, phonon frequencies, stacking fault and interstitial energies, surface energies and diatomic bond length and energy. Searching an optimum set for the parameters is itself relatively time consuming process. Approximating the EAM functions with splines, instead of an analytical expression, requires even a more complex optimization technique as the splines need an optimum number of knots for the fitting process. If the fitting process is carried out by not an optimal number of knots, then the EAM functions may have an oscillating characteristics, and thus may not correctly describe the other properties that are not involved in the database. The desired solution to the problem is to define an analytical expression for each EAM function with a physical background. Therefore, aside from the fitting procedure, the testing of the functions is essential to maintain a reliable potential that produces results in agreement with the experiments and *ab-initio* calculations. Such tests should include energetics and structural properties that are not used in the database like phonon dispersion curves, surface and stacking fault energies, barriers for various diffusions mechanisms in the bulk/on the surfaces, and thermodynamical properties at elevated temperatures.

For generating an alloy potential in EAM, there are two approaches: First is to simultaneously fit the potential to the properties and energies of the alloy and its pure elements. However, the method generally fails in accurately reproducing the desired elemental and the alloy properties [29]. The second and more accurate approach [29] is to optimize the pure element potential functions first and then use them in alloy potential generation without changing the fitted properties of the pure element part in the potential. Therefore for a binary system of AB, first, the potential functions for pure A and B element, ϕ_{AA}, ρ_A, F_A and ϕ_{BB}, ρ_B, F_B are fitted to determine the parameters of functions and r_{cut} for each element using Eqns. 2.17, 2.19, 2.20, 2.21, and 2.22 with $Z_i = Z_j$. In the second part involving generation of alloy potential, only is the pair potential, ϕ_{AB}, to be fitted to the properties of alloys. For that, the pair potentials are constructed using the two types of transformations on the pure element potential functions: shifting by

$$F'_Z(\bar{\rho}) = F_Z(\bar{\rho}) + G_Z\bar{\rho} \tag{2.23a}$$

$$\phi'_{ZZ}(r) = \phi_{ZZ}(r) - 2G_Z\rho_Z(r) \tag{2.23b}$$

and scaling by

$$\rho'_Z(r) = S_Z\rho_Z(r) \tag{2.24a}$$

$$F'_Z(\bar{\rho}) = F_Z(\bar{\rho}/S_Z), \tag{2.24b}$$

where Z stands for one of A or B element and S_A, S_B, G_A, and G_B are the fitting parameters. Eqns. 2.23a, 2.23b, 2.24a and 2.24b ensure that the pure element energies do not change under the transformations while the alloy energy does, and thus helps increasing the quality of the alloy potential in the fitting. It is also important to note that the transformations are used in the order in which scaling is applied after shifting. Since scaling the charge density of ρ is sufficient for one of the element against the other one, the parameter S_A is generally chosen to be 1 in the alloy fitting. Similar to the approach in the pure element potential fitting, the parameters of pair function ϕ_{AB} and the scaling and shifting parameters are fitted to the experimental or *ab-initio* results for lattice constants, cohesive energies, bulk modulus, elastic constants of considered A-B alloys, and also can be fitted to the bonding lengths and energies of A and B atoms in various structures.

2.4 The Calculation of Structural Constants and Energies in EAM

For the calculation of structural constants and energies of a system in the formalism of EAM, one should first, write the force in terms of EAM functions by taking derivatives of Eqn. 2.17 with respect to $\vec{r}_{ij}$

$$\vec{\mathfrak{F}}_i = -\nabla E_i(r_{ij}) = -\left(\frac{\partial E_i}{\partial r_{ij}^x}\frac{r_{ij}^x}{r_{ij}} + \frac{\partial E_i}{\partial r_{ij}^y}\frac{r_{ij}^y}{r_{ij}} + \frac{\partial E_i}{\partial r_{ij}^z}\frac{r_{ij}^z}{r_{ij}}\right) \tag{2.25}$$

which yields

$$\mathfrak{F}_i^m = \sum_{\substack{j \\ i\neq j}} \left[\phi'_{Z_iZ_j}(r_{ij}) + F'_{Z_i}(\bar{\rho}_i)\rho'_{Z_j}(r_{ij}) + F'_{Z_j}(\bar{\rho}_i)\rho'_{Z_i}(r_{ij})\right]\frac{r_{ij}^m}{r_{ij}}. \tag{2.26}$$

Here r_{ij}^m is the component of separation between atom i and the neighboring atom j along the direction m where m is the one of the Cartesian coordinates; x, y, z. $\mathfrak{F}_i^m$ represents the force acting on the atom i in the same direction m. To find the equilibrium configuration of the system, the atomic positions are optimized such that the force on each atom is zero. Using this equilibrated structure, one can easily calculate the minimum energy of the system or the energy of a configuration such as stacking fault, interstitial site, surface.

In EAM method, the mechanical stress tensor for an individual atom i can be defined by

$$\sigma_i^{mn} = \frac{1}{\Omega_0} \sum_{j,j\neq i} \left[\frac{1}{2} \phi'_{Z_i Z_j} + F'_{Z_i}(\bar{\rho}_i) \rho'_{Z_j}(r_{ij}) \right] \frac{r_{ij}^m r_{ij}^n}{r_{ij}} \tag{2.27}$$

where m, and n are the tensor elements and can be one of 1, 2, or 3 representing x, y, and z directions, respectively.

The elastic constants of an equilibrium crystal can be calculated by applying an infinitesimal homogeneous strain Δr_{ij} to the crystal. Using generalized Hooke's law for linear deformations, the stress tensor definition can also be written in the following form [31]

$$\sigma^{mn} = C_{mnkl} \Delta r_{ij}^{kl} \tag{2.28}$$

where C_{mnkl} is the elasticity tensor. Second derivative of the crystal energy in Eqn. 2.18 leads to elastic constant tensor C_{mnkl} for the crystal:

$$C_{mnkl} = \frac{\partial (E_{tot}/\Omega_0)}{\partial r^{mn} \partial r^{kl}} = \frac{1}{n_b \Omega_0} \sum_i \left[M_i^{mnkl} + F'_i(\bar{\rho}_i) N_i^{mnkl} + F''_i(\bar{\rho}_i) L_i^{mn} L_i^{kl} \right] \tag{2.29}$$

where Ω_0 is the atomic volume, n_b is the number of basis defining the conventional unit cell of the structure and

$$M_i^{mnkl} = \frac{1}{2} \sum_{i\neq j} \left[\left(\phi''_{Z_i Z_j}(r_{ij}) - \frac{\phi'_{Z_i Z_j}(r_{ij})}{r_{ij}} \right) \frac{r_{ij}^m r_{ij}^n r_{ij}^k r_{ij}^l}{(r_{ij})^2} \right], \tag{2.30}$$

$$N_i^{mnkl} = \sum_{i\neq j} \left[\left(\rho''_{Z_j}(r_{ij}) - \frac{\rho'_{Z_j}(r_{ij})}{r_{ij}} \right) \frac{r_{ij}^m r_{ij}^n r_{ij}^k r_{ij}^l}{(r_{ij})^2} \right], \tag{2.31}$$

$$L_i^{mn} = \sum_{i\neq j} \rho'_{Z_j}(r_{ij}) \frac{r_{ij}^m r_{ij}^n}{r_{ij}}. \tag{2.32}$$

Here, the fourth-order elastic tensor C_{mnkl} has the following symmetries:

$$C_{mnkl} = C_{nmkl} = C_{mnlk} = C_{nmlk} \tag{2.33}$$

Therefore, the only independent elements in the tensor are reduced to 21 elements from 81. Using Voigt's notation [32], elastic tensor can be written as $C_{\alpha\beta}$, where α and β

have values from 1 to 6 and define *xx*, *yy*, *zz*, *yz*, *xz*, and *xy*, respectively. The elements can be further reduced using the symmetries defining the crystal. In a cubic lattice, the symmetries impose that the stress contribution in any given direction is the same as the other directions such as $C_{11} = C_{22} = C_{33}$. Using the symmetry definitions and the similarities, one can reduce the independent elements to C_{11}, C_{12}, and C_{44}. This kind of reduction can also be utilized for a hexagonal lattice for which C_{13}, C_{33}, and C_{66} elements are to be independent in addition to the tensor elements of cubic lattice.

The bulk modulus of a material can be calculated using the equation of state for an *fcc* lattice given by Eqns. 2.21 and 2.22:

$$B = \Omega_0 \frac{\partial^2 E_i}{\partial {\Omega_0}^2} = \frac{r_{ij}^2}{9\Omega_0} \frac{\partial^2 E_i}{\partial r_{ij}^2}. \qquad \textbf{(2.34)}$$

Both using Eqn. 2.34 and $\sum_m \sigma^{mm} = 0$ (the hydrostatic stress condition for an equilibrium crystal) the bulk modulus can be expressed in terms of potential functions as following

$$B = \frac{1}{9\Omega_0} \left[\frac{1}{2} \sum_{j,j\neq i} \phi''(r_{ij})(r_{ij})^2 + F'(\bar{\rho}) \sum_{j,j\neq i} \rho''(r_{ij})(r_{ij})^2 + F''(\bar{\rho}) \left(\sum_{j,j\neq i} \rho'(r_{ij}) r_{ij} \right) \right]. \qquad \textbf{(2.35)}$$

In EAM formalism vacancy formation energy is defined as follows

$$E_{vac}^f = -\frac{1}{2} \sum_j \phi + \sum_j \left[F(\bar{\rho} - \rho_j) - F(\bar{\rho}) \right] + E_{relax}. \qquad \textbf{(2.36)}$$

Here the sum is over the atoms in the vicinity of the vacancy site. The first term represents the decrease in pair potentials of the neighboring atoms around the vacant site, whereas the second term is the change in the embedding energies of the neighboring atoms introduced by existence of vacancy. E_{relax} is the relaxation energy of the neighboring atoms in the absence of an atom in a lattice site. For metals, this energy is relatively small [33] and is around 0.01 eV [7] which is in the error bars of vacancy energy in the optimization procedure, and thus is usually ignored in the expression.

2.5 Phonon Dispersions

In lattice dynamics, one needs to solve the equations of motion for ions in the unit cell:

$$M_i \frac{\partial^2 \vec{R_{ic}}}{\partial t} = \vec{F_{ic}} = -\frac{\partial E_{tot}}{\partial \vec{R_{ic}}}. \tag{2.37}$$

Here $\vec{R_{ic}}$ is the equilibrium position of atom i in the unit cell c and $\vec{F_{ic}}$ is the total force acting on the atom in the system with a potential energy E_{tot}. For a dynamic crystal, where all atoms vibrate around their respective equilibrium positions, the position vector of an ion is time-dependent:

$$\vec{r_{ic}}(t) = \vec{R_{ic}} + \vec{u_{ic}}(t), \tag{2.38}$$

where $\vec{u_{ic}}(t)$ is the displacement of atom i from its equilibrium position of $\vec{R_{ic}}$ in the unit cell. If the displacements of the atoms are small in comparison with the lattice spacing a_0, then the potential energy E_{tot} of the system can be expanded around the equilibrium state:

$$E_{tot}(\vec{r_{ic}}) = E_{tot}(\vec{R_{ic}}) + \sum_{ic} \frac{\partial E_{tot}}{\partial \vec{u_{ic}}} \vec{u_{ic}} + \sum_{ic} \frac{\partial^2 E_{tot}}{\partial \vec{u_{ic}} \partial \vec{u_{jc'}}} \vec{u_{ic}} \vec{u_j c'} \ldots \tag{2.39}$$

Under equilibrium conditions where the total force on the system is zero, the second term vanishes. For small displacements, the potential energy of the perturbed system is relatively close to the equilibrium energy. Thus, the second-order term in Eqn. 2.39 is to be the dominant contribution to the lattice dynamics when the higher-order terms are neglected. Under such approximation, the form of the energy turns into that of a series of harmonic oscillators and this approach is called *harmonic approximation*.

In harmonic approximation of the lattice dynamics, the solution of Eqn. 2.37 has a traveling wave form:

$$\vec{u_{ic}} = M_i^{1/2} \tilde{U_{ic}}(\vec{q}) e^{i(\vec{q} \cdot \vec{r_i c} - wt)} \tag{2.40}$$

where $\vec{q}$ is the wave vector, w is the angular frequency, and $\tilde{U_{ic}}$ is the amplitude of the wave. With substitution of u_{ic} in Eqn. 2.37, the equation of motion takes the following form

$$-w^2\tilde{U_{ic}^m}(\vec{q}) + \sum_{c}\sum_{c'} \frac{1}{(M_iM_j)^{1/2}} \Phi_{ij}^{mn} exp\left(iq \cdot (r_{ic} - r_{jc'})\right) \tilde{U_{jc'}^n} = 0. \tag{2.41}$$

As the distance between the two atoms in the system is given by

$$\vec{r_{ic}} = a_0 + (\vec{u_{ic}} - \vec{u_jc'}) \tag{2.42}$$

where $r_{ic} - r_{jc'} = \vec{r_{ij}}$, the second derivative involved in the term Φ_{ij}^{mn} can be expressed in terms of relative distances

$$\frac{\partial^2 E_{tot}}{\partial \vec{u_{ic}} \partial \vec{u_{jc'}}} = \frac{\partial^2 E_{tot}}{\partial \vec{r_{ic}} \partial \vec{r_{jc'}}}. \tag{2.43}$$

The phonon frequencies then can be calculated by diagonalizing the dynamical matrix

$$D_{mn,ij} = \frac{1}{(M_iM_j)^{1/2}} \sum_{c'} \Phi_{ij}^{mn} exp\left(iq \cdot (r_{ic} - r_{jc'})\right). \tag{2.44}$$

Here, Φ_{ij}^{mn} is the force constant and given by

$$\begin{aligned}
\Phi_{ij}^{mn} &= \frac{\partial E_{tot}}{\partial r_{ij}^m \partial r_{ij}^n} = -\frac{\delta_{mn} f_{ij}(r_{ij})}{r_{ij}} - \left[\phi''_{Z_iZ_j}(r_{ij}) - \frac{\phi'_{Z_iZ_j}(r_{ij})}{r_{ij}}\right] \frac{r_{ij}^m r_{ij}^n}{(r_{ij})^2} \\
&- F'_{Z_i}(\bar{\rho}_i) \left[\rho''_{Z_j}(r_{ij}) - \frac{\rho'_{Z_j}(r_{ij})}{r_{ij}}\right] \frac{r_{ij}^m r_{ij}^n}{(r_{ij})^2} \\
&- F'_{Z_j}(\bar{\rho}_j) \left[\rho''_{Z_i}(r_{ij}) - \frac{\rho'_{Z_i}(r_{ij})}{r_{ij}}\right] \frac{r_{ij}^m r_{ij}^n}{(r_{ij})^2} \\
&+ F''_{Z_j}(\bar{\rho}_j)\rho'_{Z_i}(r_{ij}) Q_j^n \frac{r_{ij}^m}{r_{ij}} - F''_{Z_i}(\bar{\rho}_i)\rho'_{Z_j}(r_{ij}) Q_i^m \frac{r_{ij}^n}{r_{ij}} \\
&+ \sum_{i \neq k,j} F''_{Z_k}(\bar{\rho}_k)\rho'_{Z_i}(r_{ik})\rho'_{Z_j}(r_{jk}) \frac{r_{ik}^m r_{jk}^n}{r_{ik} r_{jk}}. \qquad (2.45) \\
& \qquad (2.46)
\end{aligned}$$

where

$$Q_j^n = \sum_{s \neq j} \rho'_{Z_s}(r_{sj}) \frac{r_{sj}^n}{r_{sj}}, \quad \textbf{(2.47)}$$

$$f_{ij} = \phi_{Z_i Z_j}(r_{ij}) + F'_{Z_i}(\bar{\rho}_i)\rho'_{Z_j}(r_{ij}) + F'_{Z_j}(\bar{\rho}_j)\rho'_{Z_i}(r_{ij}), \quad \textbf{(2.48)}$$

and E_{tot} is sum over all ionic energy in Eqn. 2.17. M_i, M_j are the masses of atoms labeled i, j in the reference unit cell c and the sum in Eqn. 2.44 is over all the neighboring c' unit cells.

2.6 Molecular Dynamic Simulations (MD)

Molecular Dynamic Simulation (MD) is an iterative method based on classical mechanics that gives the time evolution of a system of atoms in a time interval dictated by the interaction potential. In MD, the time evolution of a system is provided by solving Newton's equation of motion for each individual atom in an isolated system consisting N atoms with constant volume (V) and constant total energy (E). Such an isolated system in statistical mechanics is known as *microcanonical* ensemble (NVE). In NVE, the position update of an atom i is calculated from the force on the atom, $\vec{F}_i$, which is the first derivative of the total energy with respect to atomic position:

$$\vec{F}_i(t) = m\ddot{\vec{r}}_i(t) = -\frac{\partial U(\vec{r}N)}{\partial \vec{r}_i}. \quad \textbf{(2.49)}$$

where $\ddot{\vec{r}}_i$ is the acceleration of atom i with mass m, and U is the interatomic potential describing the interactions between the atoms in the system. The positions of the atoms are then evaluated by numerically taking simultaneous integration of the equation of motion of each atom and for each time step, the new configuration of the system is obtained through an iterative solution of the Eqn. 2.49. In T=0K simulations where atoms have been set with initial-zero velocities, the total energy of the system is simply equal to the potential energy of the system. However, for elevated temperature simulations where atoms have non-zero initial velocities specific to the assigned temperature, total energy involves kinetic energy contribution as well. In such systems, the kinetic energy of each atom at every integration step can be calculated by

$$E_i^K(t) = \frac{1}{2}m(\dot{\vec{r}}_i(t))^2 = \frac{[\vec{p}_i(t)]^2}{2m} \cdot \tag{2.50}$$

where $\vec{r}(t)$ and $\vec{p}(t)$ are the position and the momentum of the atom i, respectively. In a system, as the motions of atoms are not independent of each other, the equations of motion for the atoms are coupled. Therefore, one needs to count on numerical methods to solve theses coupled differential equations. In this study, the integration algorithm performed in MD simulations is based on the Verlet finite difference method [34]. In the method, using Taylor series expansion the atomic positions $\vec{r}(t+2\Delta t)$, $\vec{r}(t+\Delta t)$, $\vec{r}(t-\Delta t)$, and $\vec{r}(t-2\Delta t)$ can be given in the following forms,

$$\begin{aligned}
\vec{r}(t+2\Delta t) &= \vec{r}(t) + 2\dot{\vec{r}}(t)\Delta t + \frac{\ddot{\vec{r}}(t)(2\Delta t)^2}{2!} + \frac{\dddot{\vec{r}}(t)(2\Delta t)^3}{3!} + \cdots \\
\vec{r}(t+\Delta t) &= \vec{r} + \dot{\vec{r}}(t)\Delta t + \frac{\ddot{\vec{r}}(t)(\Delta t)^2}{2!} + \frac{\dddot{\vec{r}}(t)(\Delta t)^3}{3!} + \cdots \\
\vec{r}(t-\Delta t) &= \vec{r}(t) - \dot{\vec{r}}(t)\Delta t + \frac{\ddot{\vec{r}}(t)(\Delta t)^2}{2!} - \frac{\dddot{\vec{r}}(t)(\Delta t)^3}{3!} \cdots \\
\vec{r}(t-2\Delta t) &= \vec{r}(t) - 2\dot{\vec{r}}(t)\Delta t + \frac{\ddot{\vec{r}}(t)(2\Delta t)^2}{2!} - \frac{\dddot{\vec{r}}(t)(2\Delta t)^3}{3!} \cdots
\end{aligned} \tag{2.51}$$

By reorganizing the above set of equations, one obtains the following expression for the velocity:

$$12\dot{\vec{r}}(t)\Delta t = 8[\vec{r}(t+\Delta t) - \vec{r}(t-\Delta t)] - [\vec{r}(t+2\Delta t) - \vec{r}(t-2\Delta t)] + O(\Delta t^4) \cdot \tag{2.52}$$

Using the Eqn. 2.51, the velocity of an atom becomes

$$\dot{\vec{r}}(t) = \frac{\dot{\vec{r}}(t+\Delta t/2) + \dot{\vec{r}}(t-\Delta t/2)}{2} + \frac{\Delta t}{12}[\ddot{r}(t-\Delta t) - \ddot{\vec{r}}(t+\Delta t)] + O(\Delta t^4) \tag{2.53}$$

and the position associated with the atom is then calculated as follows

$$r(t+\Delta t) = r(t) + \dot{r}(t)\Delta t + \frac{4F(t) - F(t-\Delta t)}{6m}\Delta t^2 \cdot \tag{2.54}$$

At thermodynamic equilibrium, the total energy of the system in the phase space is given by

$$E = E_K(p^N) + U(r^N) = constant. \tag{2.55}$$

In the NVE simulations, since the kinetic energy as well as the potential energy oscillate around the equilibrium condition of the system, the kinetic energy of the system is the average of the oscillations within a time interval;

$$\langle E_K \rangle = \lim_{t\to\infty} \frac{1}{t} \int_{t_0}^{t_0+t} E_K(p^N) d\tau = \frac{3}{2} N k_B T. \tag{2.56}$$

where t is the integration time step, t_0 is the initial time, N is the total number of atoms, k_B is the Boltzman constant, and T is absolute temperature. The key step in performing realistic MD simulations is to choose an appropriate time-step (Δt), as the accuracy of the above numerical derivations are dictated by the time-step. In general, smaller time-steps close to machine precisions leads to senseless results and unnecessary cost to computations. On the other hand, large time-steps may lead to inconsistent evolution of the systems where the motion of atoms is rather fast compared to the change in the total energy. In this study, the simulation time unit is taken in the order of picoseconds and the time-step of 1 femtosecond is found to be sufficient to produce consistent modeling of the material characteristics.

In this Thesis, the other studied statistical ensemble is the *canonical* ensemble, where the number of atoms N, the volume V, and the temperature T in the system are held constant (NVT). In NVT simulations, the atoms in the system are initially started with a random velocity and then the system is thermalized with a thermal reservoir. The evaluation of the system at a temperature T can also be performed by keeping the total energy constant (NVE simulation). For all MD simulations performed in this thesis, the temperature is maintained fixed through a Nose-Hoover thermostat [35,36].

2.7 Nudged Elastic Band Method (NEB)

While an atom or a group of atoms moves from one stable configuration to another, its reaction path always has the lowest energy in the process. This path is known as the minimum energy path (MEP) and is used to define a reaction coordinate for transitions from one configuration to another as in diffusion processes in solids. The highest

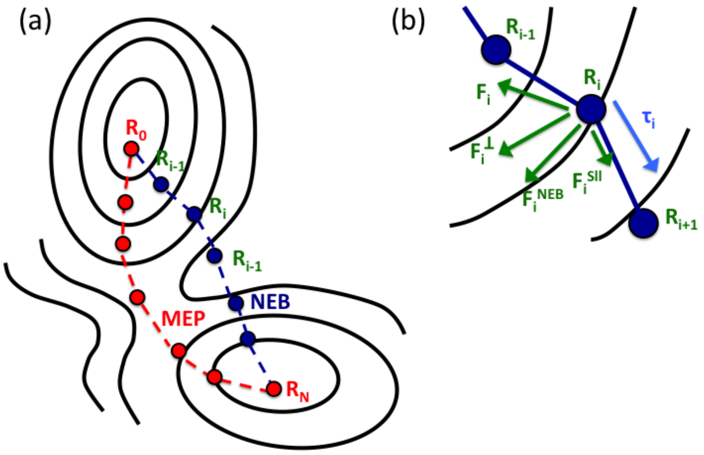

Figure 2.2: Illustration of the NEB method: (a) The images are generated along the blue line interpolation between initial state, R_0, and final state, R_N. The NEB method apply F_i^{NEB} force during the optimization to relax the images on to the true MEP. (b) The force components along the reaction path: F_i^{NEB} is the nudged elastic band force, $F_i^{\perp}$ is the perpendicular force of F_i due to the $V(R)$ potential, $F_i^{S||}$ shows the spring force parallel to tangent $\hat{\tau}_i$ [38,39].

potential energy obtained along the MEP is the saddle point energy which is also the activation energy barrier for the transition state. Among all the other methods [37], the nudged elastic band (NEB) technique has proven to be quite accurate and efficient in determining the minimum energy path, and thus the activation energy barriers for the diffusion processes once the initial and final states of the process are known [38,39]. The method generates the *chain of states* or in other words the *images* of the system for the intermediate states in the configurational space. In the method, each *state* (or *image*) corresponds to a specific atomic configuration of the system in between the initial state and the final state. The minimum energy path is then identified by carrying out a simultaneous optimization procedure throughout all these intermediate images.

In the method, the set of $N+1$ images, indicated by $[\vec{R}_0, \vec{R}_1, \vec{R}_2, ..., \vec{R}_N]$, generates an elastic band with the spring constant k_S (See Fig. 2.2) . While the end-points, R_0 and R_N, are kept fixed at given initial and final states, the remaining intermediate images are adjusted by the optimization algorithm. The minimization of the elastic band is carried out by projecting the perpendicular component of the spring force and the parallel component of the true force F_i in all *images*. The effective force on the image i is then given by

$$\vec{F}_i^{NEB} = \vec{F}_i^{\perp} + \vec{F}_i^{S_{\parallel}} \cdot . \tag{2.57}$$

Since $\hat{\tau}_i$ is the unit tangent along the path at each image, the perpendicular component of true force then is to be evaluated as

$$\vec{F}_i^{\perp} = -\vec{\nabla} V(\vec{R}_i) + \vec{\nabla} V(\vec{R}_i) \cdot \hat{\tau}_i \hat{\tau}_i, \tag{2.58}$$

where $\vec{\nabla} V(\vec{R}_i)$ is the gradient of the energy with respect to the atomic coordinates in each image of the system. The spring forces between the images of system, on the other hand, is formed by

$$\vec{F}_i^{S_{\parallel}} = k_S(\left|\vec{R}_{i+1} - \vec{R}_i\right| - \left|\vec{R}_i - \vec{R}_{i-1}\right|)\hat{\tau}_i \tag{2.59}$$

where the same spring constant, k_S, is used for all the springs acting on neighboring images. The projection, here, including the perpendicular component of true force and the parallel component of the spring force is referred as *nudging*. This *nudging* action is applied by the NEB force F_i^{NEB}, during the optimization procedure until the initial *chain of states* is fall on to the MEP passing through the saddle point with minimum energy (See Fig. 2.2(a)).

2.8 Real Space Green's Function Method for Vibrational Local Density of States

Investigating vibrational or electronic states of a solid involve calculations of the eigenvalue problem, $Hu = Eu$, or equivalently the Green's functions corresponding to the Hamiltonian, H. In the case of vibrational density of states of a solid, one may directly diagonalize the dynamical matrix portraying the interactions between the atoms in N layers of slab instead of finding the Green's function corresponding to the Hamiltonian. This approach is called the slab method and is the most commonly used technique to obtain the frequency spectrum for a solid with or without surface in k-space. In many cases the calculations are easily be carried out for systems with high symmetries such as bulk systems with no defects. On the other hand, for systems with reduced symmetries which require large computational cells, slab method calculations become costly. If ones interest lies in calculating vibrational spectrum for a local region of interest in real space, then one has to obtain the Green's function corresponding to the Hamiltonian. However, for large systems, systems with atoms of the order of thousands, obtaining the Green's function is a formidable task, as the interaction matrix H is order of $3Nx3N$, where N is the number of atoms in the system and the Green's function associated with it is defined as $G = (zI - H)^{-1}$. The continued fraction method proposed by Haydock [40] is the pioneering recursive method to circumvent such problems for complex systems requiring big interaction matrix H. Although the continued fraction method is a local approach in real space, it is not an efficient technique to follow, as the Green's function corresponding to predefined locality is written in a continued fraction form and one has to enforce a truncation for the level of coefficients of the continued fraction which in turn leads to the inaccuracies in the calculations.

Another local approach in real space is the real space Green's function (RSGF) method [41] . In this method one can focus on any *local* region according to ones need and analyse the effect of the rest of the system on that particular region. Also there is no need for the system to be periodic and it is, thus, particularly suitable for studying local vibrational density of states in complex systems with defects, disorder, and reduced symmetry. The only prerequisite is that the interatomic potential between the atoms in the system be of finite range, as it is then possible to write the force constant matrix in a block-tridiagonal form in which the sub-matrices along the diagonal represent interactions between atoms within a chosen local region and the sub-matrices in the 'off-diagonal' corresponds to interactions between neighboring localities. Thus, the method allows one to work with much smaller matrices, whose dimensions are defined by the subsystems, rather than the interaction matrices for entire system. Since an infinite/semi-infinite system is converted quite naturally into an infinite/semi-infinite set of local regions, there is no a priori truncation on the system size, as would be the case for matrix diagonalization methods based on k-space. The RSGF method also has an advantage over the continued fraction method as it does not involve truncation schemes to determine the recursion coefficients, rather a more general and simpler recursive scheme is applied.

Using the resolvent matrix method [42] in RSGF, the force constant matrix of a system can be given by block-tridiagonal form as following

$$H = \begin{pmatrix} \ddots & & & \\ v_{i,j-1} & h_i & v_{i,j+1} & \\ & v_{i+1,j-1} & h_{i+1} & v_{i+1,j+1} \\ & & & \ddots \end{pmatrix} \tag{2.60}$$

where the sub-matrix h_i involves the interactions of the atoms within the local region, and $v_{i,i+1}$ is the one between the local region and the neighboring regions. Then, the Green's functions associated with the H matrix is given by the resolvent operator, $G(z) = (zI - H)^{-1}$, for the eigenstates where $z = w^2 + i\varepsilon$, ε being the width of Lorentzian representing the delta function at w^2, and I is a unit matrix of the same size as that of H. The diagonal(ii) and off-diagonal(ii') elements of Green's functions leading the formal solution of the problem are obtained by Dy, Wu, and Spratlin [42] as

$$\begin{aligned} G_{ii}(z) = & \quad [(zI_i - h_i) - v_{i,i+1}\Delta^{+}_{i+1}v_{i+1,i} \\ & \quad -v_{i,i-1}\Delta^{-}_{i-1}v_{i-1,i}]^{-1}, \\ G_{ii'}(z) = & \quad G_{ii}v_{i,i\pm1}\Delta^{\pm}_{i\pm1}\cdots v_{i'\pm1,i'}\Delta^{\pm}_{i'},\ (i' \lessgtr i), \\ \Delta^{\pm}_{i}(a) = & \quad \left[(zI_i - h_i) - v_{i,i\pm1}\Delta^{\pm}_{i\pm1}v_{i\pm1,i}\right]^{-1}. \end{aligned} \tag{2.61}$$

In addition, the relation between the diagonal elements of the Green's function matrix G_{ii} and $G_{i\pm1,i\pm1}$ defined by

$$G_{ii} = \Delta^{\mp}_{i} + \Delta^{\mp}_{i}v_{i,i\pm1}G_{i\pm1}, i \pm 1 v_{i\pm1,i}\Delta^{\mp}_{i}. \tag{2.62}$$

Here, Eqns. 2.61 and Eqn. 2.62 reduce the calculation of Green's function to a series of inversions and multiplications of matrices that determine the interactions of atoms in the local region. Using the equations recursively, the Green's functions can be calculated in an accuracy of a desired tolerance. Once the Green's function of the local region of interest is calculated, then the normalized vibrational density of states (DOS) is obtained through

$$N_i(\omega) = 2\omega g_i(\omega^2) \tag{2.63}$$

where w is the vibrational frequency and the function $g_i(\omega^2)$ satisfies the equation

$$g_i(\omega^2) = -\frac{1}{3N_i\pi} \lim_{x\to\infty} \{Im[Tr(G_{ii}(\omega^2 + i\varepsilon))]\} \tag{2.64}$$

Here, G_{ii} is the Green's function sub-matrix associated with locality i and N_i is the number of atoms in this locality.

2.9 Adaptive Particle Swarm Optimization (APSO)

The adaptive particle swarm optimization (APSO) is an improved version of the particle swarm optimization method (PSO) [43] developed by Kennedy et al. in 1995. In PSO, the minimum of a given function or function set is searched in a procedure that mimics the behavior of the swarm such as groups of flocks or fishes. Like other evolution based algorithms such as genetic algorithm, PSO binds individuals to a community. The functions that determine the behavior of the individuals have to be evaluated numerous times repeatedly. Each individual is taken as a parameter set of the desired function to be minimized and dedicated to a particle in the solution space whose dimensions are constrained with the number of parameters. The basic idea of PSO algorithms is to evolve each particle towards the optimum of the parameter space using two contributions; 1) their best fitted parameters in the past, *pBest* and 2) the best fitted particle in the swarm, *gBest* given by the iterative algorithm:

$$\begin{aligned} v_i^d &= \omega v_i^d + c_1 R_1^d \left(pBest_i^d - x_i^d\right) + c_2 R_2^d \left(gBest_i^d\right), \\ x_i^d &= x_i^d + v_i^d, \end{aligned} \tag{2.65}$$

where x_i^d and v_i^d are the position and the velocity components in d dimension ($d = 1,2,3,\ldots,D$) of the ith particle, respectively. Moreover in Eqn. 2.65, ω, is the weighting factor for the previous velocities, c_1 and c_2 are the factors of cognitive and social parts of the equation, and R_1 and R_2 are the random numbers between $[0,1]$ in each step of generation. The optimization is carried out with typically hundreds of particles each treated as a parameter set where $X_i = [x_i^1, x_i^2, x_i^3, \dots, x_i^d]$ is the position vector and $V_i = [v_i^1, v_i^2, v_i^3, \dots, v_i^d]$ is the velocity vector that is initialized randomly in the D dimension parameter space. The previous best position of a particle and the globally the best particle are respectively the self and the social learning parts of the individuals in a society. Here, what PSO algorithm does is to simply provide the learning mechanism for each individual in the swarm. In the early PSO implementations, the learning parameters c_1, c_2 and the weighting factor ω are taken as fixed numbers through all the steps of the optimization. Determining the weights of the two learning contributions are generally hard to get a better fitting of the functions and the parameters generally change according to the type of the problem that is to be solved [44]. Therefore, the fixed evolution rates and the simplicity of PSO hinders the swarm to escape from local minimum in small number of generation steps.

To circumvent the drawbacks of PSO algorithm, adaptive particle swarm optimization (APSO) technique is introduced by Zhan et al. in 2009 [45]. In APSO method, the early convergence to false minimum is avoided through the use of fuzzy logic circuits and adaptive evolution algorithms. The adaptive weighting factor, c_1 and c_2 evolution rates are determined by the evolutionary states estimation (ESE) procedure and the evolution factor, f. In each step, the ESE stage is evaluated before the position and velocity vectors are calculated. In this stage, the state of the swarm is constructed on four different scenarios: S_1, *exploration*, S_2, *exploitation*, S_3, *convergence* and S_4, *jump-out*. The states are calculated by taking the average distances of particles in the swarm using Euclidian metric

$$d_i = \frac{1}{N-1} \sum_{\substack{j=1 \\ j \neq i}}^{N} \sqrt{\sum_{k=1}^{D} \left(x_i^k - x_j^k \right)^2} \qquad \textbf{(2.66)}$$

where D and N are the number of dimensions in the parameter space and the number of particles in the swarm, respectively. The evolutionary factor, on the other hand, is determined by using

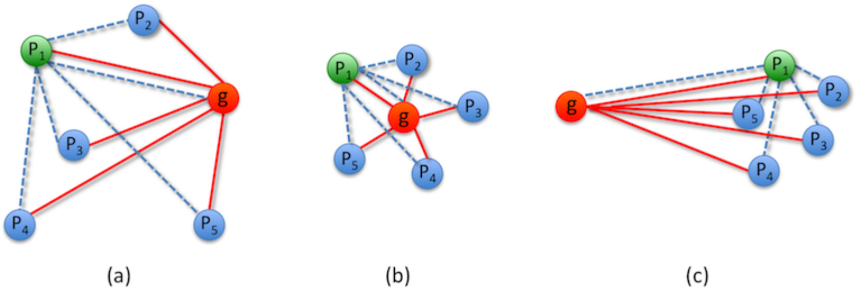

Figure 2.3: The compared distances for g and P_1 particles to the others in (a) exploration, (b) exploitation, convergence, and (c) jump-out states, where g is the globally the best particle in the swarm with $P_1, P_2, \ldots, P_5$ [45].

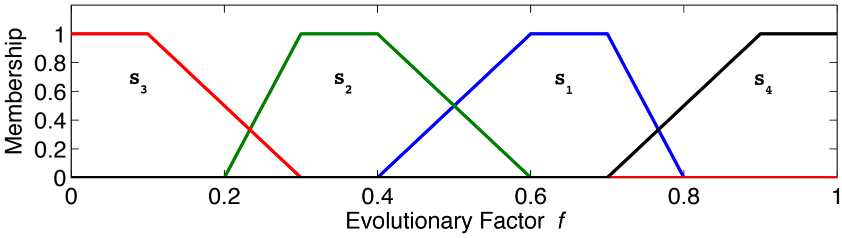

Figure 2.4: S_1 exploration, S_2 exploitation, S_3 convergence and S_4 jump-out state membership for evolutionary factor [45].

$$f = \frac{d_g - d_{min}}{d_{max} - d_{min}} \tag{2.67}$$

where d_g is the average distance of all particles to the best particle, d_{min} and d_{max} are the minimum and the maximum distances of particles to each particle in the swarm (See Fig. 2.3).

The membership of the swarm is initialed with S_1, (*exploration*) state, evolved with the sequence $S_1 \rightarrow S_2 \rightarrow S_3 \rightarrow S_4 \rightarrow S_1 \rightarrow \ldots$, and determined by fuzzy classification of evolutionary factor f. The membership for each f value is classified in the fuzzy logic scheme (See Fig. 2.4). The membership is determined by "singleton" method that chooses the function with the highest value for f factor. For example, if a swarm is in S_1 state and the calculated f is 0.45, then the following state will be S_2. However, in case where the swarm is in S_4 state then with the same factor the state will change to S_1 in the fuzzy logic scheme. With the determination of the states, APSO modifies c_1 and c_2 values adaptively using ESE procedure in states shown in Fig. 2.5. In *exploration* state, since the initial swarm is not settled near the best value of the parameter space and each particle is not well fitted yet, the self learning rate c_1 is increased and social learning rate c_2 is decreased to provide a search for the nearby

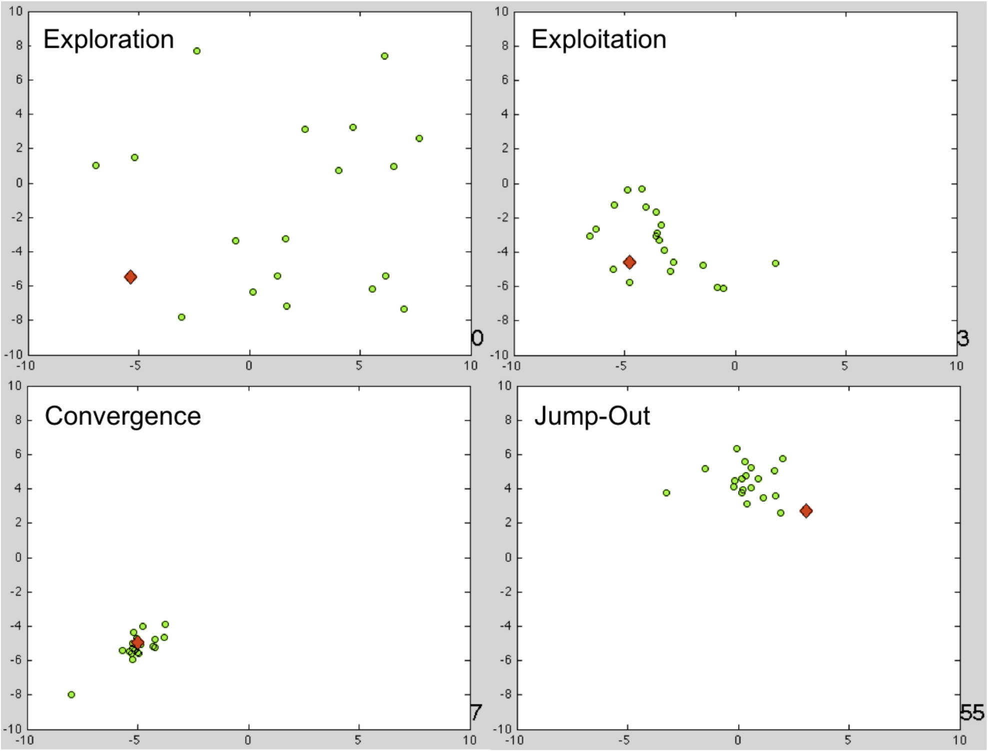

Figure 2.5: The swarm distribution in various evolutionary states of an optimization for two dimensional problem. (a)Exploration, (b)Exploitation, (c)Convergence, (d)Jump-out.

minimum. In *exploitation* state, the evolutionary factor is the indicator of how much the swarm tends to move towards a minimum determined by the best particle in the swarm. To provide a better search procedure, c_1 is increased and c_2 is decreased slightly. Such a change in the rates will provide a slow search towards the minimum so far. In the case of *convergence* state, both c_1 and c_2 rates are increased slightly. The increase in the social learning rate will first supply a positive bias towards the best fitted particle but increasing the values further will do an opposite action on the c_1 and c_2 parameters; the values of c_1 and c_2 will be decreased. The *convergence* procedure includes an additional searching algorithm called elitist learning stage (ELS). In ELS, one of the dimension P^d of the best particle *gBest* in the swarm is randomly selected and perturbed using a Gaussian function by

$$P^d = P^d + \left(X^d_{max} - X^d_{min}\right) \cdot Gaussian(\mu, \sigma) \tag{2.68}$$

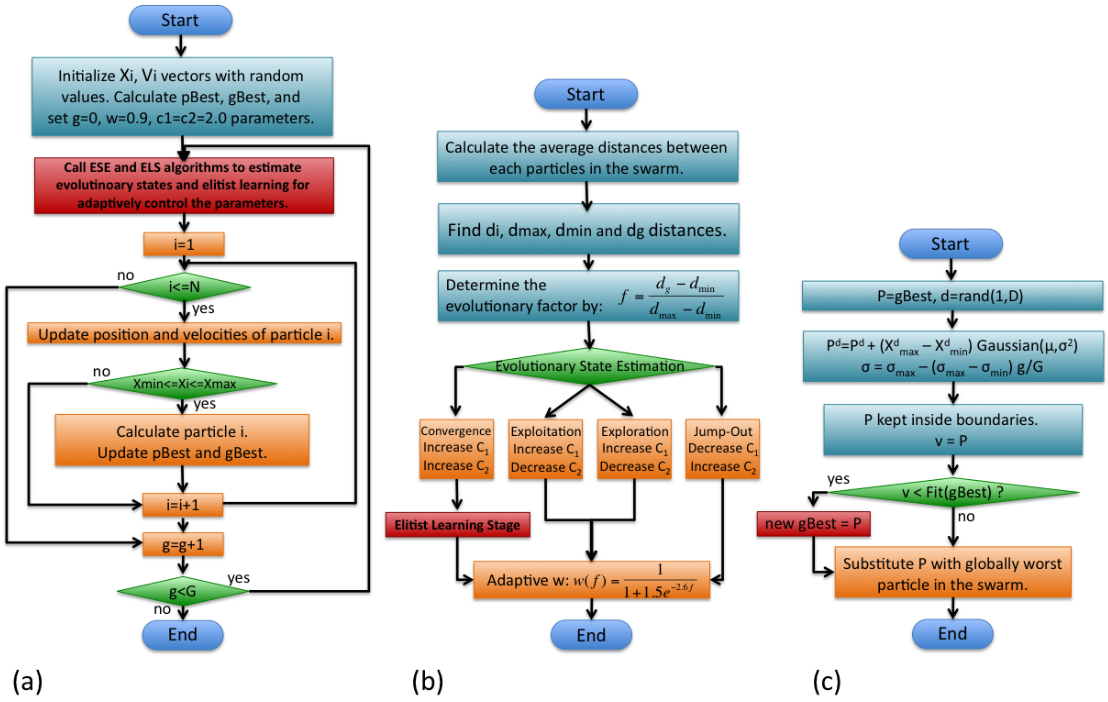
Start
Initialize Xi, Vi vectors with random values. Calculate pBest, gBest, and set g=0, w=0.9, c1=c2=2.0 parameters.
Call ESE and ELS algorithms to estimate evolutionary states and elitist learning for adaptively control the parameters.
i=1
i<=N
no
yes
Update position and velocities of particle i.
Xmin<=Xi<=Xmax
no
yes
Calculate particle i. Update pBest and gBest.
i=i+1
g=g+1
g<G
yes
no
End
(a)
Start
Calculate the average distances between each particles in the swarm.
Find di, dmax, dmin and dg distances.
Determine the evolutionary factor by: $f = \frac{d_g - d_{min}}{d_{max} - d_{min}}$
Evolutionary State Estimation
Convergence Increase C_1 Increase C_2
Exploitation Increase C_1 Decrease C_2
Exploration Increase C_1 Decrease C_2
Jump-Out Decrease C_1 Increase C_2
Elitist Learning Stage
Adaptive w: $w(f) = \frac{1}{1+1.5e^{-2.6f}}$
End
(b)
Start
P=gBest, d=rand(1,D)
$P^d = P^d + (X^d_{max} - X^d_{min})$ Gaussian(μ,σ^2)
$\sigma = \sigma_{max} - (\sigma_{max} - \sigma_{min})$ g/G
P kept inside boundaries. v = P
v < Fit(gBest) ?
yes
no
new gBest = P
Substitute P with globally worst particle in the swarm.
End
(c)

Figure 2.6: The flow chart of (a) main APSO algorithm, (b) Evolutionary state estimation, (c) Elitist learning [45].

where X^d_{max} and X^d_{min} are the search boundaries $[X^d_{min}, X^d_{max}]$ of d dimension and the Gaussian distribution with a $\mu = 0$ mean and with an adaptive standard deviation σ given by

$$\sigma = \sigma_{max} - (\sigma_{max} - \sigma_{min})\frac{g}{G}. \tag{2.69}$$

In Eqn. 2.69, $\sigma_{min} = 0.1$ and $\sigma_{max} = 1.0$ with g and G are the generation step and the total number of generations, respectively. ELS is applied in *convergence* state until a better fitting position is achieved, where *gBest* particle value is substituted with the best value found by the procedure. In such a case, the swarm will produce a higher evolutionary factor for which the algorithm tends to switch to *jump-out* state. In *jump-out* , c_2 is increased and c_1 is decreased so that the swarm follows the new best fitted particle and escape from the local minimum. With the relatively high social bias, each particle forgets their previous best fits and the *exploration* state is initialized again. In the optimization procedure, the above evolutionary state cycle is carried out until the total generation number is reached.

In all generation steps of the APSO algorithm, the following constrains are implemented: c_1 and c_2 values are kept in range of $[1.5 - 2.5]$ and the sum of c_1 and c_2 values are enforced to stay within the range $[3.0 - 4.0]$ by using

$$c_i = \frac{4.0c_i}{c_1 + c_2}, \qquad i = 1,2. \tag{2.70}$$

On the other hand, c_1 and c_2 values are increased or decreased with the following rule

$$|c_i(g+1) - c_i(g)| \leq \delta, \qquad i = 1,2 \tag{2.71}$$

where δ is a random acceleration rate in the range of $[0.05, 0.1]$. In *exploitation* and *convergence* states c_1 and c_2 are slightly increased/decreased by 0.5δ values. The overall flow chart for the APSO algorithm is presented in Fig. 2.6.

3. CALCULATIONS ON Cu NANOWIRES

In this Thesis, the preliminary total energy and structure calculations were performed on several Cu nanowires using the existing EAM potential before developing our own many-body type model potential for Cu-Ni alloys and then performing total energy and MD calculations on these binary alloy systems.

3.1 Atomic Relaxations on Cu Nanowires

For structures with a high surface-to-volume ratio like nanowires the key question concerning the equilibrium configuration of the crystal is closely related to the rearrangement of electronic and ionic structure induced by loss of symmetry. For nanowires, this effect is expected to be dramatic in radial direction and thus different characteristics in individual atomic relaxations are more likely. In a related study, Ma and Xu investigated the atomic relaxations on Cu nanowires with <100> axial orientation and defined the multilayer relaxations on these systems [46,47]. However, the local atomic environments for atoms at both surface skin and cross-sectional area of a nanowire are rather different. This effect is even more pronounced on the nanowire with smaller cross-sectional area. Hence, during the energy minimization procedure each atom is expected to relax accordingly, thus to show varying characteristics. The question then arises regarding whether one can really define multilayer relaxations for nanowires. Thus, the goal in this part of the Thesis is to explore any size effect on atomic relaxations and the energetics of Cu nanowires. For that a comparative investigation on Cu nanowires with the axial direction of <100> and <110> were carried out.

3.2 Computational Details

The model systems for examining the size effect on atomistic processes and relaxations, the <100> and <110> axially oriented copper nanowires are constructed

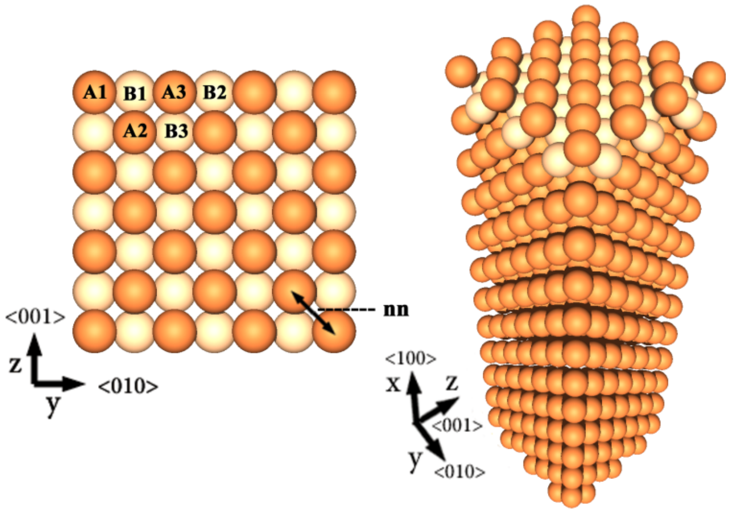

Figure 3.1: Cross-sectional (on the left) and perspective view (on the right) of the <100> axially oriented nanowire with 7×7 number of atoms along the diagonals. The darker and lighter yellow spheres show the atoms in A and B type stacking of Cu(100) crystal. For the N(100)×(100) type nanowires, the distance between the atoms along the diagonal is nn (nearest neighbor distance).

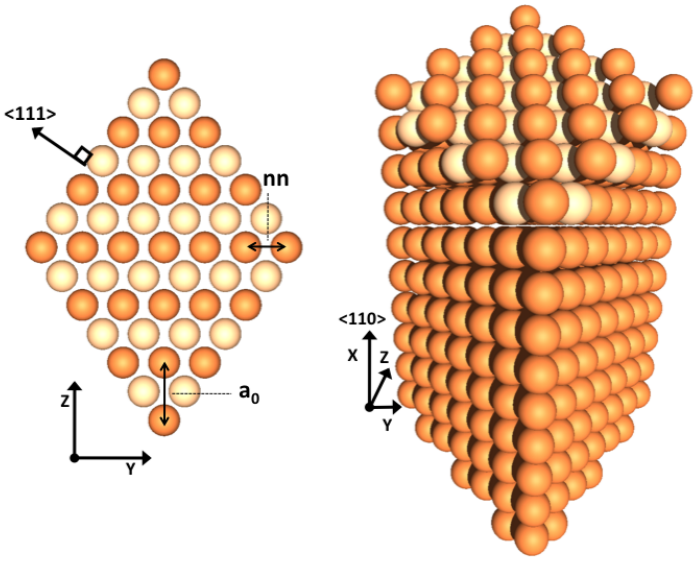

Figure 3.2: Cross-sectional (on the left) and perspective view (on the right) of the <110> axially oriented nanowire with 7×7 number of atoms along the diagonals. The darker and lighter yellow spheres show the atoms in A and B type stacking of Cu(110) crystal. For the N(110)×(111) type nanowires, the distances between the atoms along the short and long diagonals are *nn* (nearest neighbor distance) and a_0 lattice constant, respectively.

by top-down process, which involves extraction of the nanowire from a slab with the associated surface orientation. The nanowires with a <100> surface skin orientations are fabricated by cutting the (100) slab through the (100) walls of a square. A similar procedure is conducted for <110> axial oriented nanowires by cutting the (110) oriented slab through the (111) walls of a diamond. Here, a compact notation is introduced to easily visualize the structure of both rectangular and diamond nanowires with the same four surface skin orientations and the same number of atoms along both diagonals of the cross-sectional area. This notation is similar to that proposed by Lang *et al* for visualizing the stepped surfaces [48]. In this notation the nanowire structure is given by in general form of $N(h_a k_a l_a) \times (h_s k_s l_s)$, where $(h_a k_a l_a)$ and $(h_s k_s l_s)$ are the Miller indices for the cross-sectional plane (or for the axial direction) and surface skin orientations, respectively and N represents the number of atoms along the diagonals, $n \times n$, of the cross-sectional area of the nanowire. Here, the investigated nanowires are ranging from 3×3 to 19×19 number of atoms along the diagonals of the cross-sectional plane.

In this Thesis, the y and z axes are taken to lie in the cross-sectional plane and x being along the axial direction of the nanowire, as shown in figure 3.1 and 3.2. For atomic relaxation calculations, the atoms at the cross-sectional plane of the wire are labeled A1, A2, A3 and B1, B2, B3, representing the atoms, with different coordination numbers, of A and B type stacking of Cu(100) and Cu(110) crystal. Each supercell representing the nanowire with <100> and <111> surface skin orientations contains 24 layers of atoms along the axial direction. The cross-sectional plane dimensions of N_y and N_z are the number of atoms along the y and z directions and defined by the number of atoms along the diagonals, N. Periodic boundary condition is applied along the x-direction to simulate an infinitely long nanowire, while no such constraint is imposed along the y and z directions. In this work, the interactions between the atoms are describe within the system using many-body type model potentials obtained from the embedded atom method (EAM) [8,49] that are already tested and proven to be reliable for examining the energetics, structure and dynamics of low-coordinated surfaces and nano-structured materials [50–55]. Once the model systems are constructed in their bulk terminated geometries, the standard conjugate gradient [56] method is used to minimize the total energy of the system and thus to relax the atoms in their 0K equilibrium configuration, and to determine the atomic relaxations and the total energy for the final stable state.

3.3 Results & Discussions

The influence of varying cross-sectional area of $N(100) \times (100)$ type nanowire on atomic relaxations are examined by investigating the structural relaxations of the same type of nanowires with the cross-sectional area ranging from 5×5 to 15×15 number of atoms along the diagonals. The individual relaxations of each atom at the cross-sectional plane of 5×5 and 15×15 are shown in figure 3.3. Relaxation of each atom of nanowires shows similar characteristics to those of the surface atoms on vicinal surfaces [51,57,58]: the atom with the lowest coordination number relaxes the most. As seen in figure 3.3, the atom A1 is the least-coordinated atom (5) and relaxes towards the remainder of the wire the most so that it increases its effective coordination number. Note that atoms in the cross-sectional plane have different local atomic environment; the coordination number for atoms A1, A2, A3, B1, B2, and B3 are 5, 12, 8, 8, 8, and 12, respectively. As a consequence of varying coordinations, the force fields in the region of these atoms are expected to be nonuniform and thus resulting in relaxation patterns that are not uniform in both magnitude and direction. For example, the relative displacements of the atoms A1, A2, and B1 on 5×5 type nanowire - from their bulk terminated positions - are 0.22, 0.07, and 0.06, respectively, and are oriented in various directions whereas on 15×15 the corresponding displacements are 0.02 , 0.005 (almost zero), and 0.006 (almost zero) (see figure 3.3), indicating that the effect of the lower coordination on atomic relaxations diminishes as the cross-sectional area increases.

In a related computational study, Ma and Xu have investigated the multilayer relaxations on the same type of copper, silver, iridium, and nickel nanowires and found an increase in the outmost interlayer relaxation of copper nanowires as the cross-sectional area decreases [46, 47]. They conduct the calculations using the interatomic potentials obtained from the modified embedded atom method (MEAM). These potentials are empirical extensions of the original EAM potentials that include the angular bonding through the angular dependence of atomic electron density. For

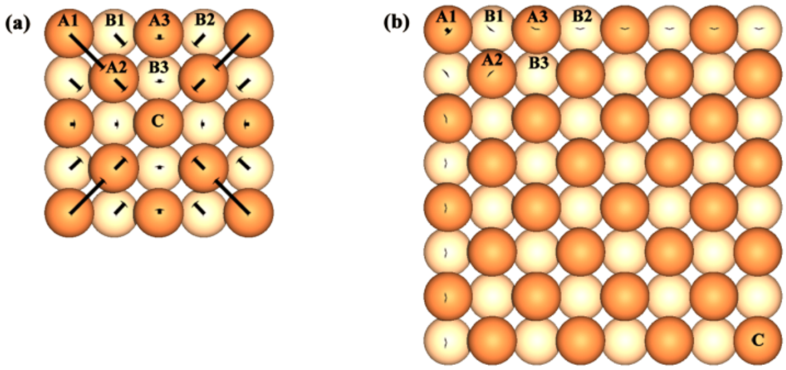

Figure 3.3: The atomic relaxations, with respect to bulk terminated positions, at the cross-sectional plane of (a) 5(100)×(100) and (b) 15(100)×(100) type nanowires. (b) shows atomic displacements only on the left corner of the 15×15 nanowire. The displacements are magnified by a factor 4.5 in both (a) and (b). Here C represents the atom at the center of cross-sectional plane. The labeled atoms of A and B represent the atoms of A and B type stacking of Cu(100) crystal. Note that the magnitudes of the relaxations of atoms around the edges of nanowire diminish as the cross-sectional area increases.

Cu, the angular forces are not likely to be as significant as they are in silicon. Hence, both MEAM and EAM potentials are expected to exhibit similar characteristics on the multilayer relaxations of copper systems, albeit of differing in numerical values. In fact, for Cu(100) both potentials predict an inward relaxation for the first interlayer separation and damping characteristic in the interlayer relaxations away from the surface into the bulk [7,8,46,47,59]. Here, however, the question is raised if one can really define the multilayer relaxations for nanowires. The multilayer relaxations for a system with a surface are defined as percentage-wise changes in the distances between the two consecutive layers (towards the bulk) with respect to the corresponding interlayer separations in the bulk and given by

$$d_{i,i+1} = 100\frac{[z_{i,i+1} - d_b]}{d_b}, \tag{3.1}$$

where $z_{i,i+1}$ is the distance between the ith and $(i+1)$th layer in the relaxed structure and d_b is the interlayer separation in the bulk and it is 1.8075 for the Cu(100) planes. When a bulk system is cut along a direction to create a system with a surface of desired orientation, atoms of each layer relax collectively to the new equilibrium positions which minimize the energy of the system. Since each atom of the same layer has the same local atomic environment and the same symmetry along the directions parallel to the surface plane, the whole layer is expected to relax to the new equilibrium position in the normal direction to the surface, unless the surface is reconstructed. However, as already discussed in previous paragraph, the case for nanowires is rather different. When a nanowire is constructed by cutting a slab, the symmetry along the radial direction is broken. That leads to varying local atomic environments and thus to individual relaxation patterns for the atoms of the cross-sectional plane, as shown in figure 3.3. For the rectangular nanowires, one of the rectangular surface skin forms the first layer, the next atomic plane parallel to the first one is the second layer, and so forth. For the first layer atoms of A1, B1, and A3 on the 5×5 type nanowires (see figure 3.3(a)), the vertical relaxations (relaxations in z-direction) are not uniform in magnitude and are found to be 0.15Å 0.04Å and 0.02Å respectively, whereas for 15×15 type nanowires the corresponding relaxations are 0.01Å 0.006Å and 0.003Å indicating that for nanowires with smaller cross-sectional area the finite size effect on atomic relaxations are dramatic and leads to varying inward relaxations of the atoms forming the outmost layer, with a pronounced relaxation of the corner atoms. Thus, defining the z-position of the first layer (z_1) of the nanowires (in particular with smaller cross-sectional area) in the relaxed system as defined for infinitely extending flat surfaces, in which case the relaxation of all surface atoms are expected to be the same both in magnitude and direction, is not conceivable. However, for relaxed nanowires one may define an average z-position of the outmost layer. In that case, the z-position of the top layer of the nanowires with smaller cross-sectional area would be dictated mostly by the corner atoms and that might cause the reported increase in the inward relaxation for $d_{1,2}$.

The stability of the wires is yet another crucial aspect when dealing with axially deformed nanowires. To explore the structural stabilies of the wires total energy calculations were employed for both <100> and <110> axial oriented nanowires under the axial strain. Deformation were imposed through a linearly varying displacement profile between the layers along the axial direction. In each increment, the separation between the consecutive layers in the wires is increased or decreased by %1. The

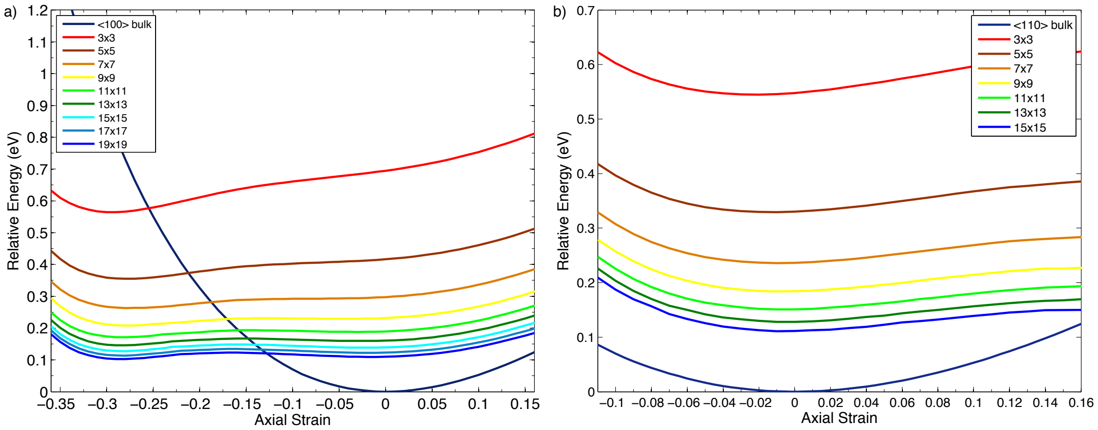

Figure 3.4: The relative energy profiles of various elongation steps for (a) <100> and (b) <110> oriented nanowires with respect to bulk cohesive energy. The bulk energy profile is shown for comparison.

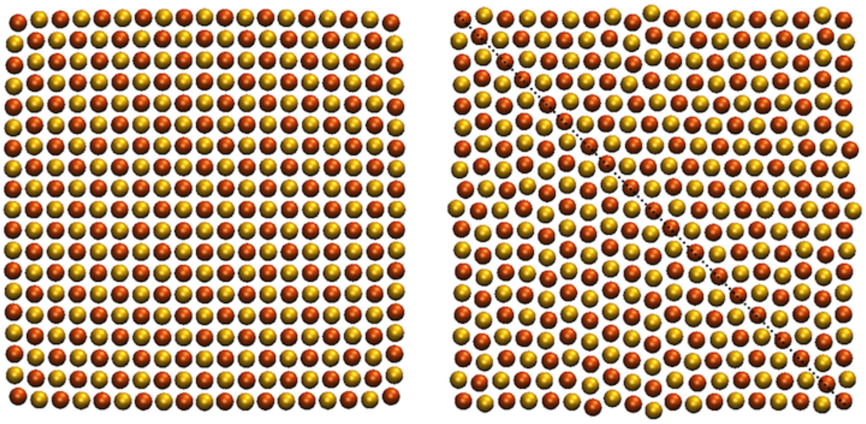

(a) **(b)**

Figure 3.5: The cross-sectional area of <100> nanowire under (a) %36 and (b) %37 contraction.

average energy per atom in the bulk is subtracted from that per atom in each nanowire and the regarding differences were plotted in Fig. 3.4. The defect formation and reconstruction in a structure under the deformations generally lead to unstable configurations, that are easily identified with a sharp change in the total energies. Such a change in the energy for the wires were found below -0.37 strain values. For 13×13 and 19×19 nanowires, high compressive strain is further found to lead to dislocations in the wires (See Fig. 3.5). There is also a minimum energy state for the wires of <100> axial orientation with smaller cross-sectional area at about %30 contraction (See Fig. 3.4a). Interestingly, for the wires with <110> axial orientation, the energy profile does not lead to such a metastable phase (See Fig. 3.4b).

In short, the energetics and atomic relaxations on the <100> and <110> axially oriented copper nanowires are examined and the effect of varying cross-sectional area and varying layer distance along axial direction are considered. From an investigation of atomic relaxations on <100> rectangular nanowires, it is found that each atom at the cross-sectional plane shows varying relaxation patterns and thus find it rather problematic to define multilayer relaxations on nanowires especially with smaller cross-sectional area. Since local relaxations very often manifest themselves in novel characteristics like modifications in local force fields and localized modes [50], an investigation of local vibrational properties of specific atoms, like corner atoms, on these nanowires would be very interesting to see the influence of broken symmetry on the local phonon spectra. On the other hand, investigation of the stability of the nanowires under axial deformation results in existence of a metastable state for the wires with <100> axial orientation and smaller cross-sectional area with respect to the 11×11 whereas no such a state is observed for the <110> axial oriented nanowires.

4. CHARGE CORRECTED EAM POTENTIAL FOR Cu-Ni ALLOYS

The development of highly optimized semi-empirical potentials for bulk Cu-Ni alloys based on the embedded atom method [7,8] is the main focus of this Thesis. Although there has been several Cu-Ni alloy EAM potentials, they are mostly generated through an optimization procedure based on a fitting to the properties of pure elements of the alloy rather than to the properties of the alloy itself. In the formalism of the very first EAM potentials− developed for 6 *fcc* metals of Ag, Cu, Ni, Au, Pt, Pd and their alloys [8], for example, the Cu-Ni alloy potentials are generated through a global fitting process that optimizes the alloy properties not only for Cu-Ni alloy but also for alloys of Cu and Ni with the other four elements. Since the procedure is based on a simultaneous optimization of the potentials for six metals and their alloys instead of optimization of the binary alloy alone, the potentials may have some issues in reproducing the experimental results.

In another study Foiles [9] also developed an alloy Cu-Ni potential where the formalism included only Cu, Ni pure element and Cu-Ni alloy properties. Although the potential successfully reproduces some surface alloy properties such as segregation and surface energies and also some bulk properties like mixing enthalpy and short-range ordering, there is still a need for betterment to correctly describe the phonon dispersions for metals with unfilled d-bands [12].

Zhou *et al.* [13] have also reported an alloy potential database using elemental potentials, including Cu and Ni. In their formalism, an analytical expression [14] is used in developing pair interaction for alloys that include, only the element functions with no parametrization and fitting to alloy properties. Such an approach might be quiet reasonable in developing a general purpose alloy potential which may naturally pose some challenges to correct observations of alloy properties.

The goal in this Thesis is, thus, to develop an accurate and highly optimized Cu-Ni alloy potential which produces reliable predictions for structural properties, energetics, phonons of the alloy.

4.1 The Theoretical and Computational Details of Cu-Ni EAM Potential

4.1.1 Parametrization of alloy potential

In this Thesis, the parametrization of the pair potential, charge density and embedding functions of the EAM potential are carried out by following the scheme presented in Ref. [60]. The charge distribution, on the other hand, is defined using an optimized charge for both $3d$ and $4s$ bands extracted from the Slater-type orbitals with effective nuclear charge approximation. The radial probability distribution of electrons in Slater-type orbitals [61] are given with hydrogen-like wave functions in polar coordinates r by

$$R(r) = r^{n^*-1} e^{-(r(Z^*)/n^*)} \tag{4.1}$$

where n^* is the effective quantum number in the field of effective nuclear charge Z^*, the effective charge $Z - s$ of the actual charge Z screened by s charge. Clementi *et al.* [62,63] derived the screening constants for each orbital from *ab initio* calculations, using the Slater-type orbital approximation. The radial probability of a single electron in $3d$ and $4s$ orbitals for Cu and Ni, resulting from the optimized effective charges, are presented in Fig. 4.1a. As clearly seen in the figure, contrary to the $3d$ bands, $4s$ bands are relatively far from the ion. The total charge densities of $3d$ and $4s$ orbitals obtained from Self Consistent Field (SCF) calculations [63] are also plotted in Fig. 4.1b. Here, the optimized linear orbital charge distributions of Cu and Ni are presented for the electronic configurations, $3d^{10}4s^1$ and $3d^8 4s^2$, respectively. The main difference in the charge densities for Cu and Ni is that, $4s$ band density is slightly higher for Ni atom compared to Cu atom. However, no such major difference can be noticed in $3d$ bands.

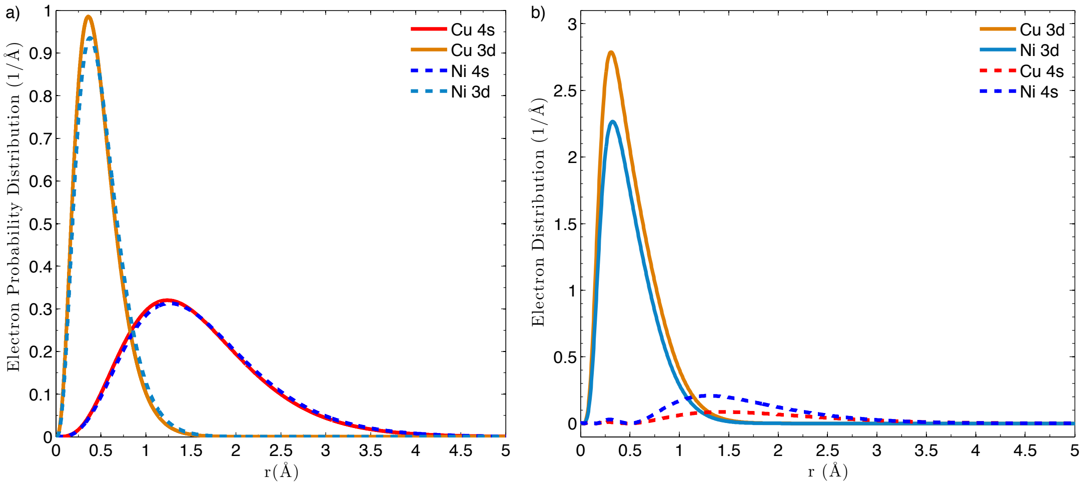

Figure 4.1: The electron charge distributions for Cu and Ni. (a) The probability distributions for $3d$ and $4s$ Slater-type orbitals for effective nuclear charges, (b) The total charge distribution for $3d$ and $4s$ from SCF calculations of Clementi et al. [62,63]

Within the current EAM formalism, the charge distribution, ρ_{Z_j}, is modified so that similar effects in radial distribution of the electron densities for Cu and Ni can be represented. It is taken to be spherically symmetric as in the former EAM formalisms and has the following form:

$$\begin{aligned}\rho_{Z_j}(r) =& tanh(20r^2)\{r^6\left(e^{-\beta r}+2^9 e^{-2\beta r}\right)+\frac{\sigma^{(1)}}{\mu^{(1)}R_B}e^{-\frac{1}{2}\left[\mu^{(1)}(r-R_B)\right]^2} \\ &-0.1\sigma^{(1)}C_{Z_j}e^{-\frac{1}{2}\left[\mu^{(1)}(r-(R_B+0.5))\right]^2}+\sigma^{(2)}e^{-\frac{1}{2}\mu^{(2)}(r-R_A)^2}\}.\end{aligned} \tag{4.2}$$

In the present EAM formalism, the contributions from both $3d$ and $4s$ orbital of effective nuclear charge [61] (See Fig. 4.1a) represented by gaussians in the additional 3 terms that provide a more pronounced $4s$ orbital. If there is no any additional charge in the range of $4s$ band for the metal under investigation, the optimization will cancel out the first two gaussians and the last gaussian function will be shifted in the main part of the charge. Such $4s$ contribution were usually neglected in previous implementations of EAM by using two common approaches: 1) a general charge is described for all elements [7], 2) a spline is defined without a physical background [28].

In the optimizations, the parameters $\sigma^{(2)}$, $\mu^{(2)}$, and R_A in Eqn. 4.2 were taken to be fixed and C_{Z_j} were chosen to be

$$\begin{aligned} C_{Cu} =& 1.0 \\ C_{Ni} =& \frac{1.0}{\mu^{(1)(R_B+0.5)}}, \end{aligned} \tag{4.3}$$

whereas β, $\sigma^{(1)}$, $\mu^{(1)}$, R_B were fitting parameters. Tangent hyperbolic functions were utilized to preserve the $3d$ orbital shape in $r = [0-1]$ range. The pair interaction, on the other hand, were taken to be Morse type potential

$$\phi(r) = D_M \left[1 - e^{\alpha_M (r-R_M)}\right]^2 - D_M. \tag{4.4}$$

Here D_M, α_M, and R_M were the fitting parameters. Morse type pair potentials were proven to characterise the long-range interactions for both Cu [27], Ni [60] pure element and also for Ni-Al alloy [29] very well. On the other hand, the embedding energy function $F(\bar{\rho})$ is defined through cubic splines and directly calculated with the EOS (See Section 2.3).

4.1.2 *Ab-initio* calculations

In this Thesis, for the first-principles calculations, the structure and total energies of the systems were calculated in the plane-wave basis approach in generalized gradient approximation (GGA) within the Kohn-Sham formalism of the density functional theory (DFT) [10] using Quantum Espresso [64] package program. For a further detailed description of DFT method see Section 2.2. Perdew-Burke-Ernzerhof (PBE) parametrization [23] of spin density approximation was specified in electron exchange and correlation. Vanderbilt ultrasoft pseudopotentials [65] were chosen to represent core electron states of atoms in the system. The potentials were developed by Dal Corso et al. [66] with the scalar relativistic calculations including nonlinear core corrections and supplied with Quantum Espresso package. Spin-polarization effects was only considered for Ni and Cu-Ni alloy structures. For pure Cu systems, spin-restrict calculations were carried out. The spin-polarization was contributed by choosing an initial magnetic moment on Ni ions and let the system converge in self-consistent calculations. Series of calculations were exercised to obtain a cutoff energy and proper selection of k-points in the geometry optimizations for total energy conversions. The cutoff energy was determined as E_{cut}=50Ry and *k*-points were selected using $12\times12\times12$ Monkhorst and Pack [67] grid.

In DFT calculations, regardless of the technique used in the exchange and correlation function, the local density approximation(LDA) or the generalized gradient approximation(GGA), both the calculated energies and lattice constants for the desired structures are generally underestimated or overestimated [66]. Furthermore, since DFT does not involve any direct-fitting to produce the desired experimental values as in the case of model interatomic potentials, the results generally deviate from the experimental values. A well-adapted technique [6,28], that provides an avenue for a meaningful comparison between the experimental results and DFT calculations, is to shift the equilibrium structure energies ($\tilde{E}$), calculated with the *ab-initio* method, to a reference E_0 energy, where E_0 is the energy of the equilibrium structure for the element measured from the experiments [6,28]. Here in this study, the reference energy for the elemental potentials was chosen to be the cohesive energy of the pure Cu and Ni atom in *fcc* structures. Therefore, the energies from the *ab-initio* calculations are compared by

$$E(a_0) \sim E_0 - \tilde{E}_0 + \tilde{E}(\tilde{a}_0) \tag{4.5}$$

where, a_0 and $\tilde{a}_0$ are the lattice constants for the equilibrium structure measured from the experiment and calculated with *ab-initio* method, respectively. Since the lattice constants calculated with *ab-initio* can also deviate from the experimental results, a more accurate comparison should be qualified by scaling the lattice constant $\tilde{a}_0$ of the structure calculated with DFT method to the reference value from the experiment [28]. To accomplish this, a scaling factor γ is introduced with the respective ratio of $\tilde{a}_0/a_0$ for each reference structure and the comparison is furnished by

$$E(a_0) \sim E_0 - \tilde{E}_0 + \tilde{E}(\gamma a_0). \tag{4.6}$$

We also adopted the same approach for the alloy energies and extended it to yield the following form:

Table 4.1: Experimental lattice constants for Cu-Ni alloys and unit cell dimensions for the representative crystal structures for *ab-initio* calculations. The experimental values for each desired concentration were the interpolated values of the experimental concentrations taken from Ref. [68], [69].

Alloy	Exp. a_0	Rep. Crystal	a	b	c
$Cu_{75}Ni_{25}$	3.587	$L1_2$	3.6302	3.6302	3.6302
$Cu_{75}Ni_{25}$	3.587	$L1_3$	3.6469	3.6469	3.5896
$Cu_{50}Ni_{50}$	3.566	$L1_0$	3.5594	3.5594	3.6483
$Cu_{50}Ni_{50}$	3.566	$L1_1$	3.5848	3.5848	3.5848
$Cu_{25}Ni_{75}$	3.545	$L1_2$	3.5510	3.5510	3.5510
$Cu_{25}Ni_{75}$	3.545	$L1_3$	3.5292	3.5292	3.5935

$$E_{Cu-Ni}(a) \sim \tilde{E}_{Cu-Ni}(\gamma_n a) - (1-n)\left[E_{Cu} - \tilde{E}_{Cu}\right] - n\left[E_{Ni} - \tilde{E}_{Ni}\right] \tag{4.7}$$

where E_{Cu} and E_{Ni} are the experimental cohesive energies for Cu and Ni respectively and γ_n is determined by the experimental lattice constants given in Table 4.1 for each alloy with a specific Ni concentration of n. The experimental lattice constants for 25%, 50% and 75% Ni alloys were determined by taking a linear interpolation to the available 3.578 Å, 3.564 Å, and 3.529 Å lattice constant results for 37%, 51.5% and 93.5% Ni concentrations, respectively [68].

Following the above scheme, *ab-initio* calculations for the reference structure, *fcc*, of pure Cu and Ni elements were carried out. The predicted equilibrium lattice constant of 3.521Å for Ni is in excellent agreement with experimental value of 3.52Å whereas the calculated lattice constant of 3.677Å for Cu deviates from the experimental value of 3.615Å by %1.73Å . However, the results for cohesive energies exhibit different trends: an overestimate of %7 for Ni and an underestimate of %1 for Cu (the respective calculated and experimental values are 4.83 eV and 4.45 eV for Ni and 3.50 eV and 3.54 eV for Cu). For Cu-Ni alloys, determination of the structures were rather complex, since the experimental measurements indicate that the Cu-Ni alloys have continuous solid-solution *fcc* structure in all concentrations of Ni [70]. For alloys with disordered phase, an approach would be to carry out *ab-initio* calculations and adopt an average ordered crystal structure over randomly chosen ordered crystals [71]. Another approach would be to proceed with an ordered crystal phase as an approximation to the disordered phase, only if the selected phase is a structure close to the average ordered crystal with the lattice constants that do not change in all directions of the unit-cell. One should note that the possibility for each type of atom to settle on an available lattice site in a continuous single phase solid-solution be almost equal in this assumption. Here, the second approach was adopted : extensive *ab-initio* calculations were performed for the ordered *fcc* phases of Cu-Ni alloys. To identify the stable structures of the alloys, three types of Cu concentration was portrayed: 1) 75% Cu and 25% Ni solid-solutions, 2) 50% Cu and 50% Ni solid-mixture, and 3) 25% Cu and 75% Ni random-solution. The crystal structures for the respective compounds were determined through total energy calculations using *ab-initio* technique. Although Cu-Ni is known to have a continuous disordered *fcc* structure, for our purpose of accomplishing predictive power for the structure and the energetics of the alloy, ordered *fcc* phases of $L1_0$, $L1_1$, $L1_2$, and $L1_3$ were utilized to represent local orders in a continuous *fcc* structure. In order to avoid the magnetization effects of Ni at high concentrations [72], no more than 50% Ni were utilized in the process of fitting the model potentials. In *ab-initio* calculations, the unit cells describing the crystals and the symmetries contain typically 32 atoms for the regarded *fcc* crystals and solid-solutions. The lattice constants for each alloy with a different Ni percentage were calculated using $L1_0$, $L1_1$, $L1_2$, and $L1_3$ crystal structures and tabulated in Table 4.1. While the lattice constant for $L1_1$ and $L1_2$ structures are the same in each direction, the unit cell vectors for $L1_0$ and $L1_3$ deviate more than 2%. Since $L1_1$ and $L1_2$ tend to have more stable *fcc* structures and 1% lower minimum energies than $L1_0$ and $L1_3$ in *ab-initio* calculations, the lattice constants and energies for Cu-Ni alloys were taken to be those corresponding to the former crystal structures.

4.2 Optimization and Fitting Procedure of Cu-Ni Potentials

In this study an efficient global searching method, adaptive particle swarm optimization (APSO) [45] (See Section 2.9) was adopted to search the parameter space for EAM potentials. Using our developed parallel version of APSO method, the optimization was carried out with 800 particles each treated as a parameter set that was initialized randomly in the parameter space. In the method, the swarm was avoided to fall in false minimums through an inner random search algorithm "Elitist Learning" based on the fuzzy logic circuits and the jumping-out processes. Developing EAM potentials using optimization methods is rather knotty as the analytical expressions do not always produce accurate derivations of the energies for all parameters that hinders or fails the optimization and results in bogus data. To avoid such a failure, an inner protocol was implemented in the optimization that controls the parameter sets by returning highest error when such numerical error is encountered. This may allow one to span a wide range of parameter space. A modified MPI based parallel version of APSO was also constructed to implement timely efficient algorithm as these optimization techniques usually requires high computational times. The parallelization of the algorithm was constructed not only on the distribution of particles of the swarm to the processes but also on the distribution of increased total number of specialized elitist learning procedures to each process. The details of the implementation of the APSO is given in Section 2.9.

Using the developed parallel APSO code, in the first phase, pure Cu and Ni EAM potential function parameters were fitted by minimizing the weighted mean squared deviations of selected Cu and Ni properties from the experimental values or *ab-initio* calculation results. The fitting of the potential is a nonuniform optimization and the error is defined with a least-squares function D of error between the results of EAM potential and the results of experiment or *ab-initio* calculations. Here, D is defined as

$$D = D_{a_0} + D_{E_c} + D_{\nu_X} + D_{E_D} + D_{R_D} + D_C \tag{4.8}$$

and each term in the sum is given by

$$D_\mu = \omega_\mu \frac{(E_{EAM} - E_{EXP})^2}{E_{EXP}^2} \tag{4.9}$$

where D_μ can be the lattice constant (a_0), cohesive energy (E_c), phonon frequency at the zone boundary (ν_X), diatomic energy (E_D) and bond length (R_D), and elastic constants (C). In the optimization procedure, the errors from the experimental values were weighted with low or heigh ω_μ for a better fitting to the desired properties of the elements and the alloy (See Table 4.3). The minimizations were carried out inside the broadest parameter range of the physical boundaries of the potential functions in all initial runs of the optimization code. Whenever a suitable parameter set was converged within the tolerance of 10^{-10} between each optimization iterations after 1000 steps, the optimization was reinitialized within the narrow boundaries near the minimum parameter set. In general, the second cycle increases the speed of convergence to the minimum parameter set. The optimizations for each Cu and Ni elements and for Cu-Ni alloy were repeated more than 10 times and the parameter sets were selected from the parameter database.

The set of fitted parameters for pure Cu and Ni was presented in Table 4.2. The element properties that were calculated with this parameter sets were tabulated in Table 4.3. In the second phase, the Cu-Ni alloy EAM potential parameters were fitted using the pure elemental functions and alloy potential transformations. The fitted alloy parameters were tabulated in Table 4.2 and the properties of alloy that were calculated and used in fitting were given in Table 4.4.

The fitting database for pure Cu and Ni part includes equilibrium lattice constant, cohesive energy, bulk modulus, elastic constants, the vacancy formation and migration energy for face-centered cubic (*fcc*) structure with the phonon frequencies of *fcc* Brillouin zone-boundary at the point of X in $(00q)$ direction and diatomic bond energy and length. In the second phase, using pure element functions and alloy potential transformations described in Section 2.3, the Cu-Ni alloy EAM potential parameters were fitted. In the fitting database, this time, the equilibrium lattice constants, cohesive energies, bulk modulus and elastic constants of $\mathrm{L1}_1$ and $\mathrm{L1}_2$ Cu-Ni alloy structure were used. In Table 4.2, the fitted alloy parameters were also tabulated and the properties of alloy that were calculated and used in fitting were given in Table 4.4.

4.3 The Results and Discussions for Cu-Ni EAM Potential

The Cu-Ni alloy EAM potential developed in this Thesis involves three fitting functions ($\phi(r)$, $\rho(r)$, and $F(\bar{\rho})$) and two transformations (scaling and shifting) with total of 22 adjustable parameters that were listed in Table4.2. Figure 4.2 shows the resulting functions for the pair interaction, the charge density and the embedding energy. Note that the effective charge density for Ni differs from that for Cu in that it posses a shoulder between the ranges of 1.8Å and 4.4Å from the atom, reflecting importance

Table 4.2: Optimized and fitted parameters for pure Cu, Ni elements and Cu-Ni alloy.

Parameter	Cu	Ni	Cu-Ni
D_M	2.04175	2.21365	1.93942
α_M	2.09230	2.21271	2.22280
R_M	1.30694	1.29030	1.32926
r_{cut}	6.28795	6.39433	6.33084
β	3.46031	3.48630	-
$\sigma^{(1)}$	0.03014	0.23447	-
$\mu^{(1)}$	0.93108	0.90905	-
R_A	2.39580	1.88793	-
S	1.0	0.54043	-
G	-2.30876	0.69228	-
$\sigma^{(2)}$	0.0	0.4	-
$\mu^{(2)}$	-	10.0	-
R_B	-	1.0	-

of the contributions from 4s band valance electrons as mentioned in Section 4.1.1. Let us remind that in EAM formalism, the energy of an ion is determined using the charge densities at its own site due to all host atoms and thus even minute variances in charge densities are expected to show significant impact on the energy of the ion. The curves for pair interactions of pure elements and the alloy show more or less similar characteristics with a single minimum that is shifted for one pair potential to the other. The potentials developed in the thesis have quiet long range with a cutoff radius of 6.288Å, 6.394Å and 6.331Å for Cu, Ni, and Cu-Ni alloy, respectively. The atoms within these cutoff ranges of developed alloy potential have up to the 5th coordination shell and one should note that even small forces coming from atoms in these coordination shells contribute significantly to the elastic constants and phonon dispersion curves.

The reliability and the performance of an alloy interaction potential requires an accurate prediction of the associated experimental and *ab-initio* values for the properties of both pure elements of the alloy and the alloy itself. Therefore, Cu-Ni alloy potential was tested for various properties including energies and constants for several crystal structures, phonon dispersions, mixing energies, melting points, energetics of diffusion mechanisms and structural properties with/without deformation.

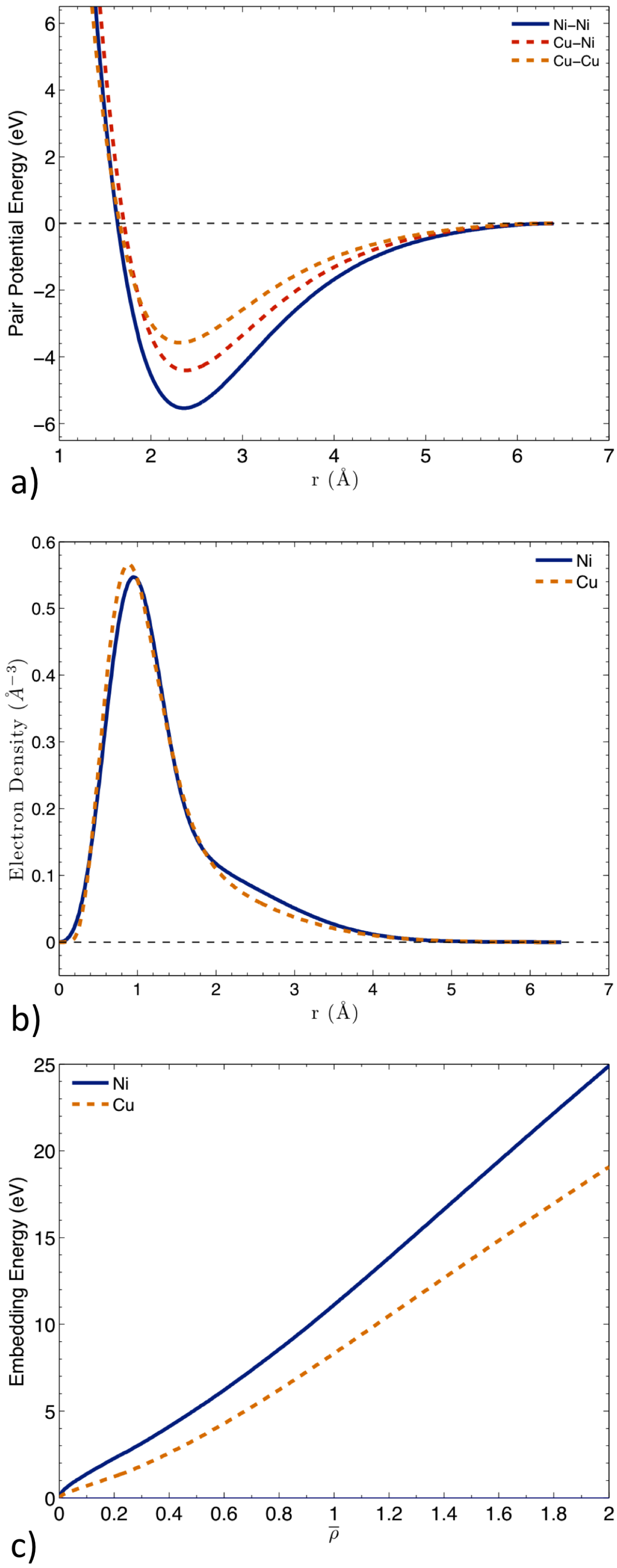

Figure 4.2: Cu-Ni EAM potential functions: (a) pair interaction function, (b) electron charge density function, and (c) embedding energy function.

4.3.1 The structural and total energy calculations

For testing the pure part of Cu-Ni alloy EAM potential, the lattice properties, lattice defects, surface energies, and phonon dispersions for *fcc* crystal structure and the lattice constant and cohesive energies for various crystal structures were investigated using the formalism described in Section 2.4 and 2.5. In Table 4.3, the calculated values of elastic constants, vacancy formation and migration energies, diatomic bond length, diatomic bond energy and phonon frequencies for both Cu and Ni pure element potentials, together with available experimental and calculated *ab-initio* data were presented. Note that, since the lattice constant, cohesive energy and bulk modulus of *fcc* structure were directly used in the optimization procedure within the formalism of EOS, EAM potentials reproduce these properties with a very high consistency (See Table4.3). As seen in the table, the predictive power of the current pure Cu and Ni potential is better compared to the other EAM potentials.

In Table 4.4, the calculated properties for Cu-Ni alloys with several structural formations were presented with the available experimental values and calculated *ab-initio* data. The agreement for vacancy formation energies of Cu and Ni in Cu-Ni alloys and diatomic properties are encouraging for a correct representation of Cu-Ni alloy properties as these properties were not included in the fitting procedure. Surely, correct prediction of elastic constants are crucial for properly describing the material when it is under deformation. Another vital aspect of a deformed system is the lattice defect energies and calculations for structural defect energies such as stacking faults and interstitial sites are critical to further test the potential. The interlayer fault energies of (111) stable and non-stable stacking faults, twining fault were determined using total energy calculations on the supercell shown in Fig. 4.3. The periodic boundary conditions were applied in all directions while no such constraint was imposed in the z- direction. The system with two surface (See Fig. 4.3b) was fully optimized to find the corresponding minimum energy configuration using standard conjugate gradient method.

To calculate the stable (SF) and unstable (US) stacking faults, the atoms at the half of the supercell above a <111> layer were incrementally shifted in a block with respect to the other half of the crystal in <1$\bar{1}$2> direction until the next prefect *fcc* stacking site

Table 4.3: Lattice constants, cohesive energies, bulk modulus, elastic constants, diatomic bond lengths and bond energies, vacancy formation energies and phonons at X, L, and K for Cu and Ni predicted by the current EAM potential, together with the available experimental data and other EAM potentials. † Fitted with low weight. * Fitted with high weight.

	Cu				Ni				
Property	Exper.	Present	M. [27]	FBD [8]	Exper.	Present	M. [28]	VC [28]	FBD [8]
a_0 (Å)	3.615 [73]	3.615	3.615	3.615	3.52 [73]	3.52	3.52	3.52	3.52
E_{coh} (eV)	-3.54 [74]	-3.54	-3.54	-3.54	-4.45 [74]	-4.45	-4.45	-4.45	-4.45
B (10^{11} Pa)	1.383 [75]	1.383	1.383	1.38[a]	1.81 [75]	1.81	1.81	1.81	1.804[a]
C_{11} (10^{11} Pa)*	1.700 [75]	1.701	1.699	1.67	2.47 [75]	2.470	2.47	2.44	2.33
C_{12} (10^{11} Pa)*	1.225 [75]	1.225	1.226	1.24	1.47 [75]	1.480	1.48	1.49	1.54
C_{44} (10^{11} Pa)*	0.758 [75]	0.758	0.762	0.76	1.25 [75]	1.255	1.25	1.26	1.28
E_D (eV)†	-2.02 [76], -2.05 [78]	-2.02	-1.93		-2.068 [77], -2.119 [76]	-2.19		1.94 [60]	
R_D (Å)†	2.2 [77], 2.2195 [78]	2.09	2.18		2.155 [76], 2.20 [77]	2.21		2.23 [60]	
E_v^f (eV)*	1.27 [79], 1.28 [81]	1.281	1.272	1.28[1]	1.60 [80]	1.581	1.60	1.56	1.63
E_v^m (eV)	0.65 [81], 0.71 [81]	0.66	0.689	0.72	1.04 [82], 1.30 [80]	0.83	1.29	0.98	1.08
T_{Melt} (K)	1357 [83]	1278	1325 [84]	1280 [85]	1728 [83]	1646			
$\nu_L(X)$ (THz)*	7.38 [86]	7.38	7.82	7.62[b]	8.55 [87]	8.59	8.71	10.03	9.95
$\nu_T(X)$ (THz)†	5.16 [86]	5.15	5.20	5.07[b]	6.27 [87]	6.24	6.38	6.68	6.76
$\nu_L(L)$ (THz)	7.44 [86]	7.38	7.78	7.56[b]	8.88 [87]	8.84	8.53	10.04	9.84
$\nu_T(L)$ (THz)	3.41 [86]	3.09	3.32	3.17[b]	4.24 [87]	4.05	4.31	4.37	4.32
$\nu_L(K)$ (THz)	5.90 [86]	5.85	6.22	6.10[b]	7.30 [87]	6.86	6.98	8.08	8.00
$\nu_{T_1}(K)$ (THz)	4.60 [86]	4.65	4.65	4.54[b]	5.78 [87]	5.70	5.68	6.04	6.08
$\nu_{T_2}(K)$ (THz)	6.70 [86]	6.76	7.17	7.02[b]	7.93 [87]	7.84	8.04	9.23	9.18

[a] fitted to different experimental values, see Ref. [7].

[b] calculated with the EAM potential in Ref. [8].

Table 4.4: Lattice constants, cohesive energies, bulk modulus, elastic constants, vacancy formation energies and diatomic bond lengths and bond energies for Cu-Ni alloys predicted by the current EAM potential compared with the available experimental and *ab-initio* data. † Fitted with low weight. ∗ Fitted with high weight.

Representative Crystal Structure / Diatomic Formation	Alloy Property	Experiment or *ab-initio*•	Present EAM
CuNi $L1_1$	a_0 (Å)*	3.566 [68]	3.576
	E_{coh} (eV)†	-3.99•	-3.974
	B (10^{11} Pa)*	1.618 [88]	1.615
	C_{11} (10^{11} Pa)*	2.049 [88]	2.079
	C_{12} (10^{11} Pa)*	1.402 [88]	1.383
	C_{44} (10^{11} Pa)*	0.991 [88]	1.031
	E_v^f (Cu) (eV)	1.36•	1.25
	E_v^f (Ni) (eV)	1.61•	1.77
Cu_3Ni $L1_2$	a_0 (Å)*	3.587 [68]	3.609
	E_{coh} (eV)†	-3.694•	-3.749
	B (10^{11} Pa)*	1.467 [88]	1.544
	C_{11} (10^{11} Pa)*	1.869 [88]	1.873
	C_{12} (10^{11} Pa)*	1.311 [88]	1.276
	C_{44} (10^{11} Pa)*	0.878 [88]	0.855
	E_v^f (Cu) (eV)	1.31•	1.30
	E_v^f (Ni) (eV)	1.59•	1.82
CuNi $L1_0$	a_0 (Å)	3.566 [68]	3.591
	E_{coh} (eV)	-3.95•	-3.969
Cu_3Ni $L1_3$	a_0 (Å)	3.587 [68]	3.603
	E_{coh} (eV)	-3.700•	-3.751
Cu-Ni Diatom	E_D (eV)	-2.05 [77]	-1.92
	R_D (Å)	2.23 [89]	2.23

was found. In each increment, the system was fully relaxed in <111> direction and the total energy of the system was calculated. To calculate the energy of the layer fault, the energy difference with respect to the unperturbed configuration was divided to the area of the layer. The energies along the path was presented in the Fig. 4.4 and the stable stacking fault configuration was given in Fig. 4.3c. The stable stacking fault energy is the minimum energy difference at the hexagonal-closed pack stacking site of the shifting. The shifted layers are shown with yellow and red atoms above unperturbed layers represented by orange and blue atoms. The stacking fault layers are the layers of red and blue atoms (See Fig. 4.3c). Similar calculations were also carried out for twining fault energy of (111) stacking. To obtain a twining structure, first the layers above the 8th layer from the bottom were shifted towards <$1\bar{1}2$> and then the layers above the 10th layer shifted back to the correct *fcc* stacking sites that leads to the two twining layers in between the blue and red layers (See Fig. 4.3d). The energy of the twining fault was then calculated by fully relaxing the supercell and taking the energy differences between the fault structure and the relaxed unperturbed *fcc* super cell with (111) surfaces on each side. The surface energies γ_S for all flat surfaces of an *fcc* crystal (100), (110), and (111) were also calculated using total energy optimization. First, the computational slabs with two surfaces were let to relax to their equilibrium configurations. This time the energy minimization was carried out to relax all atoms in all three cartesian directions without any constrain. The surface energies is then obtained by dividing the energy difference, between the bulk structure and the surface slab, by the two surface areas. The surface energies for Cu and Ni solid phases at 925K and 1060K were calculated through constant number of atoms, pressure and temperature (NPT) simulations for 1 nanosecond.

The other structural defects such as the interstitial site defects of (100) dumbbell, tetrahedra and octahedra sites on an *fcc* crystal were studied using a supercell with 20×20×20 atoms (See Fig. 4.4a). Periodic boundary conditions were applied in all cartesian coordinated and cells were relaxed to their minimum energy configurations using conjugate gradient method. In Fig. 4.4b-d, the dumbbell (D_{fcc}), tetrahedra (T_h) and octahedra (O_h) defect structures were presented and varying colors indicate varying cohesive energy of each atom in the crystal. A dumbbell defect is a dimer

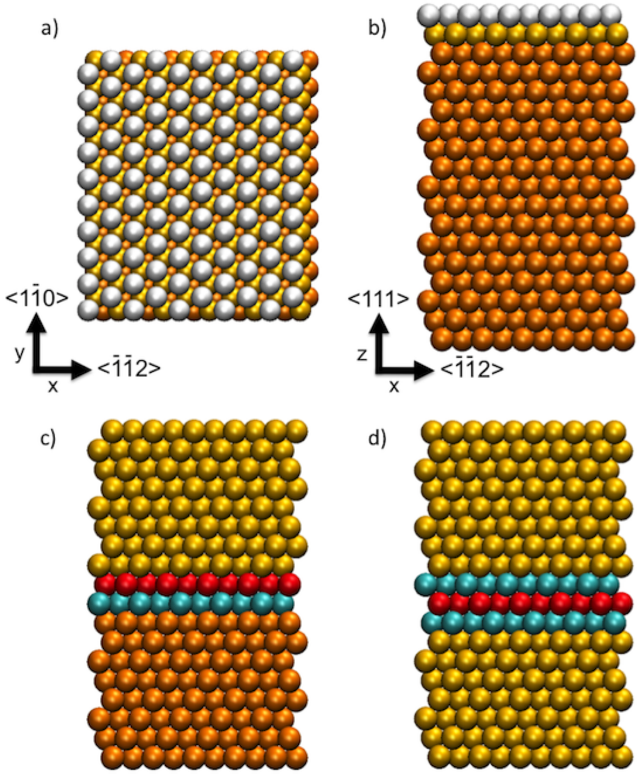
a)
b)
<1$\bar{1}$0>
y
x
<$\bar{1}\bar{1}$2>
<111>
z
x
<$\bar{1}\bar{1}$2>
c)
d)

Figure 4.3: The atomic configurations for (a) the non-defect structure of *fcc* bulk crystal from top view of (111) orientation, (b) side view of the defect free structure, (c) (111) stacking fault structure in between the layers of blue and red atoms, (d) the two (111) twining fault structure in between the layers of blue and red atoms.

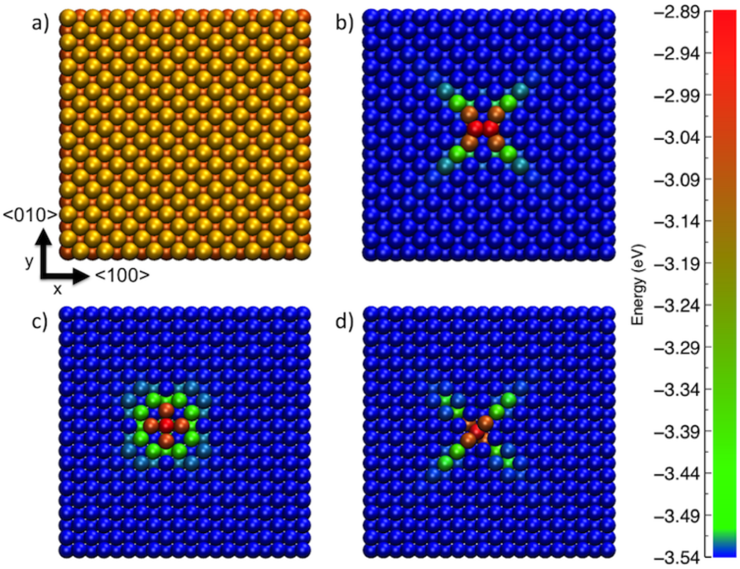

Figure 4.4: The atomic configurations for (a) the defect free structure of *fcc* bulk crystal from top view of (001) orientation, (b) dumbbell (red atoms) structure, (c) (111) stacking fault structure in between the layers of blue and red atoms, (d) the two (111) twining fault structure in between the layers of blue and red atoms. The colors represent the cohesive energies in between the minimum -3.54eV (blue) and maximum -2.89eV (red).

settled on a lattice site along (100) direction, whereas an octahedra defect is on a 4-fold site in between the neighboring *fcc* unitcells. A tetrahedra defect site is, on the other hand, located in between the nearest neighbor atoms which are the basis of an *fcc* unitcell. As seen from the varying colors in the figures 4.4(b-d) the interstitial defects generally perturbate the lattice crystal up to the third nearest neighbor from the defect atom(s). The formation energies E_f of the defects were calculated using

$$E_f = E_{defect} - [(N+1)/N]E_0, \tag{4.10}$$

where, N and E_0 are the total number of atoms and the total energy of the pure equilibrium crystal, and E_{defect} is the total energy of the same reference structure with the defect atom in the desired position. In Table4.5, the calculated stacking fault and interstitial defect energies were presented together with the experimental/*ab-initio* values and predictions of other EAM potentials. The agreement between predictions of the current Cu-Ni potential and the experimental data are promising. Note also that although the present Cu-Ni EAM potential predicts the stable and non-stable stacking

Table 4.5: Energies (mJ/m^2) for surface formation, planar defects and energies (eV) of interstitials for Cu, Ni elements calculated by the current EAM potentials compared with available experimental data.

	Cu			Ni			
Defect	Experiment or *TB*	Present EAM	M.[27]	Experiment or *ab-initio*	Present EAM	M.[28]	Voter[60]
γ_{SF}	45[90]	45	44.4	125[91]	129	125	58
γ_{US}	162[d]	162	158	269[92]	281	366	225
γ_T	24[91]	23	22.2	43[91]	67	63	30
$\gamma_S(100)$ (Relaxed 0K)	2149[d]	1978	1345		3551	1878	1754
$\gamma_S(110)$ (Relaxed 0K)	2335[d]	2099	1475		3422	2049	1977
$\gamma_S(111)$ (Relaxed 0K)	1889[d]	1860	1239		3311	1629	1621
Average γ_S $(Rel.0K)$	2124[d]	1979	1353		3427	1852	1784
Average γ_S $(925K)$	1790[a]	1513					
Average γ_S $(1060K)$				2280[a]	3316		
$E_I^f(O_h)$(eV)	2.8-4.2[82]	3.123	3.063		4.893	5.86	4.91
$E_I^f(T_h)$(eV)	3.7-3.89[93]	3.374			4.427		
$E_I^f(D_{fcc})$(eV)	2.51[b]	2.962	3.063	4.07[c],4.08[93]	3.746	4.91	4.64

[a] For average orientation, see Ref. [94] and [91].
[b] Tight-Binding (TB) calculation, see Ref. [95].
[c] DFT calculation, see Ref. [96] and [95].
[d] Tight-Binding (TB) calculation, see Ref. [27].

faults, and the twin faults in consistent with available experimental and other EAM potential data, it overestimates the surface energies of the pure elements of Cu and Ni.

In simulations under pressure or strain the equilibrium lattice structure will eventually take a form of non-equilibrium phases such as hexagonal closed pack (*hcp*), body-centered cubic (*bcc*), simple cubic (*sc*), and diamond cubic (*dc*) structures. The developed Cu and Ni pure element potentials and Cu-Ni alloy potential were also tested for the structural constants of several lattices and the results were presented in Table 4.6. The predicted structural constants of both the pure element and the alloy lattice structures are in good agreement with the experimental values and the results of other EAM type potentials.

Additionally, the alloy mixing enthalpies were calculated for both solid phases at 0K and 973K to compare with experimental curves at regarding temperatures. A series of molecular dynamic (MD) simulations were preformed to compute enthalpy of Cu-Ni alloys with various Ni concentration at different temperatures. For each specific Ni

Table 4.6: Energies per atom (mJ/m^2) for several selected crystal structures of Cu, Ni calculated by the current EAM potentials and compared with *ab-initio* data.

	Cu				Ni			
	ab-initio		EAM		*ab-initio*		EAM	
Structure	a_0	E_{coh}	a_0	E_{coh}	a_0	E_{coh}	a_0	E_{coh}
fcc	3.615	-3.540	3.615	-3.540	3.520	-4.450	3.520	-4.450
hcp	2.557[a]	-3.528	2.560[b]	-3.532	2.487[c]	-4.420	2.492[d]	-4.429
bcc	2.873	-3.496	2.899	-3.509	2.800	-4.300	2.780	-4.374
sc	2.395	-2.996	2.373	-3.093	2.334	-3.440	2.333	-3.905
dc	5.348	-2.293	5.289	-2.411	5.095	-2.510	5.221	-3.163

[a] c/a=1.633
[b] c/a=1.640
[c] c/a=1.637
[d] c/a=1.630

concentration, several Cu-Ni alloy super cells were formed by utilizing Cu and Ni atoms randomly in their bulk terminated positions so that an accurate statistics can be carried out. The supercell representing the systems were constructed with about 5000 atoms and was carefully designed to circumvent the size effects in the simulations. For each test, the atoms in the supercell first optimized to their minimum energy configurations and then heated to the desired temperature by using constant number of atoms, pressure and temperature (NPT) ensemble for 500 *ps*. The average enthalpy and total energies for each Ni concentration of n were used in

$$H_{Cu-Ni} = H_{Total}(Cu,Ni) - (1-n)\left[H_{Cu}\right] - n\left[H_{Ni}\right] \tag{4.11}$$

to calculate the alloy mixing enthalpy. The present calculated results for alloy mixing energy are in good agreement with experimental data (See Fig. 4.5). Comparing with the other EAM potentials, the current alloy potential has a better prediction competency in producing the alloy mixing energy. Experimental results generally shows a pick around 60% Ni in mixing Cu-Ni alloy. This slightly shifted mixing enthalpy character towards high Ni concentrations is considered originating from the fulfillment of the 3*d* orbital electron holes of Ni with the extra electron of Cu from 4*s* bands [97].

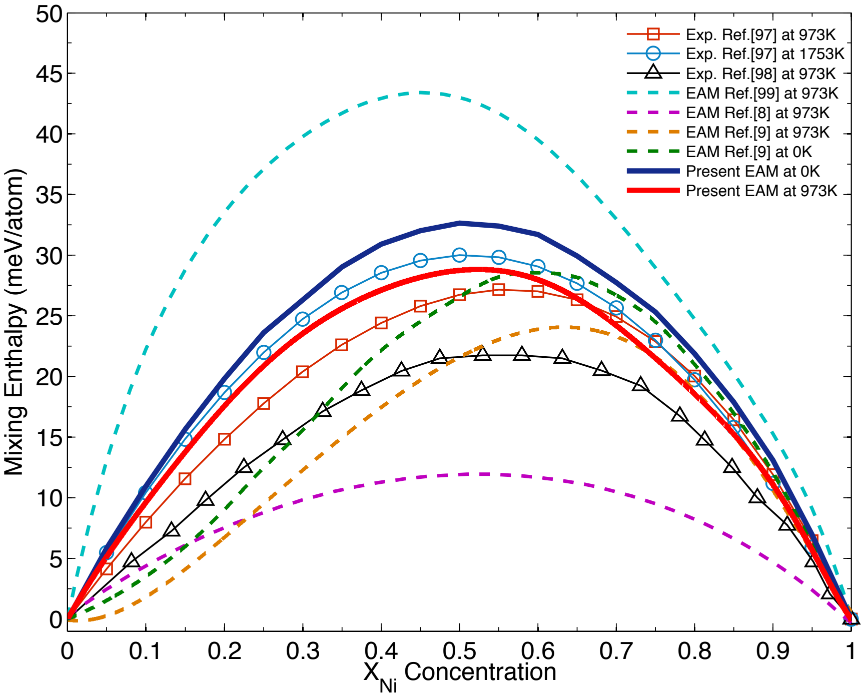

Figure 4.5: Mixing enthalpy for Cu-Ni alloy in various concentrations of Ni calculated with the current EAM potential. The experimental values from Ref. [97], [98] and the values of other EAM type potentials from Ref. [8], [9], and [99] are shown for comparison.

4.3.2 Phonon dispersions for Cu, Ni and Cu-Ni alloys

To further test the developed potentials, phonon dispersion curves for Cu and Ni pure elements and Cu-Ni alloy were also calculated with dynamical matrix approach (See Section 2.5 for details.) using both the developed potential and the *ab-initio* method. The *ab-initio* calculations were carried out by using GGA approximation with $10^{-14} Ry$ tolerance by taking $16 \times 16 \times 16$ **k**-point grid first, and second using $4 \times 4 \times 4$ **q**-point grid to gather the force constants of the dynamical matrix.

As seen in Fig. 4.6 the phonon dispersion curves of *fcc* Cu and Ni crystals, calculated using the fitted EAM potentials, are in very good agreement with both experimental and *ab-inito* results. Note also that only the phonon frequencies at zone-boundary point X were included in the fitting, the frequencies at the other k-points were predicted by the potentials. The present Ni potential slightly underestimates the phonons close to W point for frequencies lower than 6 THz.

Since no experimental data for phonon dispersion curves of any binary Cu-Ni alloy are available, the phonon spectrum was calculated using DFT based *ab-initio* methods for a chosen ordered crystal phase of Cu-Ni alloy. Note that it is not the intend here to determine any crystal phase of Cu-Ni alloy. Thus the force constant matrix was formed corresponding to the chosen compound structure of Cu-Ni alloy instead of forming an average force constant matrix by carrying out several *ab-initio* calculations for various Ni concentrations in Cu-Ni alloys which is the traditional way for determining any existing crystal phase of an alloy [71]. The main objective here is to test the accuracy of the new model Cu-Ni alloy potential by comparing the predicted optical modes for such a model alloy crystal structure with that obtained from DFT calculations.

The present DFT results led to two suitable model representation for Cu-Ni alloys, $L1_1$ and $L1_2$, that were discussed in previous sections. Due to the simplicity of the unit cell, $L1_1$ model alloy crystal was chosen for $Cu_{50}Ni_{50}$ alloy and $L1_2$ for $Cu_{25}Ni_{75}$ and $Cu_{75}Ni_{25}$. $L1_1$ can be represented by an *fcc* unit cell with two base atoms, one base for Cu and one for Ni, along $[111]$ direction separated by $\frac{1}{4}[111]$. On the other hand, $L1_2$ can be represented by an *fcc* alloy that one type of atom sit at corner sites and the others occupy face centers. Figure 4.7 shows the phonon dispersion calculations for both *ab-initio* and the current Cu-Ni alloy EAM potential. It is worthwhile to note that although the developed alloy potentials do not involve any direct fitting to the alloy phonon frequencies, the agreement between EAM and *ab-initio* results for both acoustic and optic modes is quite satisfactory. Furthermore, while EAM predicts optic modes slightly higher for frequencies over 7 THz, the splitting in the optic modes at X and M k points and in between were successfully predicted by the optimized alloy potential. The separation of these frequencies is a clear evidence for a strong dependence to the force constants between Cu-Ni atoms. As the force constants are the second derivatives of the total energy of the system closely related to the elastic constants, such a correct reproduction of the interaction is a clear indication of the quality of the current Cu-Ni alloy potential.

4.3.3 The energy barriers of various diffusion mechanisms for Cu, Ni adatoms on Cu or Ni surfaces

To further test the newly developed potential for the kinetics of materials constructed with Cu and Ni, the energy barriers for various self-surface diffusion mechanisms

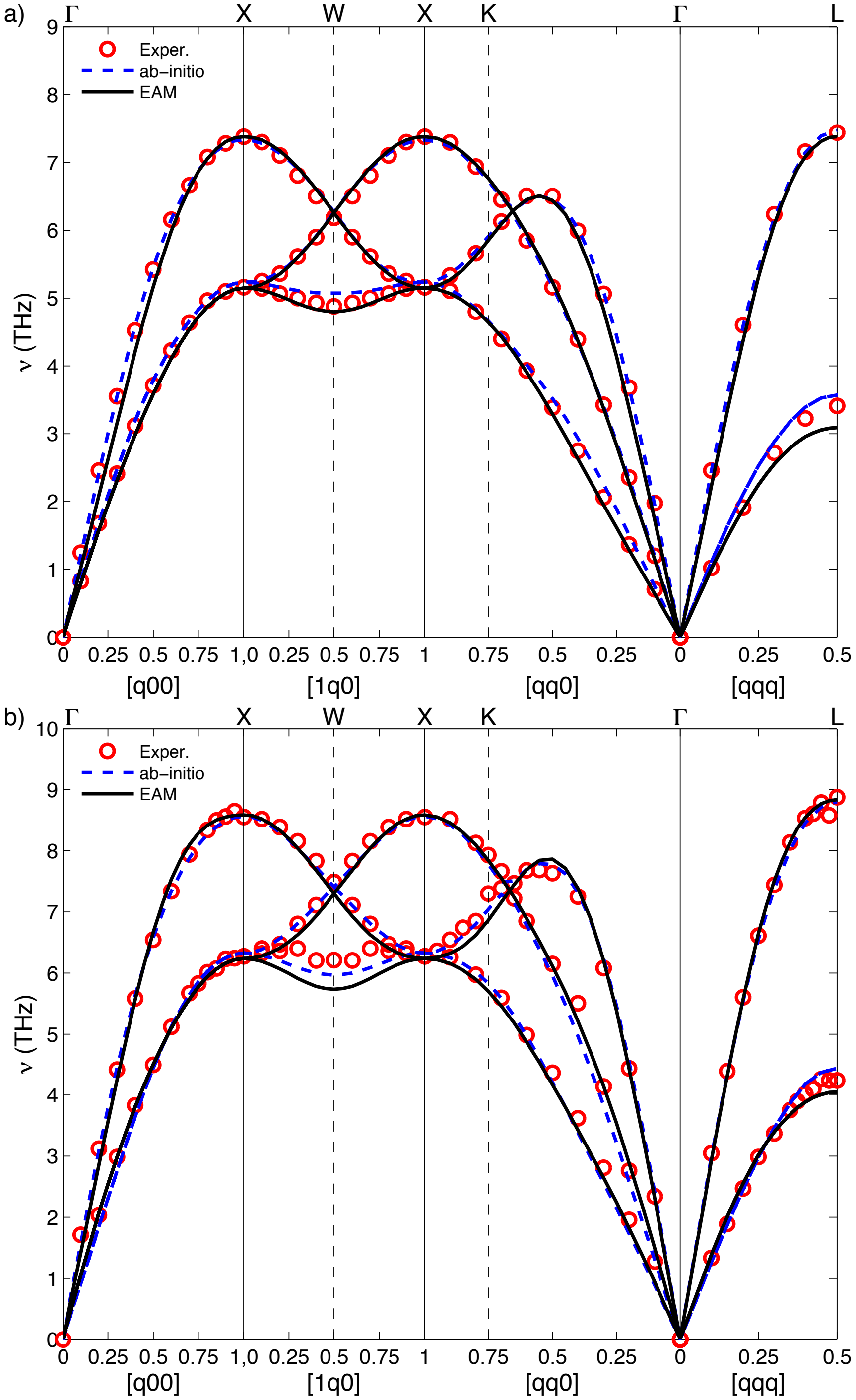

Figure 4.6: Phonon dispersion curves (a) for Cu and (b) for Ni: solid line stands for the values obtained from current EAM, dashed line from *ab-initio* method and hollow circles from the experiment at 80K for Cu [86], 296K for Ni [87].

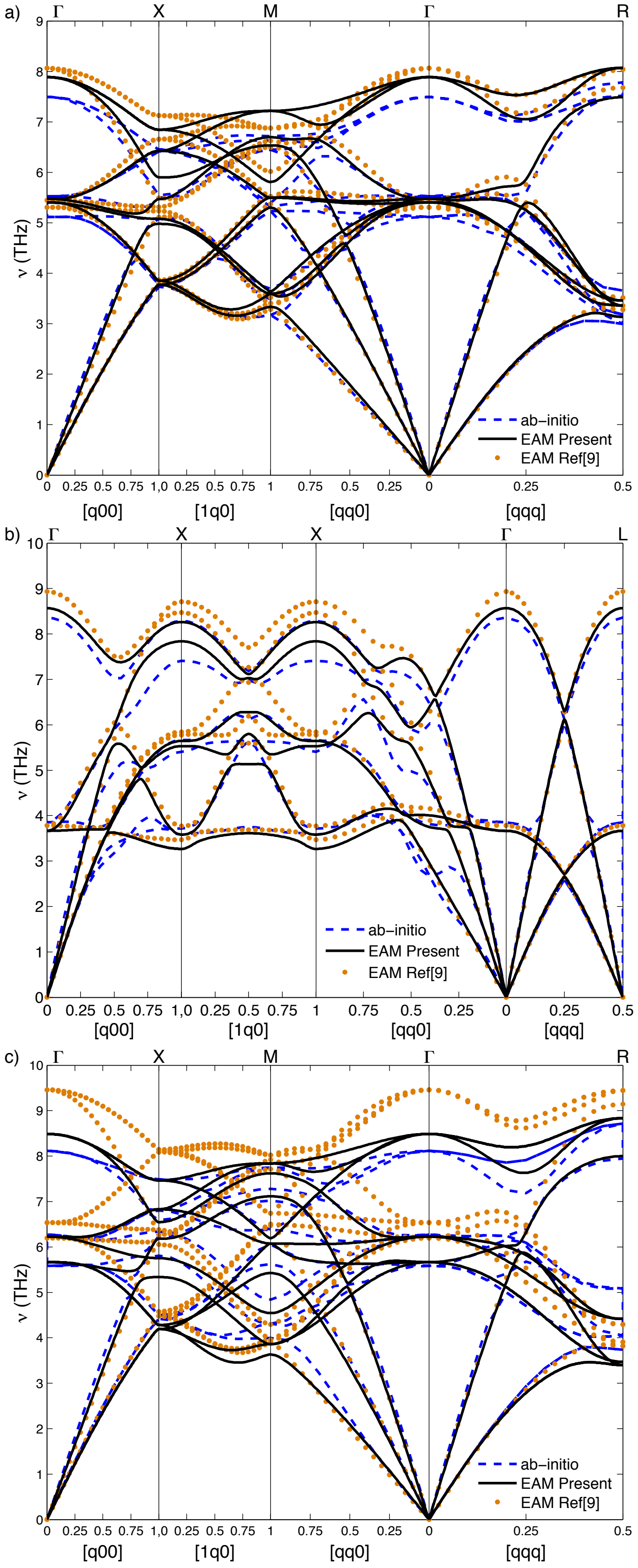

Figure 4.7: Phonon dispersion curves (a) for $L1_2$ Cu_3Ni, (b) for $L1_1$ CuNi, (c) for $L1_2$ Ni_3Cu: solid line represent the values obtained from the current potential, dashed line from *ab-initio* method, and dotted line from Foiles EAM potential [9].

Table 4.7: Diffusion energy barriers (eV) for Cu and Ni adatoms on various Cu and Ni surfaces calculated with the Cu-Ni alloy EAM potential and compared with available experimental, *ab-initio*, or model potential data in Ref. [100].

Mechanism	Experiment	*ab-initio*	Model Pot.	Present EAM
Hopping				
Cu/Cu(111)	0.03-0.06	0.05	0.029-0.044	0.040
Ni/Ni(111)	0.22-0.33	0.16	0.036-0.07	0.031
Cu/Ni(111)	-	-	0.05	0.025
Ni/Cu(111)	-	-	0.045	0.025
Cu/Cu(100)	0.48	0.50	0.44-0.70	0.493
Ni/Ni(100)	0.60-0.63	-	0.63-0.70	0.608
Cu/Ni(100)	0.35	-	0.407-0.62	0.428
Ni/Cu(100)	-	-	0.439-0.64	0.528
Exchange				
Cu/Cu(111)	-	1.455	1.12-1.42	1.361
Ni/Ni(111)	-	2.0	1.633-2.15	1.375
Cu/Ni(111)	-	-	-	1.579
Ni/Cu(111)	-	-	-	1.266
Cu/Cu(100)	-	-	0.18-0.85	0.634
Ni/Ni(100)	0.59	-	0.47-1.307	0.787
Cu/Ni(100)	-	-	1.23	1.043
Ni/Cu(100)	-	-	0.57	0.439

were calculated on the Cu and Ni surfaces with (100) and (111) orientations, using the Nudged Elastic Band [38, 39] method based on the optimized Cu-Ni alloy potential. For each adatom diffusion mechanism, the two types of diffusion process were examined: hopping and exchange. In Table 4.7, the calculated activation energy barriers for several Cu and Ni single atom diffusion mechanisms on the (100) and on (111) surfaces are tabulated. The available experimental, *ab-initio* and model potential results were also included in the table to provide a basis for comparison. A quick glance to the table shows that the predictions from our potential are in perfect agreement with the experimental and *ab-initio* data except for the barriers for Ni adatom diffusion on Ni(111) surface.

5. VIBRATIONAL THERMODYNAMICS OF Cu-Ni ALLOYS

There has been a growing interest in understanding the vibrational thermodynamical properties of the intermetallic alloys with disordered solid solution phase as these properties can sometimes differentiate the chemical order-disorder transitions in the alloys [101–103]. One of the thermodynamical properties that is found to be important in determining the phases of the alloys is the vibrational entropy. Experiments in binary intermetallic alloys [104] show that in many cases the ordering in the alloys decreases the vibrational entropy and disordering does vice versa, since ordering between unlike atoms tend to have stronger bonds. However, V-Fe alloy was observed to be exception as the ordering in the alloy increase the entropy of the system [101].

One of the intermetallic alloys that exhibit continuous random solid solution at elevated temperatures and immiscible at low temperatures is Cu-Ni. The compound has been the focus of several theoretical [105] and experimental [106] studies. Although these studies were in general devoted to determining the change in the thermodynamical properties, magnetic contributions [106], and phase segregation [105] in Cu-Ni alloys, they do not investigate how the lattice dynamics affect mixing or unmixing of Cu and Ni elements. Cu-Ni alloys were investigated with both disorder and order phases in *fcc* structures to determine the effect of temperature dependent vibrational thermodynamical properties. Since transition metals tend to change electronic density of states (DOS) [107,108] in alloys, the electronic contributions to the thermodynamic properties of Cu-Ni were also considered.

5.1 The Theoretical and Computational Details

In thermodynamics, the free energy of a system is described by $F = E - TS$, where E is the internal energy, S is the entropy and T is the temperature of the system. In a crystal, the free energy from lattice dynamics is expected to be the leading component for the most temperature regime [109].

In harmonic approximation, once the standard partition function is defined, the thermodynamic functions for the vibrational free energy F_{vib}, the vibrational entropy S_{vib}, and the lattice heat capacity at constant volume C_v are given by [50],

$$F_{vib} = 3k_B T \int_0^{\omega_{max}} ln \left[2sinh \left(\frac{\hbar\omega}{2k_B T} \right) \right] N(\omega) d\omega, \qquad \textbf{(5.1)}$$

$$S_{vib} = 3k_B \int_0^{\omega_{max}} \left\{ \frac{\hbar\omega}{2k_B T} coth \left(\frac{\hbar\omega}{2k_B T} \right) - ln \left[2sinh \left(\frac{\hbar\omega}{2k_B T} \right) \right] \right\} N(\omega) d\omega, \qquad \textbf{(5.2)}$$

$$C_V^{vib} = 3k_B \int_0^{\omega_{max}} \left(\frac{\hbar\omega}{2k_B T} \right)^2 \frac{1}{sinh^2 \left(\frac{\hbar\omega}{2k_B T} \right)} N(\omega) d\omega, \qquad \textbf{(5.3)}$$

where k_B is the Boltzmann constant, $N(\omega)$ is the normalized total vibrational density of states (VDOS) of the harmonic crystal. In this Thesis, the VDOS of the system was determined using the real-space Green's function (RSGF) [41] technique (See Section 2.8). The vibrational thermodynamic properties of Cu-Ni alloys were calculated within the harmonic approximation of lattice dynamics using the developed potential that was tested accurately reproducing the phonons of both pure Cu, Ni and Cu-Ni alloy *fcc* structures. To have a comparable investigation, these functions were also calculated using the other available alloy EAM potentials (see Chapter 4). The calculations of the VDOS were carried out for both disordered and ordered phases of Cu-Ni *fcc* alloys.

To represent the disordered crystals for each Ni concentration of Cu-Ni alloys, the supercells were first constructed by randomly distributing Ni atoms in a bulk terminated Cu slab and then optimized to the corresponding minimum energy configurations. On the other hand, for ordered crystals, $L1_0$ and $L1_1$ binary structures were chosen to represent 50% Cu-Ni alloys whereas $L1_2$ and $L1_3$ were picked to construct 25% and 75% concentrations, respectively (See Section 4.1.2). For examining the segregation of Cu and Ni atoms in the Cu-Ni alloy, a model system of $Cu_{25}Ni_{75}$ was constructed by filling $1/4$ of the crystal with Cu along (100) layers surrounded by Ni atoms in a periodic structure.

Although the vibrational contributions to the thermodynamical functions are significant in a crystal, the anharmonic and electronic contributions can sometimes be the governing effect. For example, in the case of alloys the electronic effects may play an important role in formation of the crystal structure since mixing of elements can change electronic nature of the structure [108]. Therefore, the change in the free energy to form a binary alloy can be given as following [102]

$$\Delta F = \Delta E_0 + T \left(\Delta S_{conf} + \Delta S_{vib} + \Delta S_{elec} + \Delta S_A\right) \tag{5.4}$$

where S_{conf} is the configurational entropy, S_{vib} is the vibrational entropy, S_{elec} is the electronic contributions to the entropy, and S_A is the contributions from anharmonic effects. In an ideal mixture of an alloy, the change of the configurational entropy is given by [110]

$$\Delta S_{conf}^{mix} = -k_B \left[x ln x + (1-x) ln(1-x)\right] \tag{5.5}$$

where x ($0 < x < 1$) is the concentration of the mixing element. Since the entropy change in Eqn. 5.5 is always positive, mixing unlike atoms increase the entropy of the system compared to unmixing or ordering. On the other hand, the electronic entropy is given by

$$\Delta S_{elec} = -k_B \int n(\varepsilon) \left[f(\varepsilon) ln f(\varepsilon) + (1 - f(\varepsilon)) ln(1 - f(\varepsilon))\right] d\varepsilon \tag{5.6}$$

where $n(\varepsilon)$ is the density of electronic states for energy state, ε, and $f(\varepsilon)$ is the Fermi-Dirac distribution given by [102]

$$f(\varepsilon) = \frac{e^{-\beta(\varepsilon - \varepsilon_F)}}{1 + e^{-\beta(\varepsilon - \varepsilon_F)}} \tag{5.7}$$

where $\beta = 1/k_B T$ and ε_F is the Fermi energy. In Eqn. 5.6, the formalism is similar to the ideal mixing entropy, since electrons can occupy or not occupy each ε with the probability given by the Fermi-Dirac distribution in Eqn. 5.7. To determine the electronic structure and DOS of Cu-Ni alloys, *ab-initio* calculations were carried out for 25%, 50% and 75% Ni concentrations for ordered binary alloys described in Section 4.1.2.

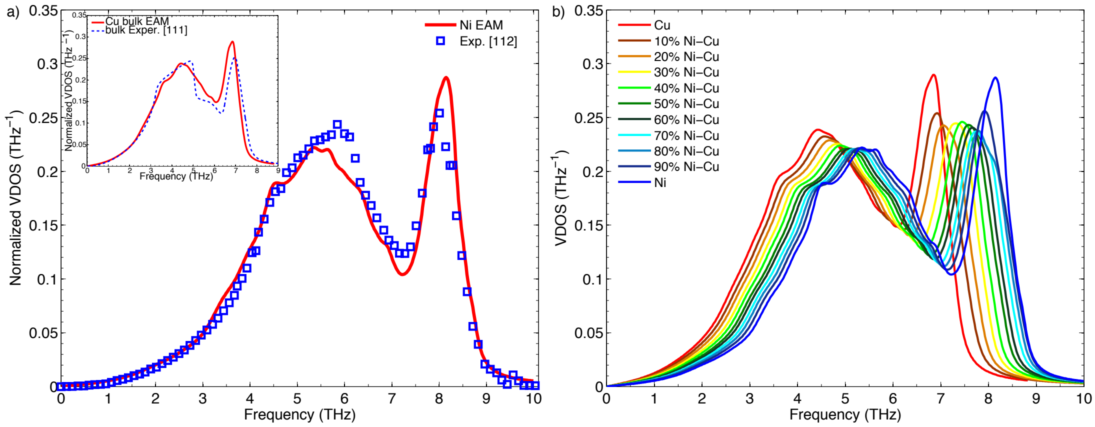

Figure 5.1: VDOS for (a) Cu and Ni (inset) (b) Cu-Ni alloys calculated with the current EAM potential. The experimental curves for pure Cu and Ni from Ref. [111] and [112] are shown for comparison.

5.2 The Vibrational Density of States of Cu-Ni Alloys

Our calculated results for normalized vibrational density of states for pure Cu and Ni are in good agreement with the experimental data presented in Fig. 5.1a. Although major pick at high frequency of pure Ni was accurately reproduced, the peak at around 6.8 THz for pure Cu was found to be slightly lower than the experimental data. To examine the change of phonon states in the Cu-Ni alloys with respect to pure Cu and Ni, the VDOS of various concentrations of Ni were calculated for random solid solutions and presented in Fig. 5.1b. The VDOS for pure Cu and Ni were also presented for comparison. For Cu-Ni alloys, the major low and high frequency peaks shift towards high frequencies as the Ni concentration increases. In an experimental study on specific heat capacity of Cu-Ni alloys, Loram *et al.* [106] proposed a scaling factor f to estimate the VDOS of the alloy using pure Cu VDOS as the reference. In this Thesis, using VDOS of the alloys with varying Ni concentration and the VDOS of pure Cu, the real scaling factors were calculated and presented in Table 5.1 together with the proposed scaling factors in the experiment. The calculated f^{EAM} values were 3-3.5% smaller than f^{Exp} assumptions for 36%-48% Ni concentrations. It is also clear from the table that proposing scaling factors to estimate the VDOS of an alloy using a respective pure-element VDOS might be misleading.

To determine the partial VDOS for Cu and Ni elements in the alloys, the projected phonon states on every atom were averaged over individual element type. Although

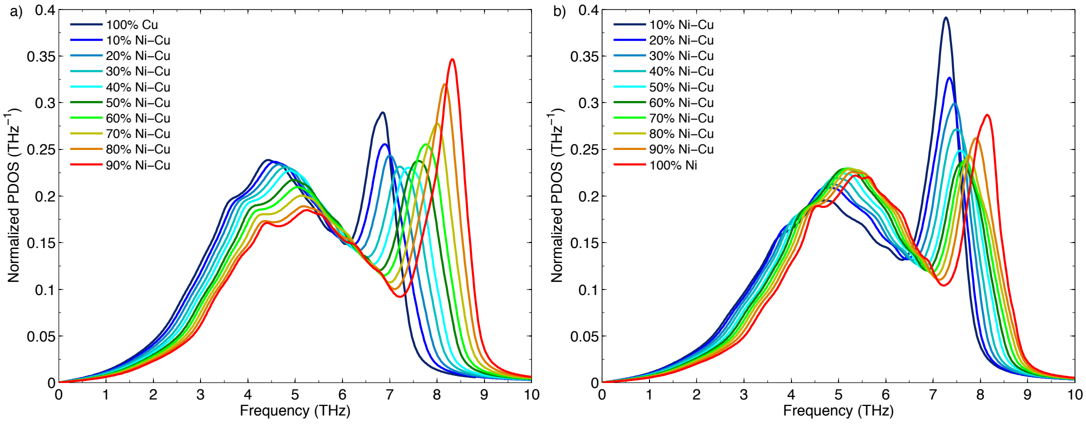

Figure 5.2: The calculated partial VDOS for (a) Cu and (b) Ni in the alloy.

increasing Ni concentration in Cu-Ni alloy enhances the stiffening in VDOS for both Cu and Ni, the stiffening of Cu atoms is more pronounced than Ni atoms at all concentrations in the binary alloys (See Fig. 5.2). It is also interesting to note that the partial phonon DOS of Cu in Ni-rich concentrations of above 80%, the DOS at the high frequency longitudinal modes is more than the Ni DOS for bulk longitudinal modes. It is also worth to note that although Cu and Ni lattice constants, atomic radii differ only by 3% and atomic masses vary by 8%, the overall stiffening of Cu DOS at Cu$_{10}$Ni$_{90}$ is more than 18% with respect to pure Cu. Such result indicates that Ni impurity in Cu crystal substantially changes the force constants between Cu-Cu atoms and Cu-Ni atoms in the solid solution. A similar local stiffening characteristic between Au-Au and Au-Fe bonds had recently been observed for Au-Fe alloys [101]. In the same study, the electronic structure was also calculated by *ab-initio* methods and the stiffening in partial phonon DOS of Au was attributed to the charge transfer to the nearly free band of *s* electrons, and stronger *s-d* hybridization with increasing Fe concentration.

To analyze the VDOS change in ordering and unmixing, the vibrational DOS of order phases for 25%, 50%, and 75% Ni concentration were calculated. The resulting VDOS for each ordered and segregated systems were presented in Fig. 5.3 together with the disordered Cu-Ni crystal results. Although the change in VDOS curves for 25% and 50% Ni ordered alloys was small, those of ordered 75% Ni alloys differ considerably. As seen in Fig. 5.3, the ordering tends to increase the contributions of transverse DOS with the additional peaks and generally decreases DOS for longitudinal modes.

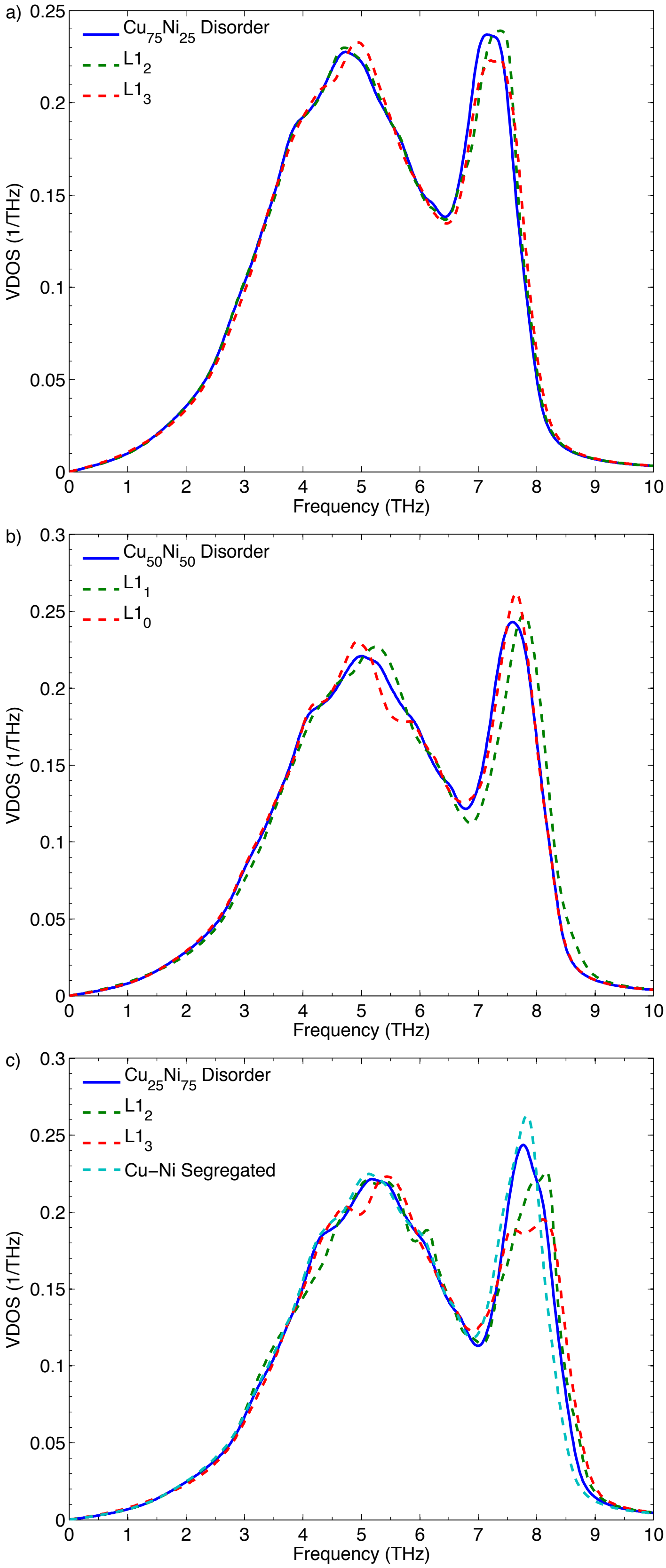

Figure 5.3: The vibrational DOS for ordered (a) $Cu_{75}Ni_{25}$, (b) $Cu_{50}Ni_{50}$, and (c) $Cu_{25}Ni_{75}$ alloys calculated with the current EAM potential together with the disordered and segregated Cu-Ni alloys VDOS.

Table 5.1: The VDOS shifting factor f for Cu-Ni alloy with respect to the pure Cu phonon spectrum.

$X_{Ni}(\%)$	Proposed Scaling Factor [106]	Present EAM	$f^{Exp} - f^{EAM}$
25	1.080	1.0417	3.55%
36	1.108	1.0795	2.57%
41	1.118	1.0883	2.97%
48	1.133	1.1029	2.66%
50.5	1.138	1.1058	3.22%
53	1.143	1.1087	3.43%
70	1.179	1.1262	5.28%
100	1.240	1.1874	5.26%

In contrast to ordered alloy DOS, states for longitudinal modes increase moderately in the segregated solid solution while almost no change happens in transverse DOS. A similar behaviour was reported by Alam *et al.* [113] for Fe-Cr alloys via analysis of short-range ordering where the change in transverse mode DOS was found to lie on ordering or segregation in the alloy. For the ordered structure of Fe-Cr, the low frequency DOS of transverse mode increases and the high frequency DOS decreases, for segregated phases, on the other hand, the DOS changes slightly in the opposite way.

5.3 Heat Capacity of Cu-Ni Alloys

The vibrational heat capacity at constant volume for pure Cu and Ni elements was presented in Fig. 5.4a, together with the estimated electronic contributions, calculated by [12]

$$C_V^{elec}(T) = \frac{\pi^2}{3} n(\varepsilon_F) k_B^2 T, \tag{5.8}$$

and experimental curves [114]. As seen in the figure, the characteristics of specific heat for both elements were substantially governed by the lattice vibrations until 150K above which both electronic and anharmonic effects become noticeable. Furthermore, both the electronic and anharmonic effects were more pronounced for Ni than Cu. For Ni, on the other hand, magnetic effects are expected to be important for temperatures above 500K.

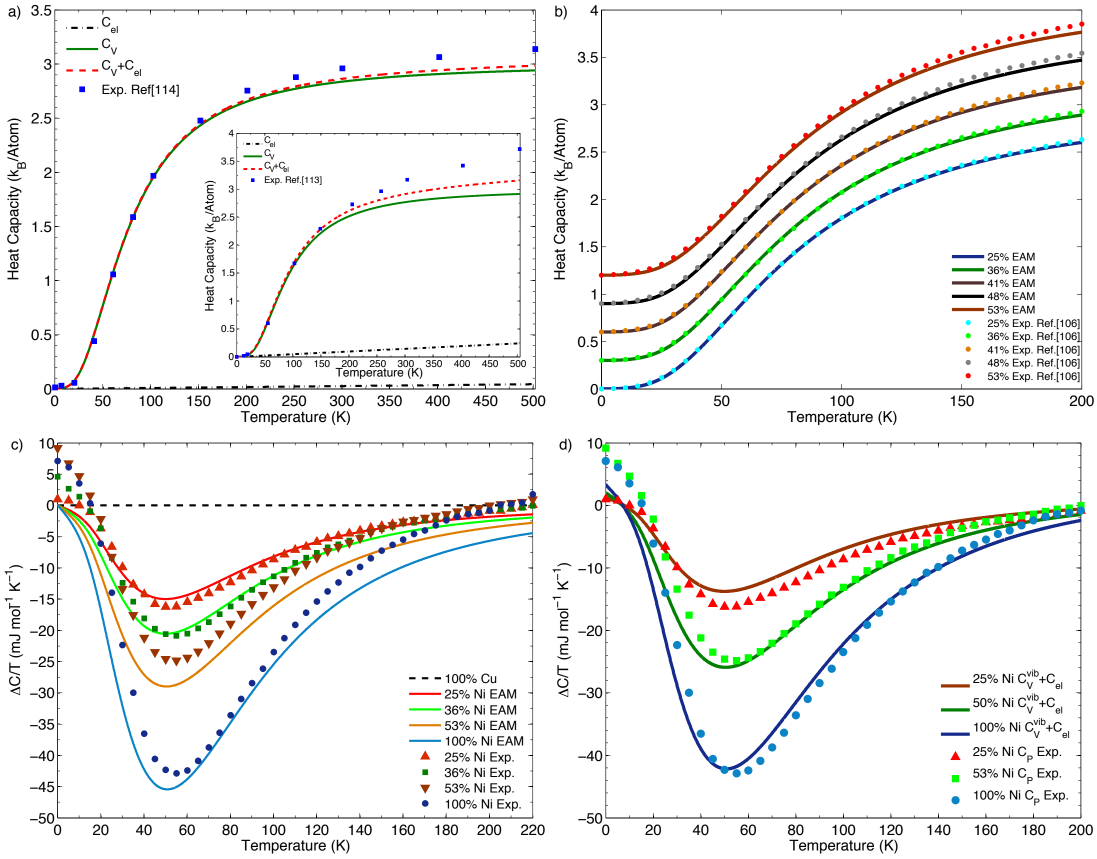

Figure 5.4: The vibrational heat capacity calculated with the current EAM potential (a) for pure Cu and Ni (inset) (b) for various Cu-Ni alloys in addition to the excess vibrational heat capacity calculated with the current EAM potential (c) for various Cu-Ni alloys (d) when the electronic contributions were accounted. The experimental values for pure elements from Ref. [114] and for Cu-Ni alloys from Ref. [106] are shown for comparison.

In Fig. 5.4b, the heat capacity for Cu-Ni alloys with various concentrations was plotted and the experimental curves were also presented [106]. Note that the experimental curves were measured at constant pressure, C_P, and involve both anharmonic and electronic effects. The results for higher temperatures could not be compared as the experimental values were available only for the temperature range between 0-200K. It is clear from the figure that for the disordered alloys of all concentrations, the vibrational contribution completely determines the nature of the specific heat that is consistent with the observation for pure Cu and Ni.

In Fig. 5.4c, the excess vibrational specific heat per temperature, C_v/T, for several Ni concentrations in comparison with the experimental results of excess C/T was plotted. Here, the excess thermodynamic quantities of the alloy were determined with respect to the heat capacity of pure Cu. As seen in the figure, the characteristics of C_V around 0K were mostly governed by the other contributions rather than phonons. With increasing temperatures the curve was largely controlled by the lattice vibrations. Even the position of the peak around 55K was determined by the phonons. As temperature increases to 200K, probably, the electronic or magnetic effects pull the curve towards the 0 value of C_V or above. Although the agreement on the excess Cu-Ni heat capacity curves of EAM calculations and experimental values was overall satisfactory for 25% and 36% Ni concentrations in 60K-100K range, the deviation from the experimental values were more pronounced for 53% and 100% concentrations.

Further calculations were performed to see the effect of electronic states, excess specific heat using Eqn. 5.8 and the results were presented in Fig. 5.4d. There is a clear betterment in the agreement between the experimental and the calculated heat capacity once the electronic contribution was added.

5.4 Free Energy and Entropy Calculations for Cu-Ni Alloys

To further analyze the thermodynamics of Cu-Ni, vibrational free energy and entropy were also calculated with the developed EAM potential. Using Eqn. 5.1, the vibrational free energies for various Cu-Ni compounds were calculated and plotted in Fig. 5.5a. The concentration weighted excess free energies for Cu-Ni alloys were also presented in Fig. 5.5b. The free energies of Cu-Ni alloys increased with increasing Ni concentration in the solid solution which is expected as addition of Ni atoms in Cu-Ni alloy stiffens the bonds of Cu-Cu and Cu-Ni. The concentration weighted excess free energies of various Cu-Ni alloys were calculated by

$$\Delta F_{vib} = F_{vib}^{x} - (1-x)\,F_{vib}^{Cu} - xF_{vib}^{Ni} \qquad \textbf{(5.9)}$$

where x is the Ni concentration in the alloy and presented in Fig. 5.5. As seen in the figure, for all temperatures the excess free energy exhibited a maximum at about 46% Ni concentration and the excess free energy of the compound increased with increasing temperature. When compared to the mixing enthalpy (See Fig. 5.5c), the vibrational excess free energy is rather small which shows that governing contribution to the excess energy is coming from the electrostatic interactions in the Cu-Ni alloys.

In this Thesis, the vibrational entropy of the disordered and the ordered Cu-Ni alloys for various Ni concentrations was also calculated. The results for the partial entropy of Cu and Ni in the alloys and the total entropy of Cu-Ni compounds for each Ni concentrations were presented in Fig. 5.5d and Fig.5.5e, respectively. As seen in the figures, increasing Ni concentration in the alloy decreases the partial entropy for both elements which may be traced back to the observed stiffening in the respective VDOS for Cu and Ni. The calculated entropy values of 3.97 and 3.42 $k_B/Atom$ at 300K are in consistent with the experimental results of 3.90 and 3.40 $k_B/Atom$ for Cu and Ni, respectively [104, 115]. Although there is more or less a linear dependence for Cu in all concentrations, for Ni the slope of the partial entropy changes slightly and then followed by a sharp change at 75% Ni concentration.

The partial entropies of Cu and Ni in the ordered crystal and the total entropy of the alloy in the ordered phase were also calculated, using Eqn.5.2. The difference between the partial entropy of the Cu in the ordered and disordered crystal of $Cu_{25}Ni_{75}$ is observed to be larger, with 0.04 $k_B/Atom$, but its end contribution to the change in the total entropy of the alloy is just 0.01 $k_B/Atom$. Such decrease in the entropy is too low for a phase transition in the alloy since experimental results for Ni-Al, Cu-Au, and Ni-Pt alloys [102,104,110] show that the change in the entropy needs to be in the order of 0.07-0.2 $k_B/Atom$ for a phase transition to occur. Although ordering tends to change the entropy significantly in alloys [104], the current simulations for Cu-Ni alloys do not show similar characteristics. This may indicate that transition of disordered phase, ordered phases can locally be occurred and easily dissolved in the solid solution.

To investigate the disordered phase of Cu-Ni one should calculate the mixing entropy:

$$\Delta S_{vib}(x_{Ni}) = (1 - x_{Ni})\, S^{Cu}_{vib}(x_{Ni}) + x_{Ni} S^{Ni}_{vib}(x_{Ni}), \qquad \textbf{(5.10)}$$

where x_{Ni} is the Ni concentration in the alloy and ΔS^{t}_{vib} is given by

$$\Delta S^{t}_{vib}(x_{Ni}) = S^{t}_{vib}(x_{Ni}) - S^{t}_{vib}. \qquad \textbf{(5.11)}$$

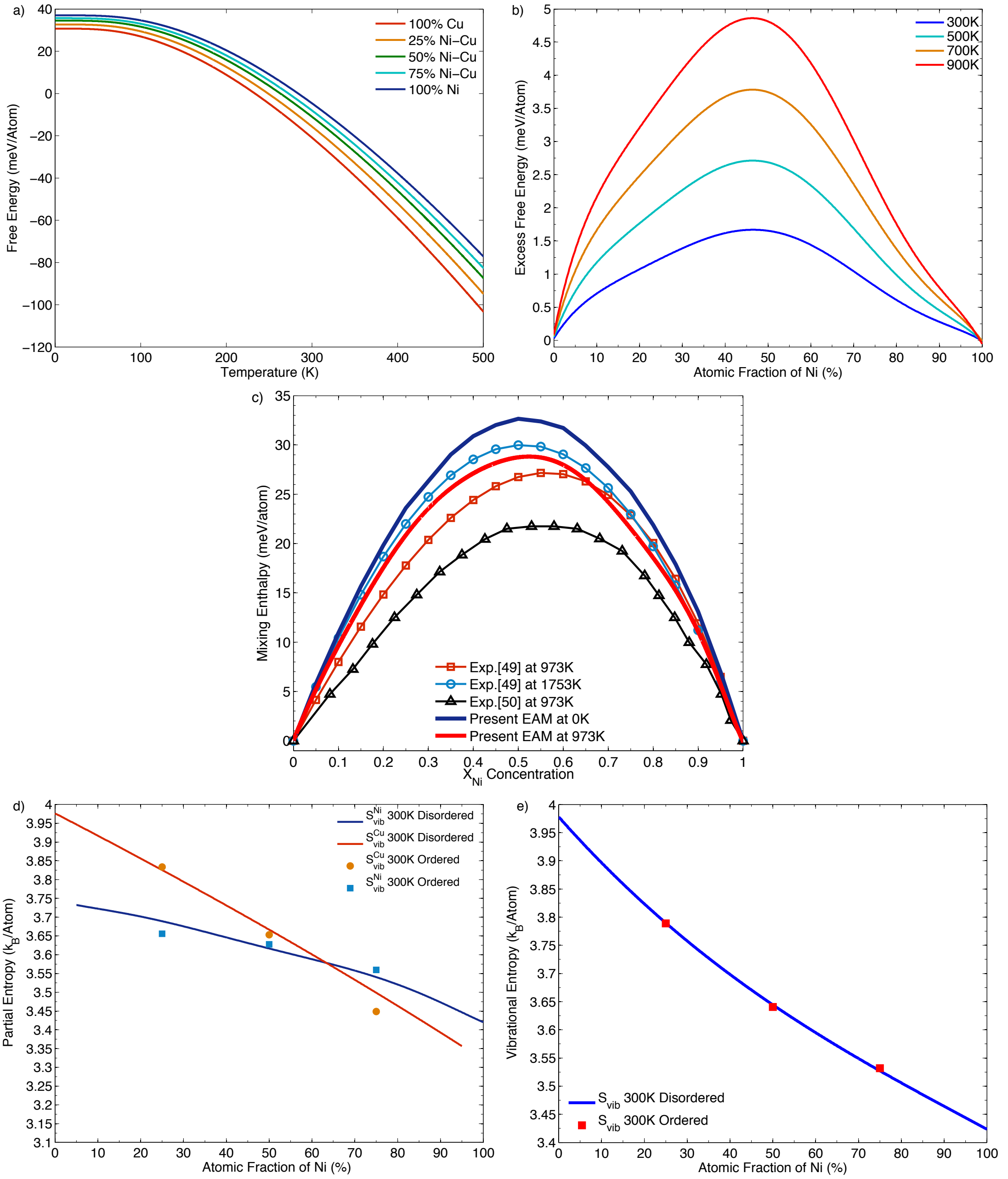

Figure 5.5: (a) The vibrational free energy for Cu-Ni alloys, (b) the concentration weighted excess free energy, (c) mixing enthalpy, (d) the partial and (e) total vibrational entropy for various Cu-Ni alloys and ordered phases calculated with the current EAM potential.

Here, S^t_{vib} is the vibrational entropy of pure element t. To compare the results with configurational entropy S_{conf} for ideal solution and the experimental results, the concentration weighted vibrational entropy of Cu-Ni is presented in Fig. 5.6a and Fig. 5.6b, respectively. As seen in figure, the results are in good agreement with the experiments at 300K with negative values in all the concentration range. While vibrational entropy curve generally gives the trend of mixing entropy at 300K, the minimum about 35-40% can be predicted to be around 43%. For Cu-Ni alloys, while vibrational contribution is important at low temperatures, it is predicted to be less dominant at elevated temperatures. Although an increase in temperature decreases mixing entropy by 0.1 J mol^{-1} K^{-1}, it is not sufficient to match the calculated mixing entropy curve with the experimental one at high temperatures.

To see if the effect of the electronic contribution to the mixing entropy is significant, further calculation was performed using Eqn. 5.6 for Cu-Ni alloys with 25, 50 and 75% Ni concentrations and the results were presented in Fig. 5.6b. The vibrational entropy has an order of magnitude higher contribution than the electronic one. However, the concentration weighted mixing entropy for higher temperatures above 300K exhibited distinct results for electronic contributions. At 700K, the results were in comparable with the vibrational contributions with negative mixing values and above 700K the electronic contributions were slightly more pronounced than vibrational contributions. Notice that the total contribution of electronic and vibrational entropy was almost coincide with the experimental values at 1000K. However, as seen in Fig. 5.6 these values were significantly small compared to configurational entropy. Keep in mind that mixing is always favored in *fcc* by configurational entropy. Therefore, Cu-Ni alloys have always tend to construct a disordered solid solution in all concentrations. However, the vibrational and electronic entropy favor unmixing with negative values [101] and contribute to the miscibility gap of Cu-Ni phase diagram [105]. At elevated temperatures electronic entropy contributions to the unmixing were more pronounced. The electronic contribution to unmixing is a well-known fact in Cu-Ni alloys and experimental and theoretical results show that the magnetic effects are also important in the determination of the miscibility gap [105].

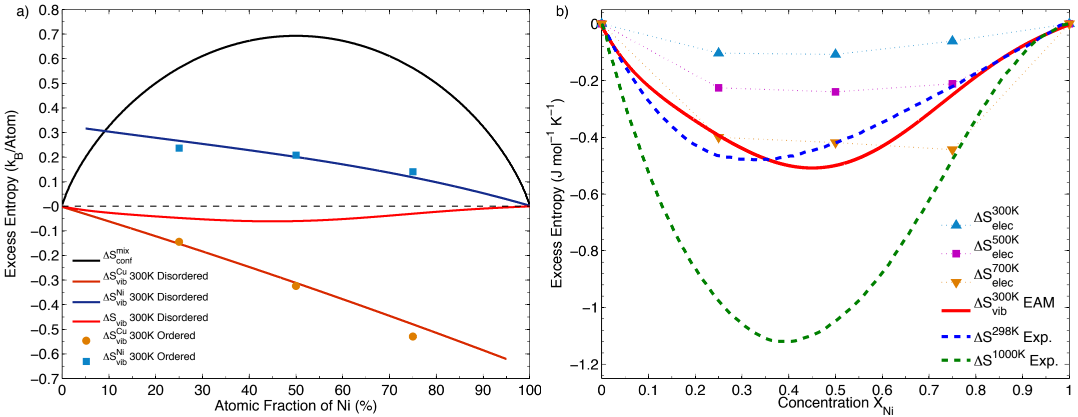

Figure 5.6: The vibrational excess entropy compared (a) to the partial and configurational entropies and (b) to the experimental results from Ref. [98] at 298K and Ref. [97] at 1000K.

6. THE GROWTH OF Ni AND Cu-Ni NANOSTRUCTURES ON Cu(111) SURFACE

In this Chapter of the Thesis, it was aimed to perform Molecular Dynamic simulations to further test the alloy potential for the pure Ni and Cu-Ni island growth on the Cu(111) surface upon Ni deposition and then to determine the kinetic nature of the growth by calculating energy barriers for various diffusion processes using NEB method.

6.1 The Evolution of Ni and Cu Add/Vacancy Islands on Cu(111)

The molecular dynamic simulations were build on the two experimental observations [116]: 1) the motions of the islands on Cu(111) surface and 2) the growth of nanostructures with deposition of Ni adatoms. Monolayer and vacancy Cu islands were constructed side-by-side with mono or double layer Ni islands on top of a substrate as presented in Figs. 6.1a, 6.2a, 6.3a, and 6.4a. The supercells representing the systems on Cu(111) surface were constructed with a slab of 24 layers where each layer contains 768 atoms corresponding to approximately 72x61Å^2 surface area which is big enough to minimize the boundary and end effects on the system. An infinitely extended surface was constructed by imposing periodic boundary conditions only along the directions parallel to the surface of the slab. To provide the experimental conditions of vacuum chamber, the temperature of the system was raised to the desired temperature with an incremental steps of 50K through NVT simulations after equilibrating the slab at 0K. Each NVT simulation of 100 *picosecond (ps)* was followed by an NPT simulation of 100 *ps* at 0 *atm*. After thermalization, the systems were allowed to evolve to their final configurations using constant energy (NVE) simulations. Although the experiments were carried out at room temperature, the simulations were run at 700K so that growth characteristics in the simulations could be observed in a reasonable time scale. The evolution of the islands were recorded until 250 *ps* after the formation of a stable island in the simulations. In the first scenario where both of Cu and Ni adatom islands had a height of monolayer, Cu atoms from the adatom island migrated to the upper layers of Ni island and covered the whole Ni layer in 1300 nanoseconds (See Fig. 6.1). In the simulations, Cu atoms of the island first migrated to a second nearest neighbor separation of Ni island and built a bridge between the two islands at about 450ns. Once the first contact with Ni island was established, Cu atoms surrounded Ni island. Within about 200 ns simulation time, the Cu atoms in the periphery of the Ni island started jump attempts to upper layers of Ni. The average attempt frequency was calculated to be 23.5ns^{-1} before a dimer formation occurred at 728ns (See Fig.6.1i). On the average, a single Cu atom that jumped to the upper layer of Ni island before any dimer formation, stayed on the Ni island about 5 ns. Interestingly, after the formation of second chain around Ni periphery by the migrating Cu atoms, the average attempt frequency was raised up to 5 ns^{-1} , which was about 5 times higher than the overall attempt frequency in the whole 1.6 microsecond simulation time. With growing Cu chains around the periphery of Ni island, Cu atoms could stay up to 10 ns on the top of Ni island, which was the twice the average time for a single atom motion on the Ni island. As shown in Fig.6.1i, after two jump attempts of Cu atoms with 5ns^{-1} frequency, a dimer formation was observed. Although the attempt frequency decreased after formation of a dimer, every jumping Cu atom eventually merged into the cluster and stayed there until the Ni island was completely covered. Further simulations were carried out for islands separated by 2, 4, and 6 nearest-neighbor (nn) to observe if a threshold separation for the merge of the heterogeneous islands existed. The results showed that for 2 and 4 nn separations, Cu islands could cover the Ni islands, while no such covering happens for the separations over 6nn even for the simulations over 500ns (See Fig.6.2). This threshold of 1.5nm length seems to be reasonable as the smallest separation of the islands without any contact in the experimental work can be estimated to be within 1-3 nanometers (See Fig.1 both in Ref. [116] and Ref. [117]).

The second scenario included a double layer Ni island near a mono layer Cu island. The dynamics of the process was as following: Cu atoms directly migrated to the upper layers skipping the decoration of periphery of bottom layer and covered the first layer within 175ns time (See Fig.6.3). Although in both scenarios, Ni islands did not move and change the shape on the surface within the simulations time of 1.6μs

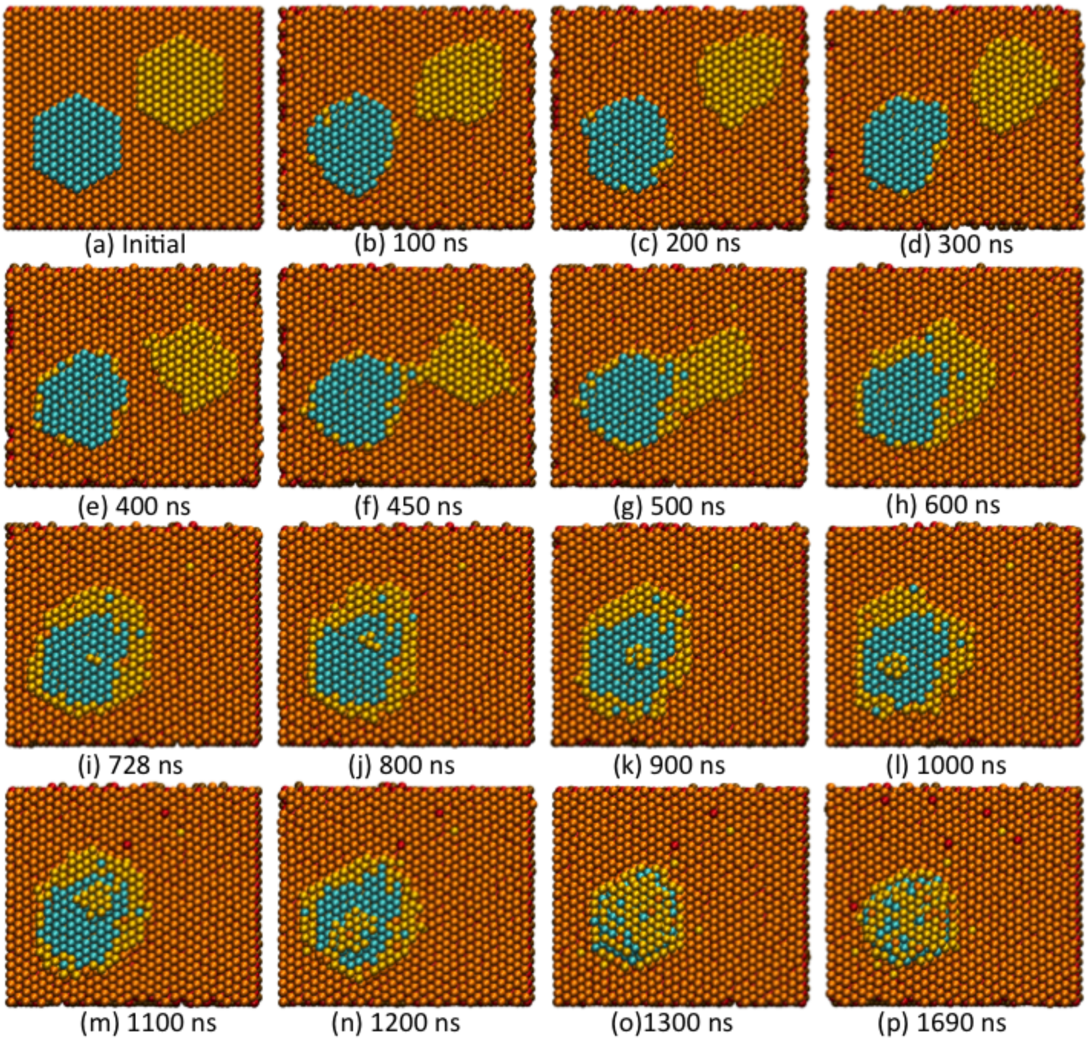

(a) Initial (b) 100 ns (c) 200 ns (d) 300 ns

(e) 400 ns (f) 450 ns (g) 500 ns (h) 600 ns

(i) 728 ns (j) 800 ns (k) 900 ns (l) 1000 ns

(m) 1100 ns (n) 1200 ns (o)1300 ns (p) 1690 ns

Figure 6.1: The snapshots of the evolution for monolayer Ni (blue) and Cu (yellow) islands on Cu(111) surface (1st layer: orange, 2nd layer: red). (a) Initial configuration, (b)-(p) the snapshots of the system at the end of every 100ns, except (f), (i) and (p) where the first one shows the formation of the bridge at 450ns, the second one shows dimer formation at 728ns and the last one shows the final configuration at 1690ns.

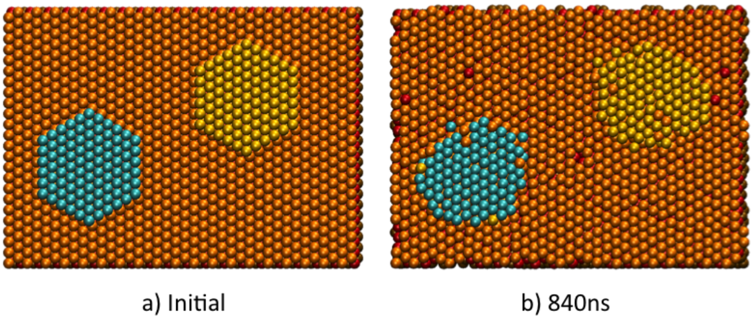

a) Initial b) 840ns

Figure 6.2: (a) The initial and (b) the final configuration after 840ns simulation of monolayer Ni (blue) and Cu (yellow) islands with 6nn separation on Cu(111) surface (1st layer: orange, 2nd layer: red).

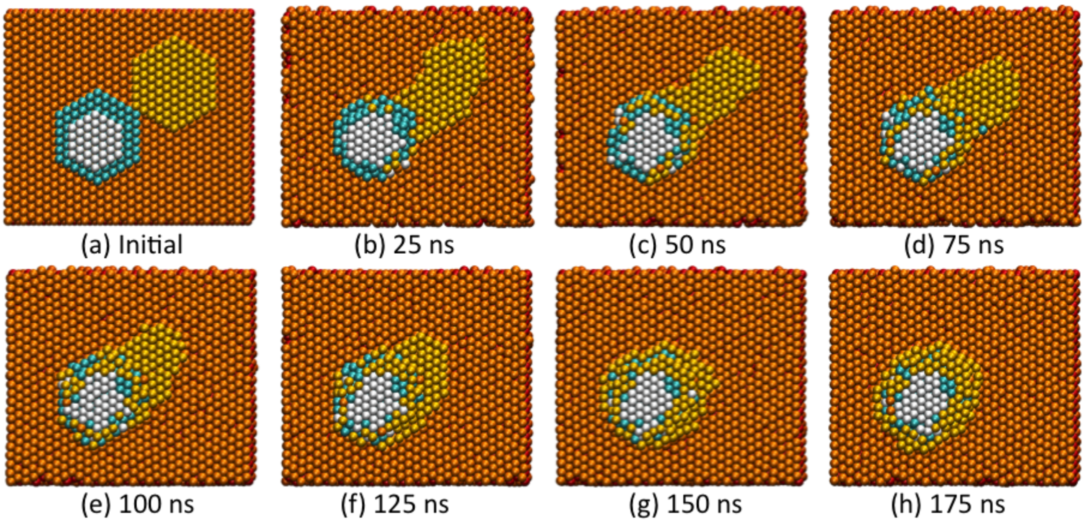

Figure 6.3: (a) The initial and (b-h) configurations after each 25ns simulations of double-layer Ni (bottom:blue, top:white) and Cu (yellow) islands on Cu(111) surface (1st layer: orange, 2nd layer: red).

(See Figs.6.1 and 6.4), the nature of migration of Cu island as a whole could show different characteristics depending on the nearby Ni island formation. In addition, the coverage of Ni islands by Cu atoms increased about 7.5 times when the Ni island had double layers. Interestingly, Ni atoms, together with the migrating Cu atoms, were also observed to jump to the upper layer (See blue atoms at the top layers in Fig. 6.1 and 6.3).

The other MD simulations involved Cu vacancy islands near mono and double layer Ni islands. The snapshots of these processes were shown in Fig.6.4 and 6.5. The migration of Cu atoms at the periphery of the vacancy islands to the very close proximity of the Ni island happened for both cases whereas Cu atoms could cover the top of the first layer when the Ni island had two layers. It seems that existence of second layer in Ni island helps Cu atoms directly migrate to the top of the first layer before surrounding the periphery of the island. Although Cu atoms had some jumping attempts to the top of the single-layer Ni island, complete coverage of the island did not occur even for a simulation of 1000ns (See Fig. 6.5). In the presence of single-layer Ni island, the jump attempt frequency for the Cu atoms of the mono-layer vacancy island was calculated to be 63ns^{-1}, that was less than half of the attempt frequency

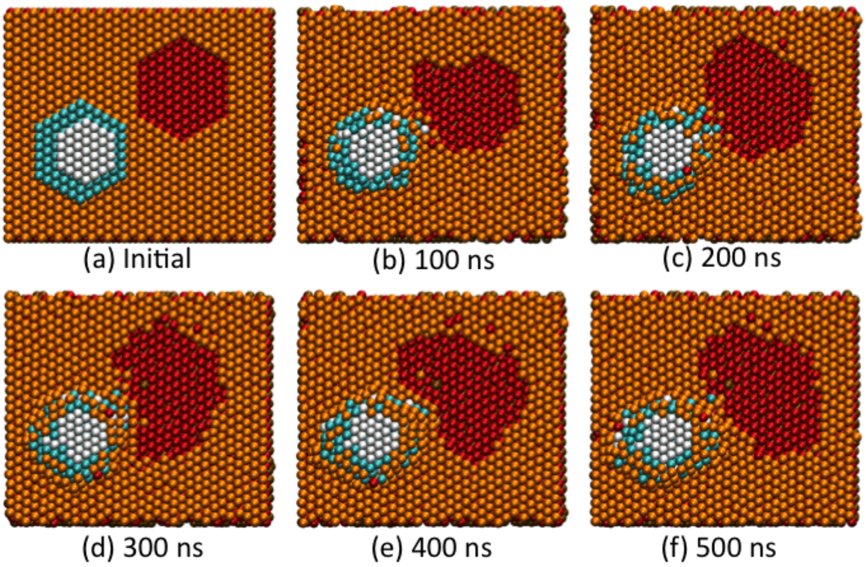

Figure 6.4: The (a) initial configuration and (b-f) configurations after each 100ns simulation steps of double-layer Ni (bottom: blue, top: white) and vacancy Cu islands on Cu(111) surface (1st layer: orange, 2nd layer: red).

of Cu atoms of single-layer island. Such a low jump rate might be due to the low concentration of Cu atoms around the Ni island.

In the recent scanning tunneling microscopy (STM) experiments, it was observed that in addition to the pure Ni islands, Cu-Ni islands were also assembled upon under one monolayer Ni deposition on Cu(111) surface [116–118]. The main outcome from the experiments were that Cu atoms from the Cu(111) surface decorate the upper layers of Ni islands. The resulting configurations of coarsening simulations were generally well agrees with these experiments, where Cu decorations to the upper layers of Ni islands were observed. Simulations showed that whenever there were enough Cu atoms free to move in the close vicinity of Ni islands (about 4nn), Cu atoms could decorate or cover the islands. The final configurations of Ni and Cu-Ni islands were also similar to the islands observed in the experiments. The composition and the growth of the islands are very often correlated with the strong magnetic moment of the Ni nano-structures on Cu(111) [118]. However, the current simulations can not point any such magnetic dependency as the developed interatomic potential does not include spin effects to the charge density. Under 0.3 ML deposition the effect of the magnetic moment is measured to be quite low [118], suggesting a non-magnetic nature in the very first stages of the growth. Interestingly, the experimental results for the formation of Ni

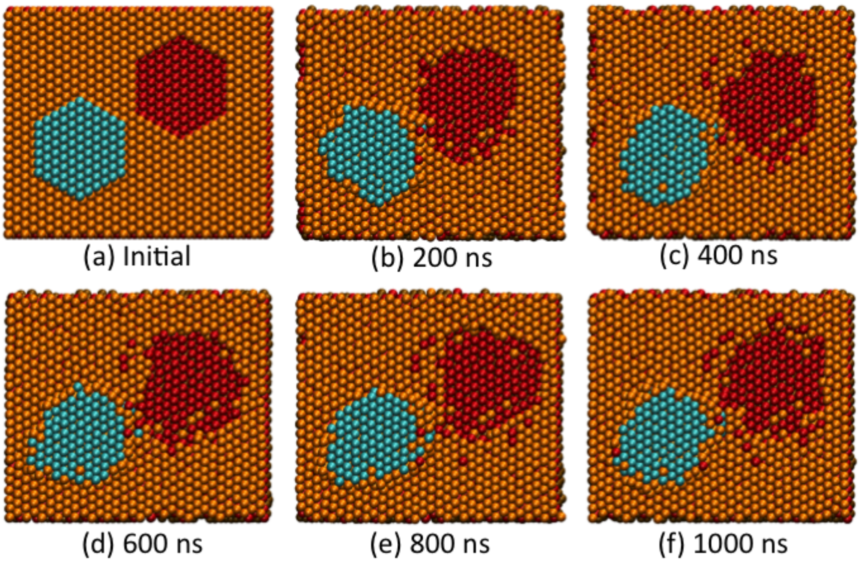

Figure 6.5: (a) The initial and (b-f) the configurations after each 200ns simulation steps of monolayer Ni (blue) and Cu vacancy islands on Cu(111) surface (1st layer: orange, 2nd layer: red).

islands above 0.3 ML deposition rates still are in very good agreement with current MD simulations. These findings show that Ni islands on Cu(111) under 1 ML deposition have not a strong dependence on the magnetization.

6.2 Sub-Monolayer Ni Deposition on Cu(111)

Simulations for Ni deposition on Cu(111) surface was carried out using the Cu(111) slab shown in Fig. 6.1. The supercell was first optimized to its minimum energy configuration. Then the temperature was increased up to 300K. During deposition the system was held at this temperature using constant-temperature (NVT) simulations. Two deposition regimes were considered: a uniform deposition with fixed time intervals and a nonuniform deposition with random time intervals. For uniform regime, five different deposition rates were considered; 0.5, 1, 2, 5, and 10 nanoseconds. In the simulations, 85 Ni atoms (0.1 ML) were deposed on the Cu surface. Ni islands generally grow in 3-dimension for the deposition rates of 5ns or faster. On the other hand, for 10ns and slower deposition rates, Ni islands tend to grow 2-dimension in a more hexagonal shape monolayer island structures.

For nonuniform regime, the depositions were carried out in random intervals between 2ns and 5ns. More than one Ni islands were formed with 2-dimensional characteristics

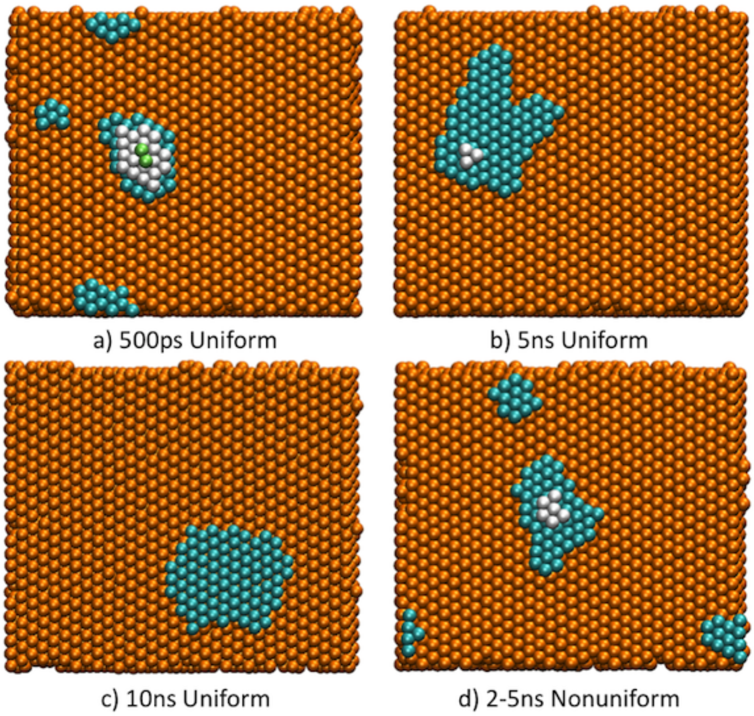
a) 500ps Uniform
b) 5ns Uniform
c) 10ns Uniform
d) 2-5ns Nonuniform

Figure 6.6: The snapshots of the final configurations of Ni atoms (top: green, middle: white, bottom: blue) on Cu(111) surface (1st layer: orange, 2nd layer: red) for (a) 500ps uniform, (b) 5ns uniform, (c) 10ns uniform and (d) 2-5ns nonuniform Ni deposition simulations.

that were similar to the characteristics of islands formed in 5ns uniform deposition rate.

6.3 The Structural Properties of Ni and Cu-Ni Islands on Cu(111)

In the STM experiments, the height of the pin along a profile both on pure Ni and Cu-Ni islands were also measured to investigate the geometric characteristics of the Cu-Ni mixing [116–120]. The first layers of islands were measured to be unexpectedly low about 1.3Å height for monolayer islands constructed with pure Ni or Cu-Ni alloy. In contrast, the height of 1 ML Ni island covering Cu(111) surface was found to be around 2.1Å in the experimental studies [116–120]. Moreover, the experimental results showed that the bilayer island heights differed quite a lot about 0.7Å with 3.3Å and 4.0Å for pure Ni and Cu-Ni alloy islands, respectively.

To have an estimate on the heights of the layers, two types of Ni and Cu-Ni islands were constructed (see Fig.6.7a). Here, the island sizes were chosen to mimic the experimental results. Both Ni and Cu-Ni islands were first optimized to the minimum

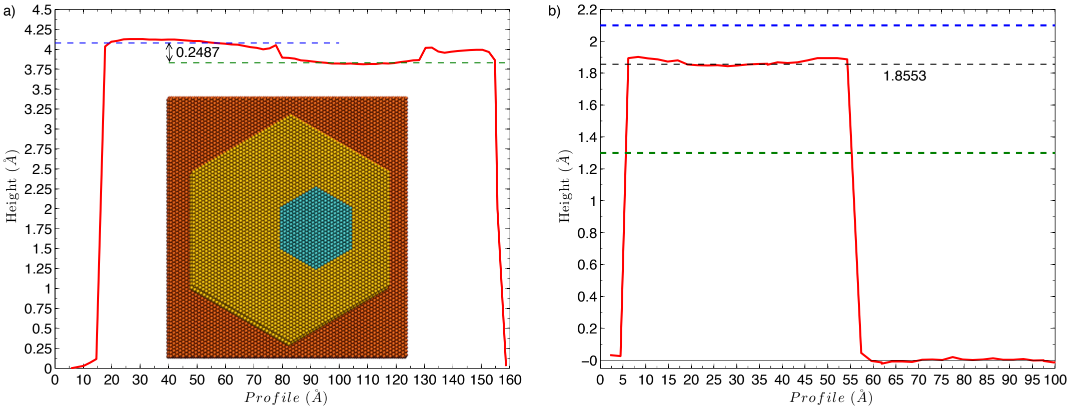

Figure 6.7: The average heights for the predefined profile on (a) double-layer Cu-Ni islands (inset shows top view of the supercell where blue and yellow atoms represent Ni and Cu, respectively) and (b) monolayer Ni island.

energy configurations and then the systems were heated up to 300K with two-step process: a 200ps NVT followed by a 200ps NPT simulation. As STM experiments were carried out at temperatures 5K-40K, the supercells at 300K were cooled down to 40K with additional 200ps NVT simulations. The positions of the highest atoms in a predefined profile in the final configurations were averaged over an additional 100ps NVT simulations and the resulting height profile was presented in Fig.6.7b.

As seen in the figure, the average height of the double layer island is in good agreement with the experimental results. In MD simulations, the height of the monolayer islands was found to be lower than the height of a single-layer Ni island on Cu surface which was consistent with the results in the experiments. Furthermore, the second layer heights of Cu-Ni islands were also found to have different heights (See Fig. 6.7b) in agreement with the experiments. The main reason for such low monolayer heights and different second layer heights were that Ni islands relaxed downward more than Cu ones on Cu(111) surface.

6.4 The Kinetics of Ni, Cu Adatoms on Cu(111)

To understand the nature of Cu decoration in the Ni islands on Cu(111), the energy barriers for the possible diffusion mechanisms in the simulation were investigated using nudged-elastic band (NEB) [38, 39] method. A brief list of the energy barriers for the possible diffusion mechanisms were given in Table 6.1. Here, two types of diffusion mechanisms were considered for the adatom diffusions: hopping and exchange. For the downward processes for monolayer islands, the exchange mechanism had rather smaller energy barriers in contrast to hopping in all conditions for both Cu and Ni adatoms, which was an expected result. However adding a second layer to the islands, the energy barrier for the exchange processes were doubled for Ni islands and increased 4 times for Cu islands. Therefore, by increasing the layer in the steps, the adatom diffusion from the step of the island turned out to be a formidable task. Another interesting result was that the energy barriers for upward diffusions were decreased for both Cu and Ni adatoms at Cu step, but it was more pronounced for Cu atoms at the vicinity of Ni step, where Cu migration to the upper layers of Ni islands was generally biased by this process. The energy barrier for Cu adatom diffusion with exchange mechanism to the upper Ni layer was almost comparable with the downward energy barrier of Cu and Ni adatoms. Therefore, one can conclude that the jump up probability of Cu adatoms at the vicinity of the step edge increase when the island has a second layer nearby.

On the other hand, the dimer formation energy for Cu atoms is quiet small compared to the hopping energy on Cu(111) surface, the dimer formation is expected to immediately take place when the two Cu atoms are in close proximity with each other on the surface. Since the energy barriers do not change for trimer formation, an adatom can easily participate to the cluster formation. Therefore, the process of Cu cluster formation on Ni monolayer islands can be explained with these mechanisms. Whenever Cu atoms can overcome the energy barrier 0.33 eV of upward exchange, there will be a chance for a dimer formation. Once there is a dimer formation on the island every jumping Cu atoms towards the dimer are expected to participate within and stay attached to the cluster. Increasing the size of the cluster on the upper layer of island relatively decreases the energy barriers for upward diffusion processes. Since the energy barriers for the mechanisms in opposite direction are increased by couple of times, the upward process turns to be a one way process. Therefore, the critical mechanism determining whether the island would be a pure Ni surrounded by Cu atoms or Cu-Ni mixed island is found to be the dimer formation over the Ni monolayer islands.

Table 6.1: The energy barriers for various diffusion mechanisms of Ni and Cu on Cu(111). Abbreviations: St: step, ML: monolayer, DL: doublelayer, M: monomer, H: hopping, E: exchange. +X represents X chains of Cu or Ni atoms at the step, A/ represents adatom on the surface or island layer where A can be one of Cu or Ni. The values in brackets ( ) are up barriers for hopping and exchange diffusion mechanisms and detachment barriers from dimer and trimer.

Dif. Mech.	Ni/Ni-layer	Ni/Cu-layer	Cu/Cu-layer	Cu/Ni-layer
M. ML St. H.	0.57(1.40)	0.54(1.68)	0.48(1.39)	0.56(1.21)
M. ML St. E.	0.33(0.88)	0.16(1.28)	0.14(0.91)	0.32(0.60)
M. ML St.+1 E.	0.33(0.99)	0.02(1.10)	0.07(0.76)	0.33(0.72)
M. ML St.+2 E.	0.38(1.23)	0.17(0.95)	0.16(0.66)	0.33(0.87)
M. DL St. E.	0.89(0.69)	0.70(0.88)	0.69(0.72)	0.99(0.50)
M. DL St.+1 E.	0.79(0.74)	-	-	0.79(0.60)
Dimer	0.01(0.38)	0.14(0.14)	0.01(0.38)	0.03(0.33)
Cu-Ni Dimer	0.02(0.36)	0.001(0.42)	-	0.02(0.36)
Cu-Cu Trimer	-	0.10(0.14)	0.01(0.28)	-
Ni-Ni Trimer	-	0.08(0.13)	0.003(0.27)	-
Cu-Ni Trimer	-	0.003(0.27)	0.02(0.26)	-

7. CONCLUSION

In this Thesis, a new and highly optimized Cu-Ni model potential within the formalism of EAM was developed. The optimization of the potential was designed to involve both experimental and *ab-initio* data not only for the pure elements of Cu and Ni but also for the Cu-Ni alloy. To control the parameters for a better fitting, selected properties of the elements and the alloy were treated with different weight. The potential reproduced both fitted and predicted properties with a reasonable precision, including elastic constants, phonon frequencies, melting points, alloy mixing enthalpy, lattice-defect energies and energies of alternate structures, and energetics on the flat surfaces of Cu and Ni. Given that the potential provided reliable results for surface energetics and energy barriers of various diffusion mechanisms, the current alloy potential is expected to correctly describe the characteristics of Ni growth on Cu surfaces or vice versa. The fact that no temperature dependent properties were included in the fitting database and yet the potential predicts the melting temperatures and alloy mixing enthalpy in good agreement with experiment affirms the transferability of the potential for higher temperature applications.

To further analyze the higher temperature capabilities of the current Cu-Ni potential, the thermodynamical properties of disordered and ordered Cu-Ni alloys were investigated. The entropy change between disordered and ordered crystals was found to be almost negligible. Although the configurational entropy favors the mixing and contributes to the solid solution phase, the negative mixing entropy of the phonons and electronic states for Cu-Ni alloys favors unmixing and contributes to the miscibility gap. The dominant contribution to Cu-Ni thermodynamic properties were calculated to be vibrational whereas the concentration weighted mixing entropy showed a strong dependence on electronic states. The partial phonon DOS for Cu stiffens with increasing Ni concentration of Cu-Ni alloys.

Furthermore, the energetics of the nanostructures and the growth mechanisms were investigated both using MD simulations and total energy calculations to understand the nature of the growth for Ni and Cu on Cu(111) surface. The simulation cells were constructed to involve mono and double layer Ni islands with Cu adatom and vacancy islands. From the simulations it was found that Cu atoms could migrate to Ni islands and decorate and even cover the upper layers of Ni islands. The formation of the islands was found to be governed by the nature of the decoration process. For the double-layer Ni islands, the migration of Cu atoms to the upper layers were predicted to be 7.5 times faster than those Cu atoms around monolayer Ni islands. The low concentrations of Cu atoms near the Ni islands led to decorations of only the first layers. The energy barriers were also calculated using NEB method for various diffusion mechanisms on Cu(111) surface. Since the calculated energy barrier for forming a dimer was found to be considerably low compared to all other investigated mechanisms, dimer formation was predicted to be the critical mechanism for the formation of Cu-Ni islands. While for monolayer Ni islands, the second layers were formed as a mixture of Cu and Ni elements, for double layer Ni islands, the upper layers were built with a segregated structure where Ni atoms were surrounded by Cu atoms. From the deposition simulations it was found that Ni islands tend to grow in hexagonal shape when the deposition rates were grater than 10ns^{-1} which was in good agreement with the results of under 1ML Ni deposition experiments where the nanostructures on Cu(111) surface generally have hexagonal like shapes with monolayer heights.

REFERENCES

[1] **Finnis, M.W. and Sinclair, J.E.** (1984). A simple empirical N-body potential for transition metals, *Philos. Mag. A*, *50*, 45.

[2] **Sutton, A.P. and Chen, J.** (1990). Long-range finnis-sinclair potentials, *Philos. Mag.*, *61*, 139.

[3] **Ackland, G.J. and Vitek, V.** (1990). Many-body potentials and atomic scale relaxations in noble metal alloys, *Phys. Rev. B*, *41*, 10324.

[4] **Cleri, F. and Rosato, V.** (1993). Tight-binding potentials for transition metals and alloys, *Phys. Rev. B*, *48*, 22.

[5] **Jacobsen, K.W., Norskov, J.K. and Puska, M.J.** (1987). Interatomic Interactions in the Effective-Medium Theory, *Phys. Rev. B*, *35*, 7423.

[6] **Ercolessi, F. and Adams, J.B.** (1994). Interatomic Potentials from First-Principles Calculations: The Force-Matching Method, *Europhys. Lett.*, *26*, 583.

[7] **Daw, M.S. and Baskes, M.I.** (1984). Embedded-atom method: Derivation and application to impurities and other defects in metals, *Phys. Rev. B*, *29*, 6443.

[8] **Foiles, S.M., Baskes, M.I. and Daw, M.S.** (1986). Embedded-atom-method functions for the fcc metals Cu, Ag, Au, Ni, Pd, Pt, and their alloys, *Phys. Rev. B*, *33*, 7983.

[9] **Foiles, S.M.** (1985). Calculation of the surface segregation of Ni-Cu alloys with the use of the embedded-atom method, *Phys. Rev. B*, *32*, 7685.

[10] **Kohn, W. and Sham, L.J.** (1965). Self-Consistent Equations Including Exchange and Correlation Effects, *Phys. Rev.*, *140*, A1133.

[11] **Daw, M.S. and Hatcher, R.D.** (1985). Application of the Embedded Atom Method to Phonons in Transition Metals, *Solid State Comm.*, *56*, 697.

[12] **Bian, Q., Bose, S.K. and Shukla, R.C.** (2008). Vibrational and thermodynamic properties of metals from a model embedded-atom potential, *J. Phys. Chem. Solids*, *69*, 168.

[13] **Zhou, X.W., Johnson, R.A. and Wadley, H.N.G.** (2004). Misfit-energy-increasing dislocations in vapor-deposited CoFe/NiFe multilayers, *Phys. Rev. B*, *69*, 144113.

[14] **Johnson, R.A.** (1989). Alloy models with the embedded-atom method, *Phys. Rev. B*, *39*, 12554.

[15] **Kohanoff, J.**, (2006). *Electronic Structure Calculations for Solids and Molecules: Theory and Computational Methods*, Cambridge University Press.

[16] **Born, M. and Oppenheimer, J.R.** (1927). Quantum theory of the molecules, *Ann. d. Physik*, *84*, 457.

[17] **Hohenberg, P. and Kohn, W.** (1964). Inhomogeneous electron gas, *Phys. Rev.*, *136*, B864.

[18] **Martin, R.M.**, (2004). *Electronic Structure: Basic Theory and Practical Methods*, Cambridge University Press, first edition edition.

[19] **Ceperley, D.M. and Alder, B.J.** (1980). Ground State of the Electron Gas by a Stochastic Method, *Phys. Rev. Lett.*, *45*, 566.

[20] **Vosko, S.H.**, **Wilk, L. and Nusair, M.** (1980). Accurate spin-dependent electron liquid correlation energies for local spin density calculations: a critical analysis, *Can. J. Phys.*, *58*, 1200.

[21] **Perdew, J.P. and Zunger, A.** (1981). Self-interaction correction to density-functional approximations for many-electron systems, *Phys. Rev. B*, *23*, 5048.

[22] **Perdew, J.P. and Wang, Y.** (1992). Accurate and simple analytic representation of the electron-gas correlation energy, *Phys. Rev. B*, *45*, 13244.

[23] **Perdew, J.P.**, **Burke, K. and Ernzerhorf, M.** (1996). Generalized Gradient Approximation Made Simple, *Phys. Rev. Lett.*, *77*, 3865.

[24] **Stott, M.J. and Zaremba, E.** (1980). Quasiatoms: An approach to atoms in nonuniform electronic systems, *Phys. Rev. B*, *22*, 1564.

[25] **Zhou, X.W. and Wadley, H.N.G.** (2005). A charge transfer ionic–embedded atom method potential for the O–Al–Ni–Co–Fe system, *J. Phys.: Condens. Matter*, *17*, 3619.

[26] **Baskes, M.I.** (1992). Modified embedded-atom potentials for cubic materials and impurities, *Phys. Rev. B*, *46*, 2727.

[27] **Mishin, Y.**, **Mehl, M.J.**, **Papaconstantopoulos, D.A.**, **Voter, A.F. and Kress, J.D.** (2001). Structural stability and lattice defects in copper: Ab initio, tight-binding, and embedded-atom calculations, *Phys. Rev. B*, *63*, 224106.

[28] **Mishin, Y.**, **Farkas, D.**, **Mehl, M.J. and Papaconstantopoulos, D.A.** (1999). Interatomic potentials for monoatomic metals from experimental data and *ab initio* calculations, *Phys. Rev. B*, *59*, 3393.

[29] **Voter, A.F.**, (1995). *in Intermetallic Compounds: Principles and Practice*, John Wiley and Sons, Ltd, edited by j. h. westbrook and r. l. fleischer, vol. 1 edition.

[30] **Rose, J.H.**, **Smith, J.R.**, **Guinea, F. and Ferrante, J.** (1984). Universal features of the equation of state of metals, *Phys. Rev. B*, *29*, 2963.

[31] **Barber, J.R.**, (2010). *Elasticity*, Springer Science, edited by g. m. l. gladwell, solid mechanics and its applications vol. 172 edition.

[32] **Sadd, M.H.**, (2009). *Elasticity: Theory, Applications, and Numerics*, Academic Press, second edition edition.

[33] **Mishin, Y.**, (2005). *Handbook of Materials Modelling*, Springer, Netherlands, editied by s. yip edition.

[34] **Verlet, L.** (1967). Computer Experiments on Classical Fluids. I. Thermodynamical Properties of Lennard-Jones Molecules, *Phys. Rev.*, *98*, 159.

[35] **Nose, S.** (1984). A Unified Formulation of the Constant Temperature Molecular-Dynamics Methods, *Journal of Chemical Physics*, *81*, 511.

[36] **Hoover, W.G.** (1985). Canonical Dynamics - Equilibrium Phase-Space Distributions, *Physical Review A*, *31*, 1695.

[37] **Henkelman, G.**, **Johannesson, G. and Jonsson, H.**, (2000). *Methods For Finding Saddle Points and Minimum Energy Paths, in Progress on Theoretical Chemistry and Physics*, Kluwer Academic Publishers, edited by s. d. schwartz edition.

[38] **Mills, G. and Jonsson, H.** (1994). Quantum and thermal effects in H_2 dissociative adsorption: Evaluation of free energy barriers in multidimensional quantum systems, *Phys. Rev Lett.*, *72*, 1124.

[39] **Mills, G.**, **Jonsson, H. and Schater, G.** (1995). Reversible work transition state theory: application to dissociative adsorption of hydrogen, *Surf. Sci.*, *324*, 305.

[40] **Haydock, R.**, **Heine, V. and Kelly, M.J.** (1972). Electronic structure based on the local atomic environment for tight-binding bands, *J. Phys. C*, *5*, 2845.

[41] **Wu, S.**, **Cocks, J. and Jayanthi, C.** (1994). General recursive relation for the calculation of the local Green's function in the resolvent-matrix approach, *Phys. Rev. B*, *49*, 7957.

[42] **Dy, K.S.**, **Wu, S. and Spratlin, T.** (1979). Exact solution for the resolvent matrix of a generalized tridiagonal Hamiltonian, *Phys. Rev. B*, *20*, 4237.

[43] **Kennedy, J. and Eberhart, R.C.** (1995). Particle Swarm Optimization, *Proc. IEEE Int. Conf. Neural. Netw.*, *4*, 1942.

[44] **Zhan, Z.**, **Xiao, J. and Zhang, J.** (2007). Adaptive Control of Acceleration Coefficients for Particle Swarm Optimization Based on Clustering Analysis, *IEEE Congress on Evolutionary Computation (CEC 2007)*, 3276.

[45] **Zhan, Z., Zhang, J., Li, Y. and Chung, H.S.** (2009). Adaptive Particle Swarm Optimization, *IEEE Trans. Syst., Man, Cybern. B, Cybern.*, *39*, 1362.

[46] **Ma, F. and Xu, K.** (2007). Size-dependent multilayer relaxation of nanowires and additional effect of surface stresses, *Solid State Commun.*, *141*, 273.

[47] **Ma, F. and Xu, K.** (2006). Dimension-induced structural stability transition: The stable and metastable phases of nanowires, *Solid State Commun.*, *140*, 487.

[48] **Lang, B., Joyner, R.W. and Somorjai, G.A.** (1972). Low energy electron diffraction studies of chemisorbed gases on stepped surfaces of platinum, *Surf. Sci.*, *30*, 454.

[49] **Daw, M.S., Foiles, S.M. and Baskes, M.I.** (1993). The embedded-atom method: a review of theory and applications, *Mater. Sci. Rep.*, *9*, 251.

[50] **Durukanoğlu, S., Kara, A. and Rahman, T.S.** (1997). Local structural and vibrational properties of stepped surfaces: Cu(211), Cu(511), and Cu(331), *Phys. Rev. B*, *55*, 13894.

[51] **Durukanoğlu, S. and Rahman, T.S.** (2003). Structure of Ag(410) and Cu(320), *Phys. Rev. B*, *67*, 205406.

[52] **Tian, Z.J. and Rahman, T.S.** (1993). Energetics of stepped Cu surfaces, *Phys. Rev. B*, *47*, 9751.

[53] **Wang, D., Zhao, J., Hu, S., Yin, X., Liang, S., Liu, Y. and Deng, S.** (2007). Where, and How, Does a Nanowire Break?, *Nano Lett.*, *7*, 1208.

[54] **Liang, W. and Zhou, M.** (2006). Atomistic simulations reveal shape memory of fcc metal nanowires, *Phys. Rev. B*, *73*, 115409.

[55] **Kara, A. and Rahman, T.S.** (1998). Vibrational Properties of Metallic Nanocrystals, *Phys. Rev. Lett.*, *81*, 1453.

[56] **Hestenes, M.R. and Stiefel, E.** (1952). Methods of Conjugate Gradients for Solving Linear Systems, *J. Res. Nat. Bur. Stand.*, *49*, 409.

[57] **Durukanoğlu, S. and Rahman, T.S.** (1998). Atomic relaxations and thermodynamics on Cu(410), *Surf. Sci.*, *409*, 395.

[58] **Yıldırım, H. and Durukanoğlu, S.** (2004). Structural relaxations of Cu vicinals, *Surf. Sci.*, *557*, 190.

[59] **Wan, J., Fan, Y.L., Gong, D.W., Shen, S.G. and Fan, X.Q.** (1999). Surface relaxation and stress of fcc metals: Cu, Ag, Au, Ni, Pd, Pt, Al and Pb, *Modelling Simul. Mater. Sci. Eng.*, *7*, 189, references therein.

[60] **Voter, A.F. and Chen, S.P.** (1987). Accurate Interatomic Potentials for Ni, Al, and Ni_3Al, *Mat. Res. Soc. Symp. Proc.*, *82*, 175.

[61] **Slater, J.C.** (1930). Atomic Shielding Constants, *Phys. Rev.*, *36*, 57.

[62] **Clementi, E. and Raimondi, D.L.** (1963). Atomic Screening Constants from SCF Functions, *J. Chem. Phys.*, *38*, 2686.

[63] **Clementi, E.**, **Raimondi, D.L. and Reinhardt, W.P.** (1967). Atomic Screening Constants from SCF Functions. II. Atoms with 37 to 86 Electrons, *J. Chem. Phys.*, *47*, 1300.

[64] **Giannozzi, P.**, **Baroni, S.**, **Bonini, N.**, **Calandra, M.**, **Car, R.**, **Cavazzoni, C.**, **Ceresoli, D.**, **Chiarotti, G.L.**, **Cococcioni, M.**, **Dabo, I.**, **Corso, A.D.**, **de Gironcoli, S.**, **Fabris, S.**, **Fratesi, G.**, **Gebauer, R.**, **Gerstmann, U.**, **Gougoussis, C.**, **Kokalj, A.**, **Lazzeri, M.**, **Martin-Samos, L.**, **Marzari, N.**, **Mauri, F.**, **Mazzarello, R.**, **Paolini, S.**, **Pasquarello, A.**, **Paulatto, L.**, **Sbraccia, C.**, **Scandolo, S.**, **Sclauzero, G.**, **Seitsonen, A.P.**, **Smogunov, A.**, **Umari, P. and Wentzcovitch, R.M.** (2009). QUANTUM ESPRESSO: a modular and open-source software project for quantum simulations of materials, *J. Phys. Condens. Matter*, *21*, 39550.

[65] **Vanderbilt, D.** (1990). Soft self-consistent pseudopotentials in a generalized eigenvalue formalism, *Phys. Rev. B*, *41*, 7892.

[66] **Corso, A.D. and de Gironcoli, S.** (1999). *Ab initio* phonon dispersions of Fe and Ni, *Phys. Rev. B*, *62*, 273.

[67] **Monkhorst, H.J. and Pack, J.D.** (1976). Special points for Brillouin-zone integrations, *Phys. Rev. B*, *13*, 5188.

[68] **Clarke, J.K.A. and Spooner, T.A.** (1971). The formation of homogeneous copper-nickel alloy films in ultra-high vacuum, *J. Phys. D: Appl. Phys.*, *4*, 1196.

[69] **Wagner, W.**, **Poerschke, R.**, **Axmann, A. and Schwahn, D.** (1980). Neutron-scattering studies of an electron-irradiated ^{62}Ni-41.4-at.%-^{65}Cu alloy, *Phys. Rev. B*, *21*, 3087.

[70] **Chakrabarti, D.J.**, **Laughlin, D.E.**, **Chen, S.W. and Chang, Y.A.**, (1994). *Phase Diagrams of Binary Copper Alloys*, ASM International, Materials Park, OH, in: p. subramanian, d. chakrabarti, d. laughlin (eds.) edition.

[71] **Kart, S.Ö.**, **Tomak, M. and Çağın, T.** (2005). Phonon Dispersions and Elastic Constants of Disordered Pd-Ni Alloys, *Physica B*, *355*, 382.

[72] **Hsieh, H.H.**, **Chang, Y.K.**, **Pong, W.F.**, **Pieh, J.Y.**, **Tseng, P.K.**, **Sham, T.K.**, **Coulthard, I.**, **Naftel, S.J.**, **Lee, J.F.**, **Chung, S.C. and Tsang, K.L.** (1998). Electronic structure of Ni-Cu alloys: The d-electron charge distribution, *Phys. Rev. B*, *57*, 15204.

[73] **Kittel, C.**, (1986). *Introduction to Solid State Physics*, Wiley-Interscience, 6st edition.

[74] **Smith, C.J.**, editor, (1976). *Metal Reference Book*, Butter-worth, London.

[75] **Simons, G. and Wang, H.**, (1977). *Single Crystal Elastic Constants and Calculated Aggregate Properties*, MIT Press, Cambridge, MA.

[76] **Ho, J.**, **Polak, M.L.**, **Ervin, K.M. and Lineberger, W.C.** (1993). Photoelectron spectroscopy of nickel group dimers: Ni_2^-, Pd_2^-, and Pt_2^-, *J. Chem. Phys.*, *99*, 8542.

[77] **Morse, M.D.** (1986). Clusters of transition-metal atoms, *Chem. Rev.*, *86*, 1049.

[78] **Huber, K.P. and Hertzberg, G.**, (1977). *Constants of Diatomic Molecules*, Van Nostrand Reinhold, New York.

[79] **Siegel, R.W.** (1978). Vacancy concentrations in metals, *J. Nucl. Mater.*, *69&70*, 117.

[80] **Wycisk, W. and Feller-Kniepmeier, M.** (1978). Quenching experiments in high purity Ni, *J. Nucl. Mater.*, *69&70*, 616.

[81] **Balluffi, R.W.** (1978). Vacancy defect mobilities and binding energies obtained from annealing studies, *J. Nucl. Mater.*, *69&70*, 240.

[82] **Ehrhart, P.**, (1991). *Atomic defects in metals*, Springer-Verlag, Berlin, edited by h. ullmaier,landolt-bornstein, new series, vol. 25 edition.

[83] **Campbell, F.C.**, (2008). *Elements of Metallurgy and Engineering Alloys*, ASM International.

[84] **Zheng, L.**, **An, Q.**, **Xie, Y.**, **Sun, Z. and Luo, S.** (2007). Homogeneous nucleation and growth of melt in copper, *J. Chem. Phys.*, *127*, 164503.

[85] **Barnett, R.N. and Landman, U.** (1991). Surface premelting of Cu(110), *Phys. Rev. B*, *44*, 3226.

[86] **Nilsson, G. and Rolandson, S.** (1973). Lattice Dynamics of Copper at 80 K, *Phys. Rev. B*, *7*, 2393.

[87] **Birgenau, R.J.**, **Cordes, J.**, **Dolling, G. and Woods, A.D.B.** (1964). Normal Modes of Vibration in Nickel, *Phys. Rev.*, *136*, A1359.

[88] **Epstein, S.G. and Carlson, O.N.** (1965). The elastic constants of nickel-copper alloy single crystals, *Acta Metallurgica*, *13*, 487.

[89] **Reuse, F.A. and Khanna, S.N.** (1995). Geometry, electronic structure, and magnetism of small Ni_n (n = 2-6, 8, 13) clusters, *Chem. Phys. Lett.*, *234*, 77.

[90] **Carter, C.B. and Ray, I.L.F.** (1977). On the stacking-fault energies of copper alloys, *Philos. Mag.*, *35*, 189.

[91] **Murr, L.E.**, (1995). *nterfacial Phenomena in Metals and Alloys*, Addison-Wesley, Reading, MA.

[92] **Zimmermann, J.A.**, **Gao, H.J. and Abraham, F.F.** (2000). Generalized stacking fault energies for embedded atom FCC metals, *Modell. Simul. Mater. Sci. Eng.*, *8*, 103.

[93] **Wollenberger, H.J.**, (1996). *Physical Metallurgy*, Elsevier Science, Ltd, fourth, revised and enhanced edition, edited by r. w. cahn and p. haasen, vol. 2 edition.

[94] **Tyson, W.R. and Miller, W.R.** (1977). Surface free energies of solid metals: Estimation from liquid surface tension measurements, *Surf. Sci.*, *62*, 267.

[95] **Mason, D.**, **Foulkes, W.M.C. and Sutton, A.P.** (2009). A simple model for large-scale simulations of fcc metals with explicit treatment of electrons, *Philos. Mag. Let.*, *90*, 51.

[96] **Tucker, J.D.**, **Allen, T.R. and Morgan, D.**, (2007). Ab initio *defect properties for modeling radiation-induced segregation in Fe-Ni-Cr alloys*, Addison-Wesley, Whistler, BC, in proceedings of the 13th international symposium on environmental degradation of materials in nuclear power systems edition.

[97] **Srikanth, S. and Jacob, K.T.** (1989). Thermodynamic properties of Cu-Ni alloys: measurements and assessment, *Mater. Sci. Tech.*, *5*, 427.

[98] **Mey, S.** (1992). Thermodynamic re-evaluation of the Cu-Ni system, *CALPHAD*, *16*, 255.

[99] **Bonny, G.**, **Pasianot, R.C.**, **Castin, N. and Malerba, L.** (2009). Ternary Fe-Cu-Ni many-body potential to model reactor pressure vessel steels: First validation by simulated thermal annealing, *Philos. Mag.*, *89*, 3531.

[100] **Antczak, G. and Ehrlich, G.**, (2010). *Surface Diffusion: Metals, Metal Atoms, and Clusters*, Cambridge University Press, Cambridge.

[101] **Munoz, J.A.**, **Lucas, M.S.**, **Mauger, L.**, **Halevy, I.**, **Horwath, J.**, **Semiatin, S.L.**, **Xiao, Y.**, **Chow, P.**, **Stone, M.B.**, **Abernathy, D.L. and Fultz, B.** (2013). Electronic structure and vibrational entropies of fcc Au-Fe alloys, *Phys. Rev. B*, *87*, 014301.

[102] **Fultz, B.**, **Anthony, L.**, **Nagel, L.J.**, **Nicklow, R.M. and Spooner, S.** (1995). Phonon densities of states and vibrational entropies of ordered and disordered Ni_3Al, *Phys. Rev. B*, *52*, 3315.

[103] **Anthony, L.**, **Okamoto, J.K. and Fultz, B.** (1993). Vibrational Entropy of Ordered and Disordered Ni_3Al, *Phys. Rev. Lett.*, *70*, 1128.

[104] **Lucas, M.S.**, **Mauger, L.**, **noz, J.A.M.**, **Halevy, I.**, **Horwath, J.**, **Semiatin, S.L.**, **Leontsev, S.O.**, **Stone, M.B.**, **Abernathy, D.L.**, **Xiao, Y.**, **Chow, P. and Fultz, B.** (2013). Phonon densities of states of face-centered-cubic Ni-Fe alloys, *J. Appl. Phys.*, *113*, 17A308.

[105] **Kravets, A.F.**, **Timoshevskii, A.N.**, **Yanchitsky, B.Z.**, **Salyuk, O.Y.**, **Yablonovskii, S.O.**, **Andersson, S. and Korenivski, V.** (2012). Exchange-induced phase separation in Ni–Cu films, *J. Magn. Magn. Mater.*, *324*, 2131.

[106] **Loram, J.W. and Chen, Z.** (1983). Spin fluctuation contributions to the specific heat of CuNi alloys, *J. Phys. F: Met. Phys.*, *13*, 1519.

[107] **Phuong, L.D.**, **Pasture, A. and Manh, D.N.** (1993). Effect of s-d hybridization on interatomic pair potentials of the 3d liquid transition metals, *J. Phys.: Condens. Matter*, *5*, 1901.

[108] **Xie, Y. and Zhao, S.** (2011). The energetic and structural properties of bcc NiCu, FeCu alloys: A first-principles study, *Comp. Mater. Sci.*, *50*, 2586.

[109] **Born, M. and Huang, K.**, (1954). *Dynamical Theory of Crystal Lattices*, Oxford at the Clarendon Press, first edition edition.

[110] **Ozoliņš, V.**, **Wolverton, C. and Zunger, A.** (1998). First-principles theory of vibrational effects on the phase stability of Cu-Au compounds and alloys, *Phys. Rev. B*, *58*, R5897.

[111] **Meyer, R.**, **Lewis, L.J.**, **Prakash, S. and Entel, P.** (2003). Vibrational properties of nanoscale materials: From nanoparticles to nanocrystalline materials, *Phys. Rev. B*, *68*, 104303.

[112] **Kresch, M.**, **Delaire, O.**, **Stevens, R.**, **Lin, J.Y.Y. and Fultz, B.** (2007). Neutron scattering measurements of phonons in nickel at elevated temperatures, *Phys. Rev. B*, *75*, 104301.

[113] **Alam, A.**, **Chouhan, R.K. and Mookerjee, A.** (2011). Phonon modes and vibrational entropy of disordered alloys with short-range order: A first-principles calculation, *Phys. Rev. B*, *83*, 054201.

[114] **Touloukian, Y.S. and Buyco, E.H.**, (1970). *Thermophysical Properties of Matter, The TPRC Data Series, Specific Heat, Metallic Elements and Alloys, vol. 4*, Plenum Data Company, New York.

[115] **Bogdanoff, P.D.**, **Swan-Wood, T.L. and Fultz, B.** (2003). Phonon entropy of alloying and ordering of Cu-Au, *Phys. Rev. B*, *68*, 014301.

[116] **Pons, S.**, **Mallet, P.**, **Magaud, L. and Veuillen, J.Y.** (2002). Spontaneous evolution of the Ni/Cu(111) interface at 300 K, *Surf. Sci*, *511*, 449.

[117] **Mulazzi, M.**, **Stanescu, S.**, **Fujii, J.**, **Vobornik, I.**, **Boeglin, C.**, **Belkhou, R.**, **Rossi, G. and Barbier, A.** (2006). Structural and electronic properties of thin Ni layers on Cu(111) as investigated by ARPES, STM and GIXD, *Surf. Sci.*, *600*, 3938.

[118] **Boeglin, C.**, **Stanescu, S.**, **Cherifi, S.**, **Deville, J.P.**, **Ohresser, P.**, **Barbier, A. and Brookes, N.B.** (2002). High dipolar magnetic moment observed on Ni/Cu(111) nanostructures by magnetic circular X-ray dichroism, *Surf. Sci.*, *507-510*, 522.

[119] **Pons, S.**, **Mallet, P. and Veuillen, J.Y.** (2001). Electron confinement in nickel and copper nanostructures on Cu(111), *Phys. Rev. B*, *64*, 193408.

[120] **Magaud, L.**, **Pasturel, A.**, **Mallet, P.**, **Pons, S. and Veuillen, J.Y.** (2004). Spin-polarized Shockley state at Ni(111) free surface and at Ni-Cu–based structures on Cu(111) surface, *Europhysics Lett.*, *67*, 90.

CURRICULUM VITAE

Name Surname: Berk ONAT

Place and Date of Birth: İstanbul, 29.05.1980

Address: İTÜ, Informatics Institute, Ayazağa Campus, 34469, Maslak, İstanbul

E-Mail: berk.onat@be.itu.edu.tr

B.Sc.: İTÜ, Science & Letters Faculty, Physics Department, Physics Engineering, 2003

M.Sc.: İTÜ, Informatic Institute, Computational Science and Engineering, 2005

List of Publications:

- **Onat B.**, Durukanoğlu S., Dağ H., 2007: A Parallel Implementation: Real Space Green's Function Technique,*International Journal of High Performance Computing Applications*,**21**, 66-74.

PUBLICATIONS ON THE THESIS

- **Onat B.**, Konuk M., Durukanoğlu S., Dereli G., 2009: Energetics and atomic relaxations of Cu nanowires: the effect of local strain and cross-sectional area, *Nanotechnology*, **20**, 075707.

- **Onat B.**, Durukanoğlu S., 2013: An Optimized Interatomic Potential for Cu-Ni Alloys with the Embedded-Atom Method, *submitted, under review*.

- **Onat B.**, Durukanoğlu S., 2013: The Vibrational and Thermodynamic Properties of Cu-Ni Alloys, *under preparation*.

- **Onat B.**, Gürlü O., and Durukanoğlu S. 2013: Growth of Cu-Ni Nanostructures on Cu(111) Surface, *under preparation*.

Awards:

- **The Best Poster Presentation in Symposium I**, 2012: Growth of Ni, Cu Nanostructures on Cu(111), Computer Modelling in Nanoscience and Nanotechnology: An Atomic Scale Perspective II, EMRS 2012 Fall Meeting, 17-21 September, Warsaw, Poland.

Professional Experience:

- **Research Scholarship**, February 2010 - April 2013: *Mechanical, Thermodynamic, and Electronic Properties of Metal Nanowires*, project under grant no 109T105, TUBİTAK, SabancıUniversity.

- **Researcher**, February 2007 - March 2009: *Double Layer Islands Decay and Relevant Diffusion Mechanisms: Cu/Cu(111) and Ag/Ag(111)*, project under grant no 106T157, TUBİTAK, İstanbul Technical University.

- **Co-organizer of Research Assistants**, Spring 2011 - Fall 2012: Computational Science and Engineering, Informatics Institute, İstanbul Technical University.

- **Teaching Assistant**, 15 - 26 August 2010: *Condensed Matter Physics and Systems Biology*, Densed Summer School for Undergraduate Students 2010, Feza Gürsey Institute.

- **Research Assistant**, Spring 2005 - Fall 2012: Computational Science and Engineering, Informatics Institute, İstanbul Technical University.

- **Teaching Assistant**, Spring 2005 - Fall 2012: *Parallel and Distributed Computing*, Informatics Institute, İstanbul Technical University.

- **Teaching Assistant**, Spring 2005 - Fall 2012: *Parallel Numerical Algorithms and Tools*, Informatics Institute, İstanbul Technical University.

- **IT Systems and Scientific Applications Administration**, Spring 2004 - Spring 2013: *High Performance Computing Center*, Computational Science and Engineering, Informatics Institute, İstanbul Technical University.